TUNING APPLICATION AND ADJUSTING PROPERTIES OF METAL-ORGANIC FRAMEWORKS VIA SMALL MODIFICATIONS

by

Alexander B. Spore

B.S., DePaul University, 2010

Submitted to the Graduate Faculty of

The Kenneth P. Dietrich School of Arts and Sciences in partial fulfillment

of the requirements for the degree of

Doctor of Philosophy

University of Pittsburgh

2019

UNIVERSITY OF PITTSBURGH

KENNETH P. DIETRICH SCHOOL OF ARTS AND SCIENCES

This thesis was presented

by

Alexander B. Spore

It was defended on

August 29th, 2018

and approved by

Haitao Liu, PhD, Associate Professor, Department of Chemistry

Alexander Star, PhD, Professor, Department of Chemistry

Christopher E. Wilmer, PhD, Assistant Professor, Department of Chemical and Petroleum Engineering

Thesis Advisor: Nathaniel L. Rosi, PhD, Associate Professor, Department of Chemistry

Tuning Application and Adjusting Properties of Metal-Organic Frameworks *via* Small Modifications

Alexander B. Spore, PhD

University of Pittsburgh, 2019

This dissertation describes how metal-organic framework (MOF) stability, properties, and performance can change with minor variation. Three topics of this dissertation include (i) examination of water vapor and liquid stability in ionic MOFs (ii) shell modification of MOFs for incorporation into mixed-matrix membranes (MMMs) and (iii) selection of MOFs for polyphosphazene polymer MMMs.

More specifically, chapter 2 will focus on the well-studied **bMOF-1**. Previous work has incorporated different cations into its pore environment to test changes to CO_2 capacity and luminescent properties. In this study, we incorporate cations with varying hydrophobicity into the pores and examine how the stability in water vapor and liquid changes. Chapter 3 will focus on work done in collaboration with the National Energy Technology Laboratory (NETL). In our study, shell modification of UiO-66-NH_2 with various functional groups adjusted particle incorporation into a MMM with Matrimid® polymer. The particle-polymer interface can be tested based on the separation and permeability properties of the MMMs. In chapter 4, our work with (NETL) continued. A polyphosphazene-based membrane was utilized and we tailored MOFs to (i) limit the gaps between the MOF and membrane and (ii) increase the CO_2/N_2 separation abilities of the membranes.

Table of Contents

List of Tables

List of Figures

List of Equations

Preface

Acknowledgements

Advisors and Co-Workers

To begin, I would like to thank my PhD advisor, Nathaniel L. Rosi for all of the support, time, and guidance during my time in his research laboratory. Professor Rosi has guided me through projects that were successes and failures, but never lost hope that the dream I had of this dissertation would be successful. And for that, I am, and will continue to be, eternally thankful.

I would like to thank my dissertation committee: Professor Haitao Liu, Professor Alexander Star, and Professor Christopher Wilmer. They have offered time and patience throughout my time at the University of Pittsburgh.

I also thank my collaborators at National Energy Technology Laboratory (NETL). Specifically, Erik Albenze, Surendar Venna, Jeffrey Culp, and Santosh Kumar. They have worked with Professor Rosi and me through two successful papers and it has been a fruitful endeavor.

I would not have been a successful student without the help from co-workers in Professor Rosi's laboratory, past and present. Drs. Tao Li and Kiley White for teaching me techniques and concepts for a successful laboratory approach. Jessica Schiren (Sammons), Andre Merg, Tianyi Luo, Yicheng Zhou, and Dr. Chen Zhang for their help throughout this process. And a very special thank you to Dr. Chong Liu. He and I came into Professor Rosi's laboratory together, and it has been an amazing working friendship that he and I have together. It was such a pleasure to watch him succeed in summer 2016 and I will also be one of his biggest cheerleaders.

I have had the pleasure of working with several undergraduate researchers in my time at Pitt. Thank you to Katherine Thompson, Evan Doud, and Catherine Madden for working with me to synthesize MOFs and optimize procedures.

Family and Friends

My family has painted a picture of what it takes to be successful, and I have followed their outline in many ways. For that, I am very thankful. My parents, Joe and Mary Beth, for being my biggest fans since birth, and for letting me be my own person. To my sisters, Dr. Emily Lowder, Dr. Molly DiMatteo, and Bridget Faulk, for keeping me in line, and loving me no matter how wild I may get.

To my friends, too numerous to name here that I met in graduate school, I thank you for keeping me sane and reminding me to have fun. And listening to me play at BBT on Tuesdays. I apologize to your ears, but I thank your hearts.

"Behind every great man, there is a woman rolling her eyes" –Bruce Almighty

My smart, caring, patient, and beautiful wife, Sarah Ashley: I would be nothing without you. Thank you, thank you, thank you! You are the reason that I powered through the last part of this journey. It was for you, as will the rest of my life. Thank you!

I would like to dedicate this work to the memory of Sr. Mary Helen Meyer (1921-2016). I am sorry you will not be here to celebrate with me.

“Up there she is. Up there”

1.0 Introduction

1.1 Metal-Organic Frameworks (MOFs)

Metal-organic frameworks (MOFs) are a growing and scientifically fascinating class of porous materials. MOFs are defined as crystalline materials composed of polydentate organic struts (ligands) connecting inorganic nodes (metal ions or clusters containing metals) into two- or three-dimensional structures.[1-3] Since Yaghi's groundbreaking publication of MOF-5 in 1999,[4] the field has witnessed variation of organic struts, inorganic nodes, and/or reaction conditions, leading to thousands of new MOF structures (Figure 1.1).

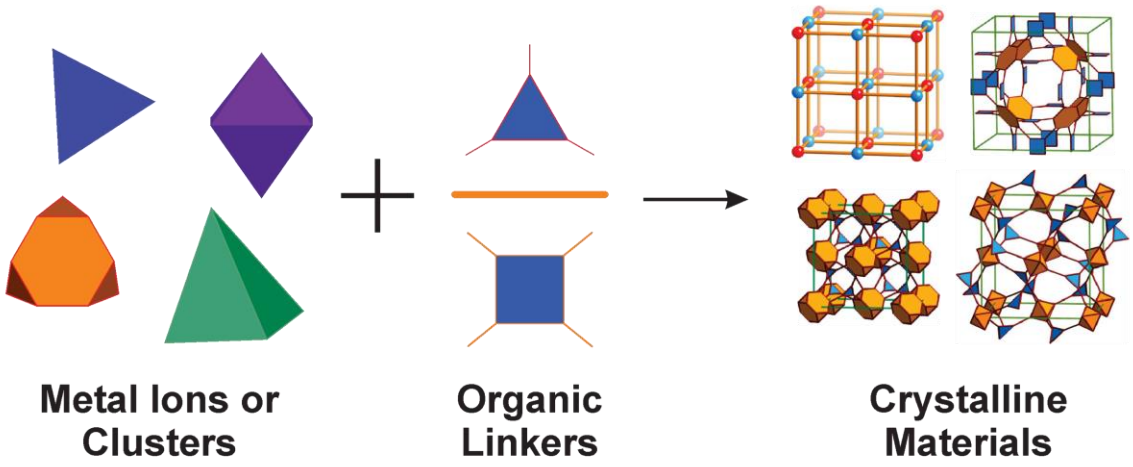

Figure 1.1 Scheme for MOF synthesis. Net figures curtesy of the Reticular Chemistry Structure Resource (RCSR) (http://rcsr.anu.edu.au).

Unlike some forms of porous materials, MOFs have the advantage of being crystalline. Therefore, the exact positions of all atoms in the structure can be determined through single crystal X-Ray diffraction studies.[5, 6] Definitive knowledge of MOF structure enables robust structure-property studies. Knowledge of the MOF structure can also allow for better prediction of experimental properties. For example, computational studies have been used to predict separation,[7, 8] storage,[9] conductivity,[10] heat transfer,[11] and catalytic properties,[12] as well as metrics such as surface area and pore volume.[13, 14] With the number of synthesized MOFs increasing every year, it is a time-saving benefit to analyze MOFs using computational modeling

rather than synthesizing them to experimentally determine properties. However, many times, computational modeling is used to confirm experimental results.[15] One example of how computation and experiment can work together is from Yang and coworkers.[16] To better understand CO_2 and CH_4 adsorption properties exhibited by a zirconium-terephthalate framework, UiO-66 (UiO = University of Oslo)[17], the researchers employed a combination of experimental techniques (thermal gravimetric analysis, calorimetry, X-Ray diffraction, and adsorption) and molecular modeling. The diffusion of gas molecules through the material was determined from theoretical techniques and they observed how each molecule has a preferential adsorption position within the MOF and how the slower moving CO_2 molecule can enhance the capture of the faster-moving CH_4 through the pores. These computational findings complimented what was determined experimentally.

MOF pores can range in dimensions from a few angstroms to several nanometers.[18-20] MOFs are typically prepared through solvothermal synthesis, that is, mixing metal salts with organic acids at elevated temperatures. Due to the simplicity of synthesis, pore dimensions can be easily tuned through variation of ligand length or shape. For example, the pores of MOF-5 (or IRMOF-1),[4] which is composed of the $Zn_4O(COO)_6$ inorganic secondary-building unit (SBU) linked by the benzene ring of 1,4-benzenedicarboxylate (BDC), can be expanded by utilizing a longer linear linker, *p*-terphenyl-4,4'-dicarboxylate (TPDC), to afford IRMOF-16.[18] Furthermore, the topology of MOF-5 can be changed by utilizing a ligand with three points of extension (triangular geometry), such as 1,3,5-benzenetribenzoate (BTB), to afford MOF-177.[20] In each case, the product MOFs have uniform pore dimensions (Figure 1.2).

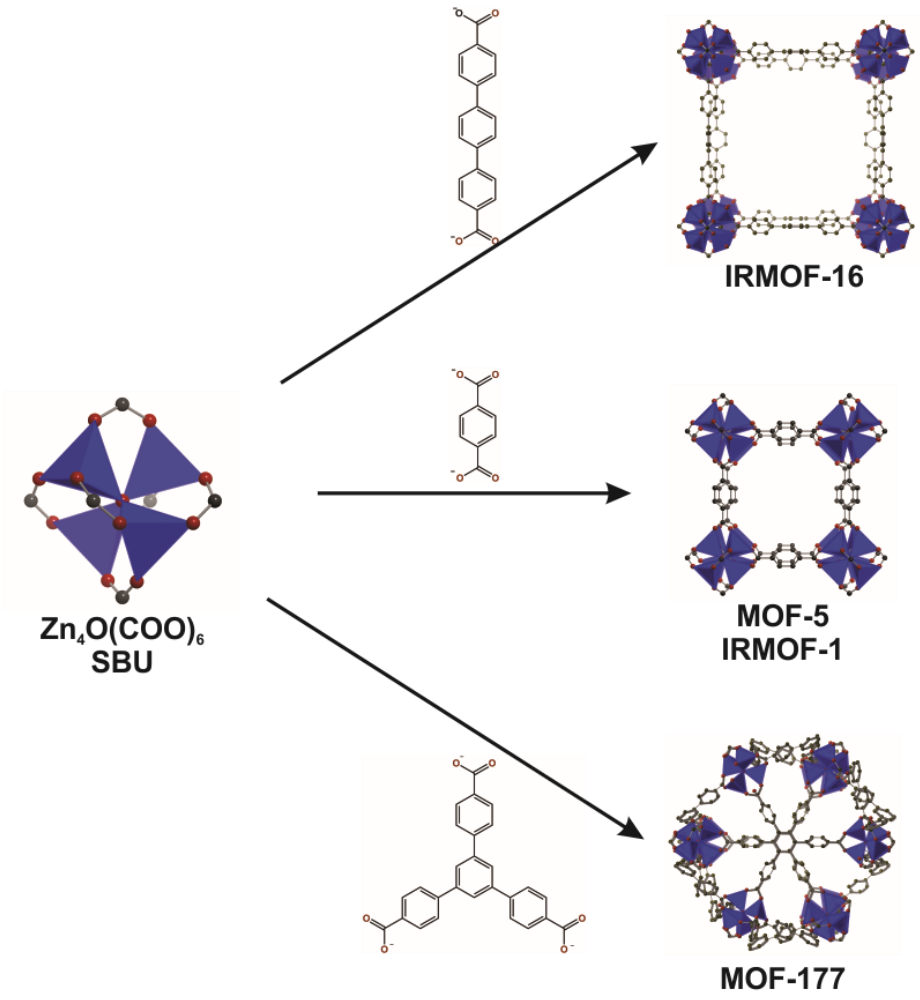

Figure 1.2 Image of $Zn_4O(COO)_6$ SBU with three possible MOF structures based on the organic ligand (Zn^{2+}, Blue polyhedra; C, dark grey spheres; O, dark red spheres. H atoms omitted for clarity).

Altering the pore dimensions and the topology are not the only ways through which different properties can be imparted into MOFs. Functionality can be imparted on MOFs through functionalized linkers or post-synthetic modification (PSM).[21] H. Deng, et. al. elegantly demonstrated how multiple functionalized linkers could be incorporated into a single MOF structure through the synthesis of multivariate MOFs (MTV MOFs).[22] In this study, MOF-5-type structures were synthesized with a combination of nine linkers containing different functional

groups at the 2,5 positions of the BDC linker. The linkers were mixed in the synthesis to yield single MOF crystals containing multiple different functional moieties in relatively stoichiometric ratios. While the linkers were randomly distributed throughout the framework, the backbone (Zn_4O SBU) remained throughout, resulting in the desired MOF-5 topology. The researchers limited the number of MOFs to study to 18 MOFs with 2-8 differently functionalized linkers. The adsorption properties of these MOFs were analyzed to examine how change in functionality can cause changes to the MOF properties (Figure 1.3).

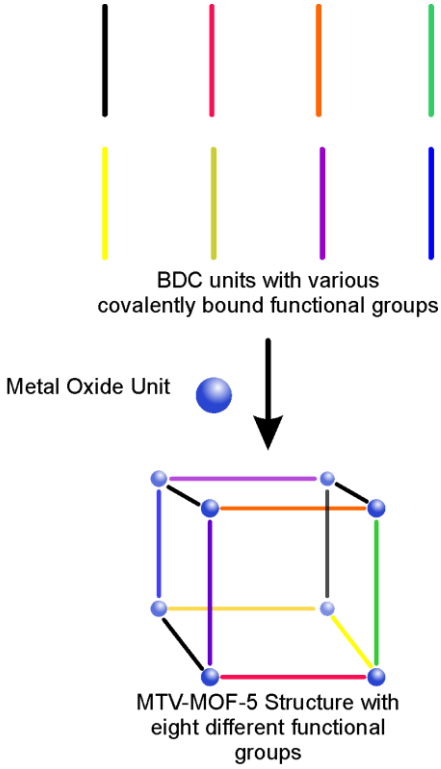

Figure 1.3 Synthesis of multivariate MOF (MTV-MOF) with eight different linkers, each represented by a different color.

Likewise, S. Garibay and S. Cohen demonstrated the use of PSM for changing MOF properties.[23] In this study, UiO-66 was synthesized with amino (UiO-66-NH_2), bromo (UiO-66-Br), nitro (UiO-66-NO_2) or naphthalene (UiO-66-1,4-Naph) substitution on the BDC linker. The amino-functionalized linker was then further reacted *in situ* with various anhydrides of varying

length and functionality to decorate the pore space with different functional moieties. The thermal stability and surface area of the MOFs were analyzed, and the results varied based on functional group on the BDC linker. It is important to note that after ligand modification or PSM, the MOF maintains its structural integrity and porosity.

1.2 Desired Applications of MOFs

With the many ways in which to change the topology and metrics of MOFs, it is critical to know what properties are desired for the materials being synthesized. MOFs have been used for a wide variety of applications including, but not limited to, gas capture/separation/storage,[24-27] catalysis,[28] sensing or imaging,[29-31] and drug delivery.[32] Herein, separation techniques and CO_2 capture will be discussed due to their relevance to the research projects presented in this thesis.

1.2.1 MOFs for Separation

Gas separations are an obvious application for MOFs, due to the tailorable porosity of the materials. Small molecule separation is an important industrial process. Most industrial separations are accomplished through distillation processes.[25] However, high-energy costs (heating or cooling) and limitations on molecular weight present challenges. Furthermore, the boiling point of the two species being separated must be significant for an efficient distillation. Because of the limitations listed, separations based on adsorptive properties have been considered.

MOFs can function as a separation absorbent material. MOFs have been used to separate small organic molecules[22-25] and gases.[33-35] Separations can be based on size/steric restrictions and/or differential adsorbate interactions with the pore walls of the MOFs. In many cases, MOFs can be used for multiple separation cycles. They can be regenerated through washing, heating, or applying pressure swings to remove analyte from the pores.

1.2.2 CO_2 Capture in MOFs

Increasing global temperatures are a serious concern facing the world. One of the major causes for the rising temperatures is the increase in greenhouse gases. The leading greenhouse gas is carbon dioxide (CO_2).[36] A large amount of CO_2 comes from coal-burning factories and power plants. While the most ideal way to deal with increased greenhouse gas emissions would be the elimination of carbon-based fuel sources, for the foreseeable future, the infrastructure is not in place to transition to cleaner alternatives. Until alternatives are accepted, a placeholder solution to increased CO_2 emissions is to capture it from "flue gas" that is released from coal-burning power plants. This "flue gas" contains ~15% CO_2, 73-77% nitrogen, ~5-7% water, and trace other gases.[26] Therefore, in order to successfully separate CO_2 from N_2, H_2O, and other gases in a flue stream, the material must have a high CO_2/N_2 selectivity and remain stable under humid conditions.

One current method for capturing CO_2 from flue gas is to utilize liquid amines, such as monoethanol amine (MEA). While liquid amines are effective in capturing CO_2 from other gases, they have some major shortcomings. First, there is a high-energy cost associated with regenerating MEA after it has chemically reacted with CO_2. The regeneration of MEA involves high temperature and high pressure. Furthermore, the toxicity of MEA is problematic.[37]

An ideal material for CO_2 capture would be porous and capture CO_2 through physisorption rather than chemisorption. MOFs have been identified as materials that can be used for this process.[27, 38] One of drawbacks of many promising MOFs is their limited stability in humid conditions.[13, 39] However, MOFs have been sought after for stationary phase separation of CO_2 from flue gas. Additionally, MOF/polymer composites have been examined for selective separation of CO_2.[40-43]

1.3 Desired Properties for Ideal MOF Application

In order to be efficient materials for use in the above-mentioned applications, MOFs must be designed for the actual working conditions. Herein, we will examine the properties that MOFs must exhibit to be considered for one of the applications listed above.

1.3.1 Stability in Industrial Conditions

Many industrial conditions include high temperatures and/or humid conditions. The thermal stability of some materials limits the effectiveness in industrial settings. However, many MOFs exhibit high thermal stability.[44, 45] Indeed, some MOFs remain stable and maintain porosity up to ~500 °C.[17] While 500 °C is an extreme case, many MOFs have thermal stability in the 300-400 °C range. This thermal stability makes some MOFs useful for certain industrial applications. One excellent example of a MOF family with high thermal stability is UiO-66.[17] The $Zr_6O_4(OH)_4(COO)_{12}$ SBU of this MOF contributes to the incredible thermal stability ($T_{decomposition}$ = 540 °C). Similarly, high thermal stability is observed in MIL-53,[46] which is a breathable MOF that contains $Al(OH)_3$ inorganic clusters that form strong metal-linker bonds with BDC, that allow it to have exceptional thermal stability. However, as noted above, minor modifications to these frameworks can result in a lower thermal stability. Most notably, UiO-66-NH_2 has a thermal stability of ~400 °C,[23] significantly lower than unmodified UiO-66.

While many MOFs have respectable thermal stability, many lack stability in humid conditions. A number of the applications of MOFs require a need for stability in the presence of water, including drug delivery, biological imaging, and CO_2 capture. Many MOFs degrade and/or lose porosity in the presence of water due to hydrolysis of the metal-ligand bond. This is especially true for MOFs constructed from softer metal ions (Zn^{2+}, Co^{2+}, etc.) and ligands containing hard-base carboxylates.[47] When water replaces the carboxylate, the crystallinity of the

MOF is compromised, resulting in a loss of porosity and therefore function. The two most common ways to construct a MOF that is stable in aqueous or humid conditions are to (i) increase the hydrophobicity within the framework through modification of the linker[48-50] or (ii) synthesize the MOF with hard bases (e.g. carboxylates) and hard metal ions, such as Zr^{4+} or Al^{3+}.[17, 46, 51]

The first route to impart water-stability into a MOF has been studied in the work of Walton, *et. al*.[52-54] In these works, the ligands used to synthesize isoreticular MOFs have small modifications, including alkyl chains or fluorine groups. MOF stability is then studied in water vapor or liquid. MOFs in two of these studies have Zn^{2+}-carboxylate metal-linker bonds[52, 53] that have been shown to have limited stability in aqueous conditions. However, when the ligands are modified with alkyl or fluorine groups, the metal-ligand bond is protected, leading to more stability in humid conditions. Variation in linker functionality is not novel and has been discussed above (see section 1.1). In this case, the changes to the functional groups on the linker are for the purpose of imparting water stability. However, once again there is a tradeoff in imparting water stability in this manner: the bulky alkyl groups reduce the surface area of the MOFs and can alter the adsorption properties of other species, such as CO_2 or CH_4.

The other common route of imparting water stability is to form stronger metal-linker bonds through hard acid-base interactions. Some metal centers include Zr^{4+} (UiO-66)[17, 49], Al^{3+} (MIL-53),[50] or lanthanides.[55, 56] The thermal stability of UiO-66 and MIL-53 have been discussed above. Many of these MOFs exhibit stability in harsh conditions such as boiling water for several days.[49] Yet, synthesis with hard acids such as Zr^{4+}, Al^{3+}, or Hf^{4+} can add complications due to the highly oxophilic nature of these ions. The MOFs can form quickly leading to defects in the

framework,[57] which can be tuned for the advantage of adsorption properties, but they can also cause variation in results based on synthetic conditions.

1.3.2 Interface with Polymers

MOFs, as stated above, have a rigid structure. Therefore, incorporation with polymers can be difficult due to polymer flexibility. There have been two ways that MOF/polymer hybrid materials have been developed. The first method for MOF/polymer integration is the creation of mixed-matrix membranes (MMMs).[58] MMMs have been sought-after for use in CO_2 separation.[59] MMMs combine the advantages of membrane materials with those of a secondary adsorption and separation material. However, there is a tradeoff between permeability and selectivity: as a material becomes more permeable, the less selective it will be for CO_2, or *vice versa*. This is represented by the Robeson upper bound, which established the highest permeability and selectivity a membrane material can exhibit.[60, 61]

In order to reach this upper limit, MOFs have been used as a filler material for MMMs.[40-42] In order to be an efficient filler material in MMMs, MOFs must (i) allow for gases to permeate through the MMM; (ii) interact with the polymer membrane material well to minimize or eliminate gaps between the particle and the polymer that would allow gases to flow through without selectivity; and (iii) be selective for the gas (CO_2) that is to be separated. The ease with which MOFs can be modified make them ideal materials for these processes.

One can also tune MMM properties by adjusting the filler particle/polymer ratio. This was recently observed in a study by DeCoste, et. al., in which HKUST-1 ($Cu_3(TMA)_2$, HKUST = Hong Kong University of Science and Technology) was used as a filler material. The MMMs were studied for ammonia separation. The MMMs had varying success based on the amount of MOF used and demonstrated long term stability, even under humid conditions. A recent study

has demonstrated that MOFs can be loaded up to 90% by weight into polymer membranes while still exhibiting the flexibility of the polymer and separation properties of the MOF.[62]

MOFs can be studied *via* computational modelling (see section 1.1), and this can be a great advantage in the synthesis of MMMs. Computational analysis can inform separation properties and it can be used to study/optimize the MOF-polymer interface to limit interface defects.[63-65] For example, in a recent study conducted by Semino, *et. al.*,[64] the computational analysis of a variety of MOFs with flexible (e.g. PEG) or rigid (e.g. polystyrene) polymers was conducted. Based on the result that the more flexible polymers would form more reliable MMMs, the researchers synthesized only MMMs with these polymers. Streamlining MOF and polymer selection makes MMMs attractive materials for a variety of separations.

Another MOF/polymer hybrid material are polymerMOFs (polyMOFs). PolyMOFs are the newer route for making hybrid materials. To synthesize polyMOFs, a flexible polymer is utilized as the ligand for MOFs synthesis. The ability to incorporate a non-porous, mostly amorphous polymer into the crystalline, porous, three-dimensional MOF to create a hybrid material is novel. The first polyMOFs were based on the MOF-5 structure and resulted in one-dimensional polymer growth through the pores of the MOF.[66] Since their first publication, polyMOFs have been shown to have increased surface area[67] and increase kinetic water stability compared to their conventional MOF counterparts.[68]

1.4 Tuning Properties and Application through Small Structural Modifications

The properties of MOFs can be fine-tuned to suit a variety of applications. Furthermore, with their inherent crystallinity, confirming small changes to the structure is easily accomplished. In this work, small but distinct changes will be made to MOF structures that dramatically affect MOF stability and MOF adsorption properties. Furthermore, modifications will be made to

MOF structures that influence and affect their performance as filler particles in mixed-matrix membranes.

Chapter 2 summarizes a first study that investigates the stability of anionic MOFs in humid conditions as a function of countercation identity. Chapters 3 and 4 present collaborative work performed with the membrane team at the National Energy Technology Laboratory (NETL). MOFs were synthesized and systematically modified for use as filler particles in mixed-matrix membranes (MMMs). The exterior functional groups present on the outer surface of MOF crystallites were modified to tune the interaction between the MOF and the polymer membrane and the ultimate performance properties of the MMM. However, chapter 3 is a proof of concept work with a glassy polymer and hygroscopic MOF. Chapter 4 presents a different approach to eliminate the polymer/particle defects in MMMs with "real world" advantages of flexible and tunable polyphosphazene polymers and SIFSIX-Cu-2i MOF, which has high CO_2 selectivity over N_2 and H_2O.

2.0 Effect of Countercation on the Water Stability of an Anionic Metal-Organic Framework

This work, written in collaboration with Nathaniel Rosi*, was published in Crystal Engineering Communication, 2017, 19, 5417.[69]

2.1 Introduction

Metal-organic frameworks (MOFs) have myriad potential applications, many which derive from or exploit their inherent porosity.[70] Many of these applications require retention of porosity in the presence of either water liquid or vapor.[45, 71] The water stabilities of many of the most canonical MOFs (e.g. dMOFs,[48, 53, 72-74] UiO MOFs,[17, 48, 49, 51, 54, 75] IRMOFs,[76-83] ZIFs,[82-84] etc.) have now been studied and documented. Not surprisingly, these studies conclude that multiple factors can influence MOF stability in water, including the nature of the metal-ligand bonds and other structural and compositional aspects, such as pore diameter and ligand functionality. One of the more important conclusions, upon review of this literature, is that MOF water stability is nuanced: in some cases, MOFs retain their structure and porosity upon exposure to certain amounts of water or water vapor, but certain threshold amounts can have deleterious effects.[78]

Decorating MOF scaffolds with hydrophobic functional groups has proven an effective means of improving MOF stability in water liquid and water vapor.[53, 54, 72, 81] Many MOFs are intrinsically ionic and have counterions residing in their pore space. Ion exchange can be used to tune their porosity and functionality. It stands to reason that the water stability of ionic MOFs may also be adjusted via ion exchange. For example, introduction of more hydrophobic ions may improve water stability. It may also be possible to introduce multiple different ions into a MOF, some that improve stability in water and others that tailor the MOF for a specific application. In this study, we explore how countercation identity influences the water stability of **bMOF-1**, an anionic MOF having the general formula $Zn_8(ad)_4(BPDC)_6O \bullet$ 2 cations (ad = adeninate; BPDC = biphenyldicarboxylate).[85] We explore a selection of 'hydrophobic' and 'hydrophilic' ammonium-based countercations and study how each affect **bMOF-1** stability in water. Our

results show that the identity of the ammonium-based countercation significantly affects **bMOF-1** water stability. Larger and more hydrophobic alkylammonium cations generally improve water stability compared to smaller and more hydrophilic cations. Importantly, we show that mixtures of hydrophobic and hydrophilic cations can still engender stability to water, depending on the ratio of the two cations. Collectively, these studies illustrate a straightforward method for adjusting the water stability of ionic MOFs.

2.2 Results and Discussion

We chose **bMOF-1** (**I**) for these studies because i) the DMA cations can be quantitatively exchanged by a wide variety of organic and inorganic cations; and ii) our preliminary studies have shown that native **I** [$Zn_8(ad)_4(BPDC)_6O$• 2 DMA] crystals are marginally stable in liquid water, based on comparison of PXRD patterns collected before and after water soaking. The following panel of alkylammonium cations were selected to adjust the 'hydrophobic/hydrophilic' character of the MOF and to determine how factors such as cation size and cation functionality affect the relative stability of **bMOF-1** during exposure to water liquid or vapor: DMA, TMA, TEA, TBA, and TEHMA (Figure 2.1). Cation exchange experiments were performed to yield **II** (**TMA@bMOF-1**), **III** (**TEA@bMOF-1**), **IV** (**TBA@bMOF-1**), and **V** (**TEHMA@bMOF-1**).

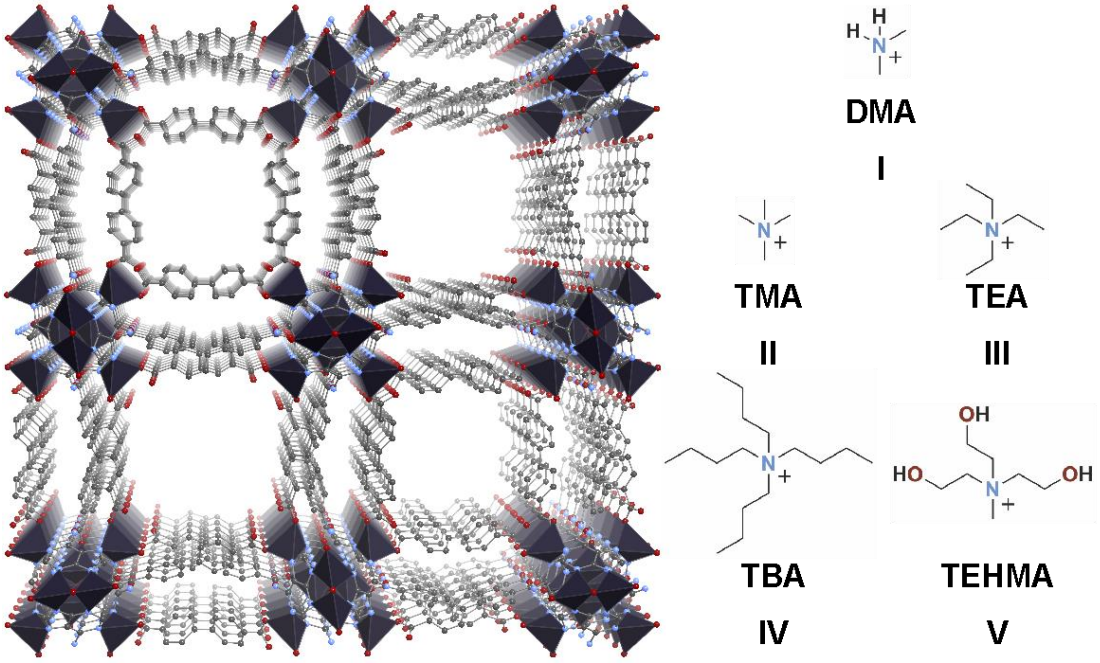

Figure 2.1 Anionic **bMOF-1** with cations shown for **I-V**. (Zn^{2+}, blue polyhedra; C, dark grey spheres; O, red spheres; N, light blue spheres. H atoms omitted for clarity).

^{1}H NMR spectroscopy of dissolved samples of **I-V** was used to determine their precise composition and to verify that DMA was replaced with the new cation (Table 2.1). Furthermore, PXRD was employed to verify retention of crystallinity after cation exchange (Figure 2.2). As is evident from this data, the powder patterns for I-V are in agreement with the simulated pattern, confirming that crystallinity is retained through the process of cation exchange.

Table 2.1 ^{1}HNMR data for the integration of cations in **bMOF-1** samples **I-V**.

bMOF-1 Sample	Cation (Protons integrated in *italic*)	Delta shift (ppm)	H's	Cations per Formula Unit*
I	$NH_2(CH_3)_2^+$	2.55	2.8	0.47
II	$N(CH_3)_4^+$	3.10	6.0	0.50
III	$N(CH_2CH_3)_4^+$	1.20	6.4	0.53
IV	$N(CH_2CH_2CH_2CH_3)_4^+$	0.97	5.2	0.43
V	$N(CH_3)(CH_2CH_2OH)_3^+$	3.10	1.8	0.60

*Formula unit for **bMOF-1** is $Zn_2(ad)_1(BPDC)_{1.5}O_{0.25}$ which corresponds to ~0.5 cation.

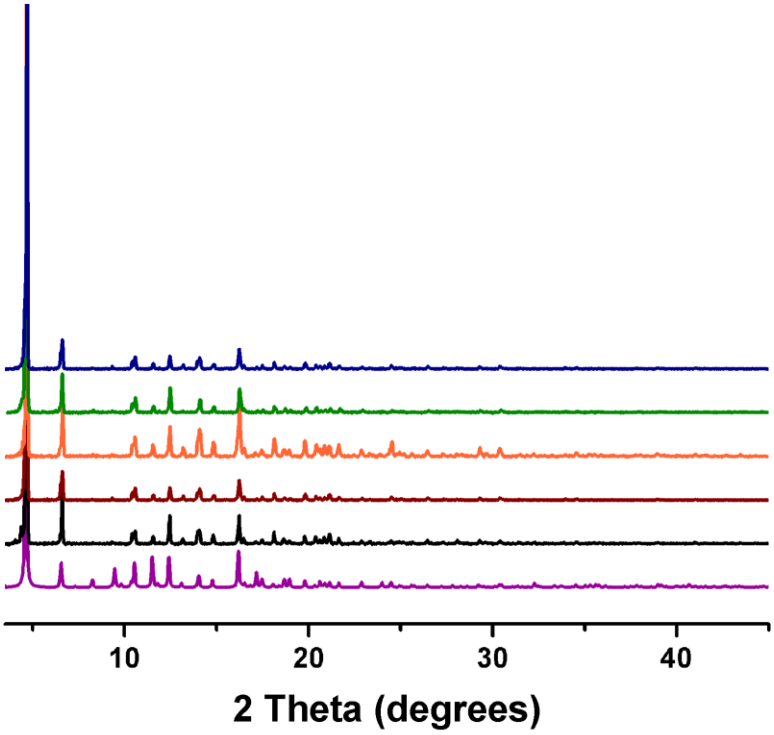

Figure 2.2 PXRD patterns for **I** (black), **II** (red), **III** (orange), **IV** (green), and **V** (blue) compared to the simulated pattern (purple).

We postulated that the larger ammonium cations with longer alkyl substituents and thus more 'hydrophobic' character might serve to protect **bMOF-1** from water and prevent decomposition, while the smaller cations and hydroxylated cations with more 'hydrophilic' character might result in an obverse effect. We first evaluated the stability of **I-V** after soaking in liquid water for 7 days. Supernatant was analyzed for zinc (II) content using inductively coupled plasma optical emission spectroscopy (ICP-OES). However, all samples fell below the measurement threshold (< 2ppm). PXRD patterns (Figure 2.2ai-ei) for the water-soaked samples reveal that **III** and **IV** largely retain their original crystallinity, while the diffraction patterns for samples **I**, **II**, and **V** indicate a significant loss of long range order, as evidenced by broadening of the [200] diffraction line at 4.63° and either broadening or complete loss of the [220] diffraction line at 6.71° and other high angle diffraction lines from ~7-20°. SEM images of the

crystals, before (Fig. 2.3aii-eii) and after (Fig. 2.3aiii-eiii) water soaking, offer qualitative visual corroboration of the PXRD data. Before soaking, **I**-**V** crystals all exhibit smooth, well-defined facets and edges. After soaking, **III** and **IV** crystals remain visually unchanged, while crystals of **V** show signs of pitting and degradation along the [111] facets and crystals of **I** and **II** show significant cracking and deformation.

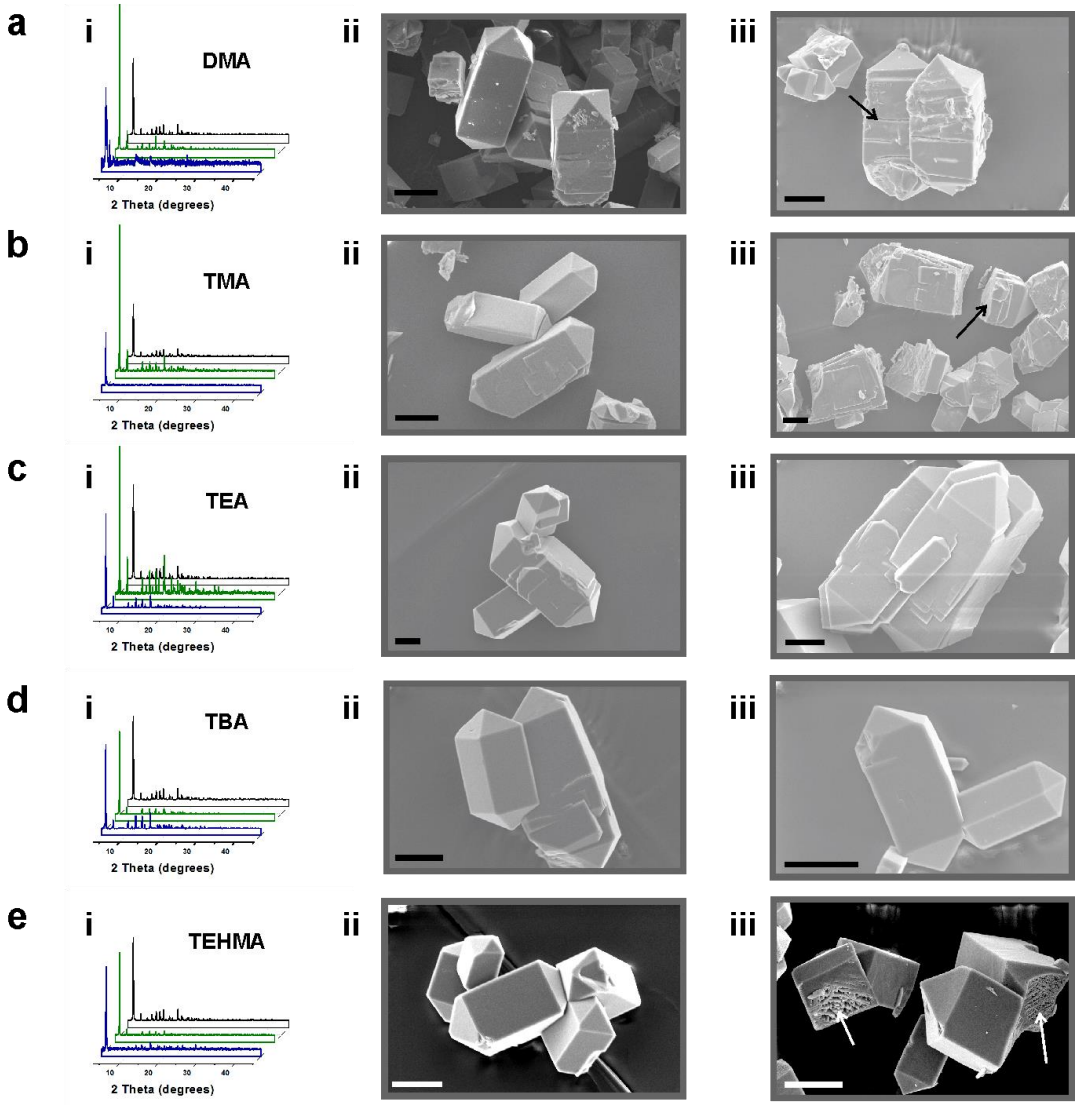

Figure 2.3 PXRD patterns (i) for simulated (black), before water soaking (green), and after water soaking (blue) and SEM images before (ii) and after soaking (iii) for **I** (a), **II** (b), **III** (c), **IV** (d), and **V** (e). Scale bar: 20 μm. Arrows indicate cracks and pitted regions.

N_2 adsorption isotherms (77 K) were collected before and after water soaking to quantitatively assess how liquid water affects the porosity of **I-V** (Figure 2.4). The total N_2 capacity for **I-V** decreases after water soaking, yet each remains microporous.

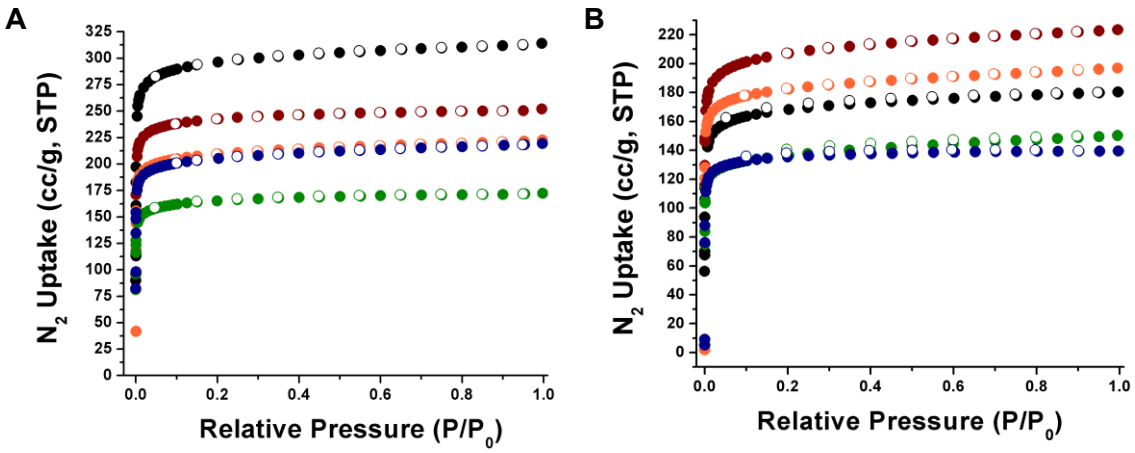

Figure 2.4 N_2 isotherms at 77 K before (A) and after for soaking in water for seven days (B) for **I** (black), **II** (red), **III** (orange), **IV** (green), and **V** (blue).

As the alkyl chain length of the countercation increases (i.e. increasing 'hydrophobic' character), the percent loss of N_2 capacity after water soaking decreases (Figure 2.5). These data correlate well with the observed changes in crystallinity upon water soaking and clearly show that countercation identity affects MOF stability in water. **III** and **V** are loaded with TEA and TEHMA, respectively. We note that TEA and TEHMA are of similar size, but TEA has more 'hydrophobic' character and TEHMA has more 'hydrophilic' character, because it is decorated with three hydrophilic hydroxyl groups. After water soaking, **III** retains 89% of its N_2 capacity while **V** retains only 63%. We speculate that the hydrophilic hydroxyl groups poorly shield the **bMOF-1** scaffold from water, leading to greater structural degradation and significant loss of porosity.

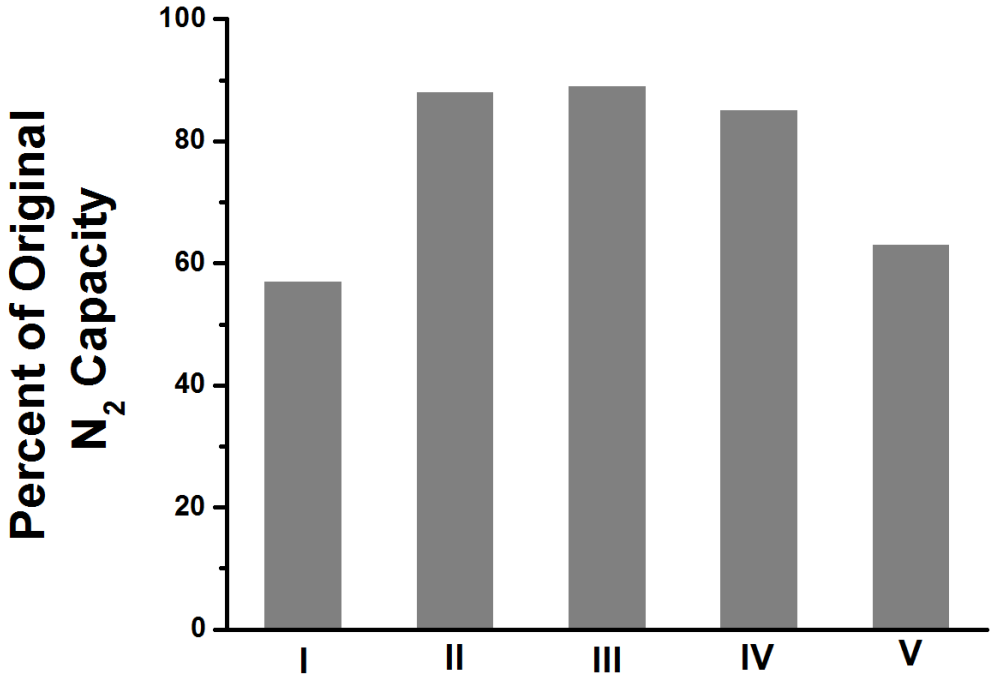

Figure 2.5 Percent of original N_2 capacity after seven days of water soaking for **I-V**.

We next examined MOF stability after exposure to water vapor. First, **I-V** were exposed to doses of water vapor at 293 K up to 90% humidity (Figure 2.6A). After collecting the water vapor isotherms, N_2 adsorption isotherms (77 K) and PXRD patterns were collected. A complete loss of porosity was observed for **I-V** and the PXRD patterns confirmed significant loss of crystallinity, with only **IV** showing some retention of mid- and long-range order (Figure 2.6B).

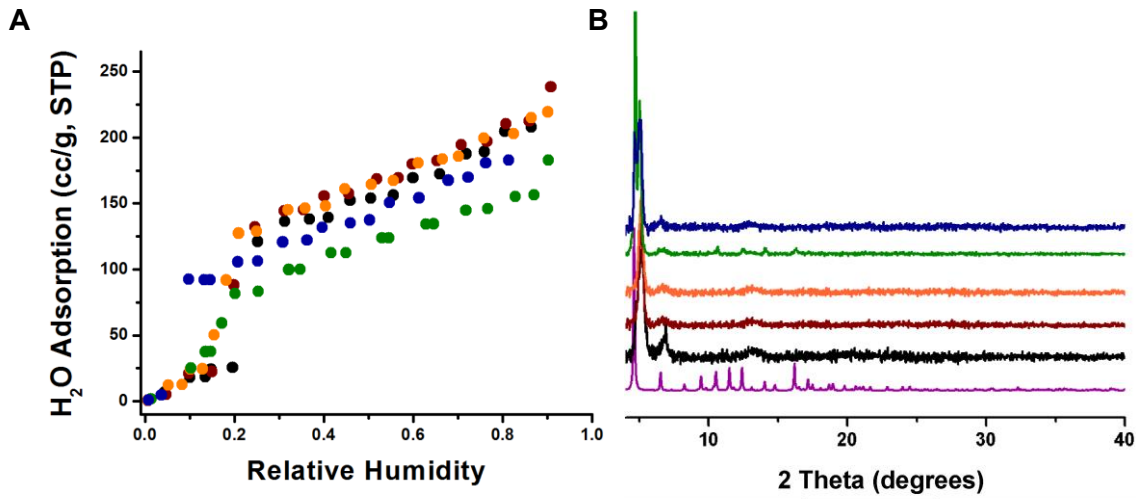

Figure 2.6 Water adsorption isotherms at 293 K taken to 90% relative humidity (A) and PXRD patterns after 90% relative humidity exposure (B) for **I** (black), **II** (red), **III** (orange), **IV** (green), and **V** (blue). PXRD patterns compared to simulated **bMOF-1** pattern (purple).

Given that some reported MOFs are stable up to certain threshold humidity levels, we decided to expose **I-V** to incremental doses of water vapor up to the percent humidity at which the sample loses nearly 100% of its original porosity. Nitrogen isotherms (77 K) were collected after each water vapor adsorption experiment (See Appendix images A1-A5). While no systematic trends are observed, we can conclude that **I-IV** all retain >50% of their original porosity after collection of water vapor isotherms to 15% humidity. After 17.5% humidity, **I-IV** maintained porosity, with **II** and **III** retaining >85% of their original N_2 capacity (Figure 2.7). The porosity of **IV** decreases more significantly than **I-III** after water vapor exposure. At this stage, we can only postulate that this may be due to less favorable packing of the TBA in the pore space, which may allow the water molecules to more easily access the metal ligand framework connections. Significantly, **V** only maintained appreciable porosity after exposure to 5% humidity; it became non-porous after collecting a water vapor isotherm to 7.5% humidity (Figure A5). To summarize, it is clear again that cations with 'hydrophobic' character provide

better protection against water degradation than the hydroxyl-functionalized 'hydrophilic' TEHMA.

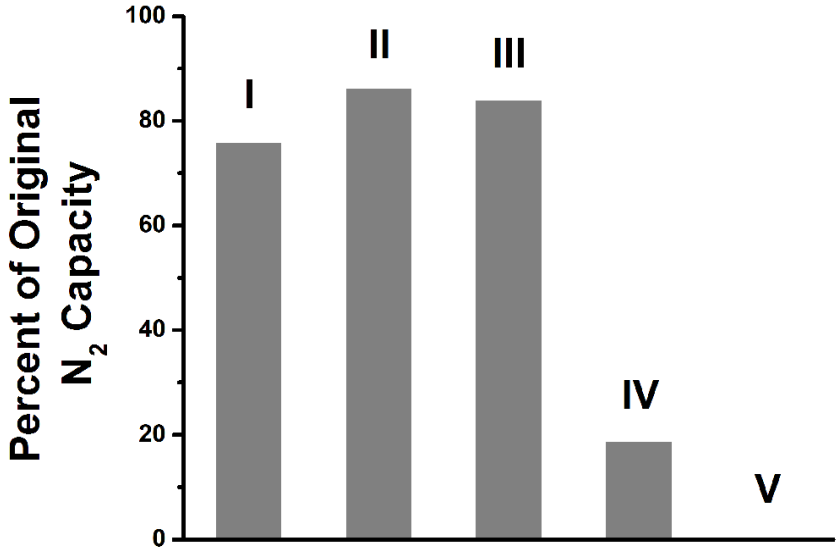

Figure 2.7 Percent of original N_2 capacity after exposure to 17.5% relative humidity for **I-V**.

To assess **bMOF-1** stability after several cycles of water vapor exposure, four consecutive water vapor isotherms were collected for a single sample of **I** to 15% humidity. N_2 isotherms (77 K) were collected after each water isotherm to monitor porosity changes upon cycling (Figure 2.8). The N_2 capacities of **I** after collecting each of the final three water isotherms were all within 22 cc/g of each other, confirming that **I** could be used multiple times at 15% humidity with no appreciable loss of porosity.

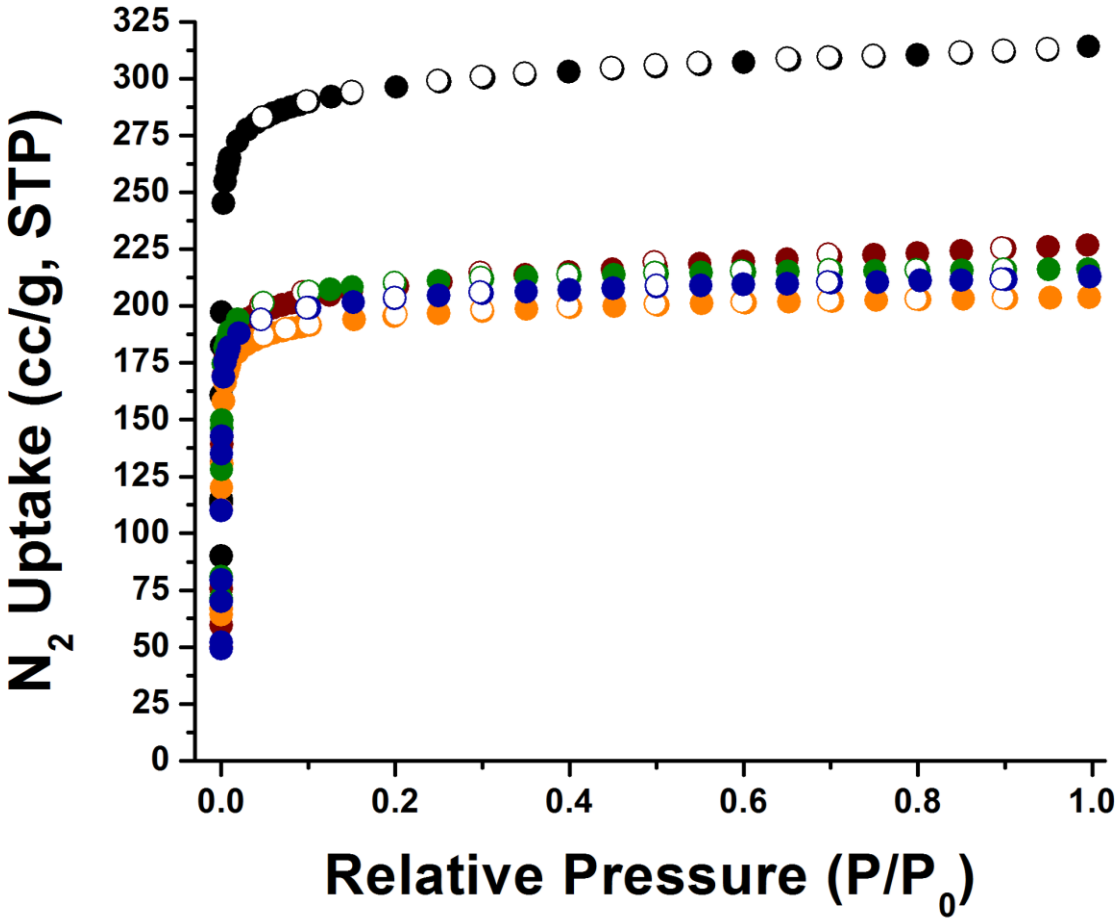

Figure 2.8 N_2 isotherm at 77 K for **I** (before: black) after exposure to 15% humidity four times (red, orange, green, and blue). Some points omitted for clarity due to overlapping plots.

Ion exchange is a facile way of creating new classes of 'multivariate MOFs',[22, 86, 87] where multiplicity is controlled by loading the MOF with more than one type of cation at different controllable ratios. It is reasonable to expect that different mixtures of cations and different ratios of sets of cations may result in different MOF properties. Here, we demonstrate this concept by loading **bMOF-1** with different ratios of TEA and TEHMA and evaluating MOF stability after exposure to water vapor. Three multivariate samples of **TEA/TEHMA@bMOF-1** were prepared with the following TEA:TEHMA ratios: 1.2:1 (**VI**), 3.2:1 (**VII**), and 1:1.5 (**VIII**).

TEA and TEHMA were specifically chosen because of their similar size yet contrasting functionality (Table 2.2). Water isotherms for **VI-VIII** were collected step-wise to 7.5%, 10%, and 12.5% humidity (Figure 2.9). After exposure to 7.5% humidity, no significant loss in porosity was observed for any of the samples. Recall that **V**, which contains 100% TEHMA, experiences complete loss of porosity after 7.5% humidity exposure. These data indicate that TEA can still prevent MOF decomposition, even when it is present in smaller amounts than the hydrophilic TEHMA. At higher humidity, the MOFs with more hydrophobic character (**VI** and **VII**) retain more of their original porosity compared to **VIII**. These studies show that minority amounts of cations having 'hydrophobic' character can significantly improve MOF water stability. The key implication of these findings is that ionic MOFs bearing multiple different counterions can be designed, where each counterion performs a specific task or provides a different function. For example, one counterion could be used to render the MOF selective toward CO_2 adsorption, while a second counterion, present in small amounts, could improve MOF stability in humid conditions.

Table 2.2 Ratio amounts of TEA and TEHMA in **VI-VIII**.

bMOF-1 Sample	TEA H's	TEHMA H's	Ratio of TEA : TEHMA
VI	3.5	0.72	1.2 : 1
VII	5.1	0.4	3.2 : 1
VIII	3.3	1.2	1 : 1.5

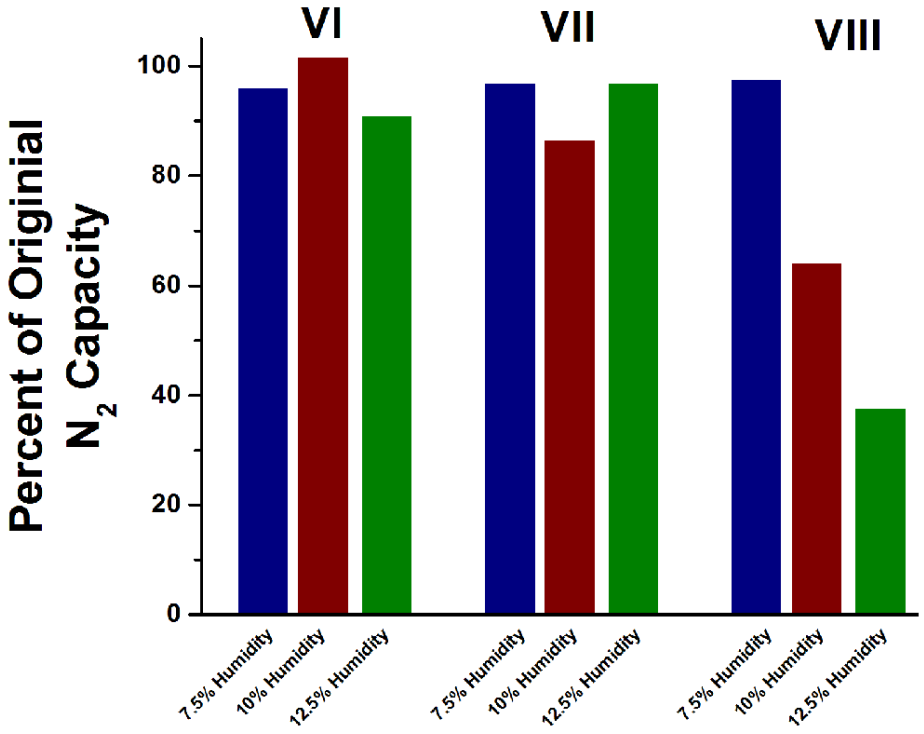

Figure 2.9 Percent of original N_2 capacity for **VI-VIII** after exposure to 7.5% (blue), 10% (maroon), and 12.5% (green) relative humidity.

2.3 Conclusion

We have shown that the water stability of anionic MOFs can be systematically tuned via choice of organic countercation. This MOF modification approach only affects the pore environment and results in no change to the MOF scaffold (metal, ligand, or metal-ligand connectivity). Importantly, we demonstrated that two functionally disparate cations can be incorporated into a MOF at different ratios and that the presence of minority fractions of hydrophobic cations can result in significantly improved water stability. Collectively, these results indicate that counteraction identity can dramatically affect the properties of anionic MOFs and that multivariate anionic MOFs may exhibit a rich diversity of properties that derive not only from their counteraction(s) composition but also the relative amounts of each cation within MOF.

2.4 Experimental Section

2.4.1 General Procedures

Adenine was purchased from Alfa-Aesar, and all other chemicals were purchased from Aldrich Chemical Co. All chemicals were used as purchased without further purification. Nanopure water (18.2 MΩ) was obtained using a Barnstead DiamondTM System. Powder X-ray diffraction (PXRD) patterns were collected using a Bruker AXS D8 Discover powder diffractometer equipped with a Cu Kα X-ray source at 40 kV, 40 mA. Scan speed and step size were set at 0.2 sec/step and 0.02 °/step, respectively. Prior to analysis, MOF samples were spread evenly onto a glass slide. Sample height was aligned with a laser and data were collected for the desired range, typically $3.5° < \theta < 45°$. Scanning electron microscopy (SEM) images were obtained using a Philips XL-30 field emission scanning electron microscope under BSE mode. Proton nuclear magnetic resonance spectra (^{1}H NMR) were collected on Bruker Avance 300 MHz spectrometers. Chemical shifts are in parts per million using the residual solvent peak as the reference value. The value used for proton spectra is 2.50 ppm for d_6-DMSO. Gas adsorption isotherms were collected on a Quantachrome Autosorb-1 instrument. Approximately 100-160 mg of each sample was added into a pre-weighed sample analysis tube. The samples were degassed at 100 °C under vacuum for ~24 hours until the pressure change rate was no more than 3.0 mTorr/min. A liquid N_2 bath was used for the N_2 adsorption experiments at 77 K. A water/ethylene glycol bath was used for isotherms collected at 293 K. UHP grade N_2 gas adsorbates (99.999 %) were used in this study. Nano-pure water was used for all H_2O vapor adsorption studies.

2.4.2 Synthesis of MOFs and Cations

bMOF-1 (**I**) [$Zn_8(ad)_4(BPDC)_6O \bullet 2$ DMA; DMA = dimethylammonium] was synthesized according to reported protocols.[88]

Triethylhydroxylmethylammonium (TEHMA) iodide was synthesized according to a published protocol.[89] Briefly, triethanolamine (20.1 mmol) was added to 30 mL dichloromethane (DCM) in a 40 mL capped vial. Methyliodide (21.0 mmol) was added, and the resulting solution was stirred at room temperature for 1 hour, and then at 40 °C for 12 hours. Two liquid phases formed over time. The solution was cooled to room temperature, the less dense phase was decanted, and the dense liquid salt was washed with DCM (3x with 3 mL). DCM was removed under vacuum to yield product (16.5 mmol, 82 % yield).

2.4.3 Cation Exchange Experiments

I was soaked in 0.1 M DMF solutions of tetramethylammonium tetrafluoroborate ($TMABF_4$; washed 3x per day for 5 days), tetraethylammonium tetrafluoroborate ($TEABF_4$; washed 3x per day for 7 days), or tetrabutylammonium tetrafluoroborate ($TBABF_4$; washed 3x per day for 12 days) in order to replace the DMA cations to yield **TMA@bMOF-1** (**II**), **TEA@bMOF-1** (**III**), and **TBA@bMOF-1** (**IV**).

TEHMA@bMOF-1 (**V**) was prepared by soaking **I** in a 0.1 M solution of TEHMA iodide in absolute ethanol (EtOH) (washed 3x per day for 5 days).

To prepare the mixed-cation samples, **I** was first exchanged with TEA in DMF (**VI** and **VII**) or TEHMA in EtOH (**VIII**) (washed 3x per day for 3 days). The sample was then soaked with the other cation to yield approximate ratios of TEA:THEMA of 1.2:1 (**VI**), 3.2:1 (**VII**), and 1:1.5 (**VIII**) (TEHMA or TEA, washed 3x per day for 3 days for **VII** and **VIII**, 1 day for **VI**).

I-VIII were washed with EtOH (3x with 3 mL) over the course of 3 days to remove DMF from the pores. All MOF samples were stored on the benchtop under EtOH in capped vials.

The composition of the exchanged products was verified by ^{1}H NMR of dissolved samples. 23 μL of DCl (35 wt% in D_2O) was diluted in 1 mL of d_6-DMSO. ~5 mg of each sample was completely dissolved in 150 μL of diluted DCl and 500 μL of d_6-DMSO. ^{1}H NMR (300 MHz) spectra of dissolved samples were collected at room temperature.

2.4.4 Water Soaking Procedure

I-V were heated to 150 °C for 30 minutes to remove solvent. Samples were dissolved (see procedure above) and ^{1}H NMR was used to confirm removal of solvent. After solvent removal, the MOFs were massed in a 20 mL vial. 1 mL of nanopure water was added for every 0.075 mmol of MOF. The vials were capped and the samples were allowed to soak for seven days. After seven days, they were washed with EtOH (5x with 3 mL) and again after 24 hours (3x with 3mL).

2.4.5 Water Vapor Exposure Experiments

H_2O adsorption isotherms were collected on **I-VIII** at 293 K. Stepwise isotherms were collected at 2.5% humidity increments. After collecting each isotherm, the sample was re-activated, an N_2 adsorption isotherm (77 K) was collected to determine sample porosity. Subsequent H_2O isotherms were collected on the same sample, increasing the final humidity by 2.5% until there was a complete loss of porosity (i.e. negligible N_2 adsorption).

In addition, 4 H_2O adsorption isotherms (293 K; 15% humidity), in sequence, were collected on **I**. **I** was activated after each experiment and an N_2 isotherm (77 K) was collected to determine sample porosity.

3.0 Fabrication of Mixed Matrix Membranes (MMMs) with Improved Gas Separation Properties Using Externally-Functionalized Metal-Organic Framework (MOF) Particles

This work, written in collaboration with Tao Li, Surrendar Venna, Santosh Kumar, Michael Lartey, Hunaid B Nulwala, David Luebke, Erik Albenze, and Nathaniel Rosi*, was published in *Journal of Materials Chemistry A*, **2015**, *3*, 5014[90] (Copyright 2015, Royal Society of Chemistry).

All polymers and MMMs were synthesized by Dr. Surendar Venna at the National Energy Laboratory Technology (NETL). SEM, TGA, permeability, and selectivity studies were also conducted at NETL. Synthesis and PSM procedures of UiO-66-NH_2 MOFs were developed by Dr. Tao Li.

3.1 Introduction

Membranes are an effective and promising route for energy-related applications, such as CO_2 capture from flue-gas or natural gas sweetening. Furthermore, membranes offer the advantages of having low-cost manufacturing and easy processing. However, all membranes have a tradeoff. At a certain point, when a membrane exhibits a higher selectivity for a specific species (i.e. CO_2 over N_2), the permeability of the material decreases. The limit to membrane materials is demonstrated in the Robeson upper bound, which was established phenomenologically in 1991, and updated in 2008.[60] The Robeson upper bound exhibited the ideal combinations of selectivity and permeability for sets of important gas pairs. Once the upper bound is reached, any increase is selectivity is met with decreased permeability, or *vice versa* (Figure 3.1).

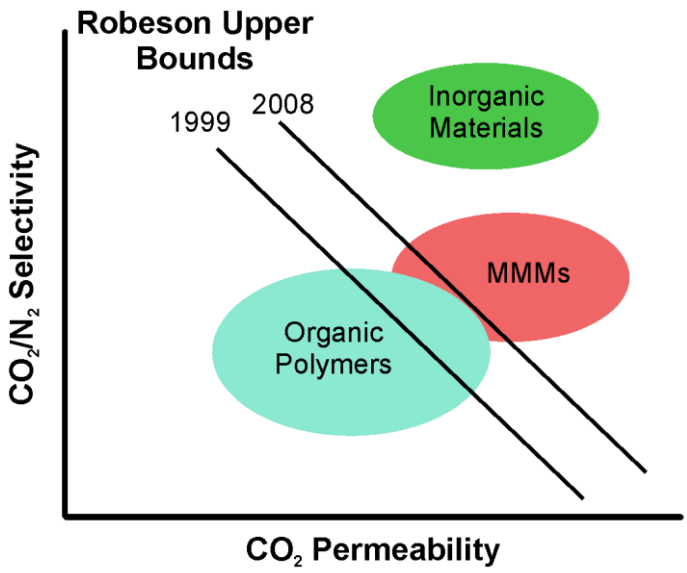

Figure 3.1 Robeson upper bound for CO_2 separation from N_2.

However, the Robeson upper limit rules do not apply to inorganic materials, such as glasses, ceramics, and zeolite membranes. Therefore, these materials could be advantageous in making materials that surpass the Robeson upper bound. Unfortunately, these materials may not

be economically feasible, with high cost of large-scale processing and complicated reproducibility. Many inorganic materials have defects within the structure, which leads to variations to the selectivity and permeability.[91]

With the limitations of inorganic materials in mind, we knew that making a material entirely out of an inorganic phase would not be advantageous for "real-world" use. Therefore, in our work, composite membranes consisting of polymeric materials and inorganic filler particles were synthesized to produce mixed-matrix membranes (MMMs). Ideally, this would allow for a combination of the advantages of the polymer (ease of processing, economically feasible, and, in some cases, flexibility) and the inorganic (favorable separation) phases. MMMs have been used for flue gas separation,[43] water purification,[92] and petrochemical purification.[93] A shortcoming of MMMs is that the filler material can be incompatible with the polymer, leading to defects around the polymer/filler interface. In order to surpass the Robeson upper bound, the polymer/filler interface must be defect free. The defects can be categorized into types: interface voids, which cause increased permeability and decreased selectivity, or particle pore blockage, causing decreased permeability.[94] Defects can be negated *via* better adhesion between the polymer and filler materials. With careful selection of polymer and filler material, better adhesion between the phases of MMMs can be achieved (Figure 3.2).

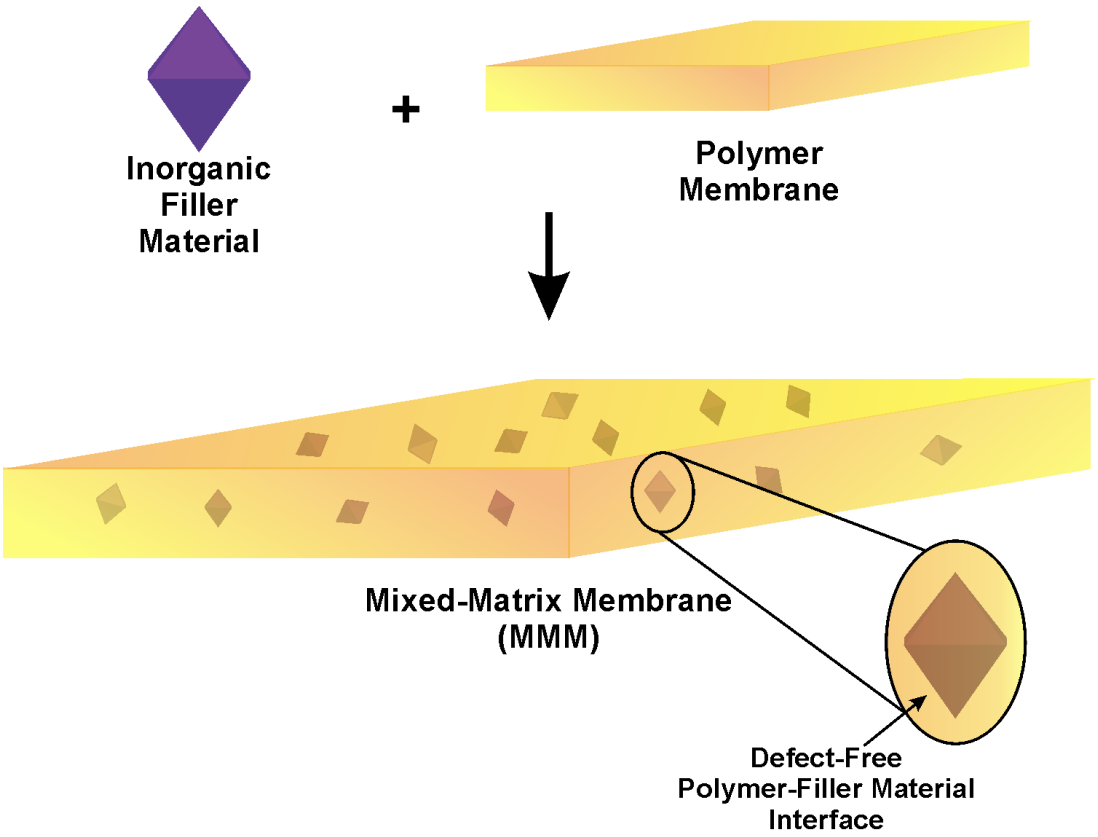

Figure 3.2 Synthesis of MMMs, depicting a defect-free interface between polymer and filler material.

Metal-organic frameworks (MOFs), which exhibit promising separation properties,[25, 26] have been used as filler materials in MMMs in the past.[41, 42, 62, 95, 96] In the following study, the focus will be on the post-combustion carbon capture separation, specifically CO_2 over N_2. An advantage to using MOFs as a filler material is that MOFs can be tuned, either through post-synthetic modification (PSM), or by selection of the metal ions/linkers during synthesis. The organic/inorganic hybrid nature of MOFs makes them ideal to limit the defects in the polymer/filler interface, because MOFs can be designed to be more compatible with the polymer. PSM surface functionalization of MOFs can lead to fewer interface defects.

In our study, UiO-66-NH_2 was utilized as a filler material. UiO-66-NH_2 offers several advantages such as (i) favorable Lewis acid-base interactions for the selection of CO_2, and (ii) high water, thermal, and chemical stability. It should be noted that while UiO-66-NH_2 does have

high water stability, it is hygroscopic, meaning it will adsorb water. The competing adsorption of water and CO_2 will not be discussed in this work, as the polymer/filler interface is the focus of this study. UiO-66-NH_2 is composed of $Zr_6O_4(OH)_4$ clusters bridged together by twelve 2-amino-1,4-benzenedicarboxylate (NH_2-BDC) linkers. It is permanently porous, and cavities within the structure are accessible through ~0.6 nm triangular windows (Figure 3.3).

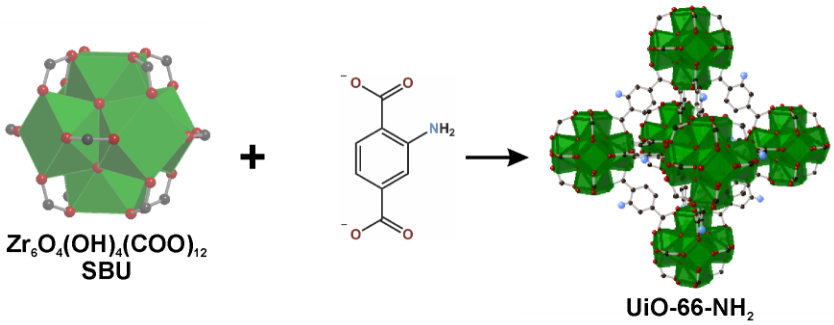

Figure 3.3 Structure of UiO-66-NH_2. (Zr^{4+}, green polyhedra; C, dark grey spheres; O, red spheres; N, blue spheres. H atoms omitted for clarity).

Post-synthetic surface modification on UiO-66-NH_2 was then achieved. As the name suggests, this modification was conducted only on ligands residing on the outside surface of the MOFs. This allowed for the surface functionalized MOFs to have similar capability in capturing and separating CO_2, because the core of each MOF would remain unfunctionalized. Surface modification would only affect the interface between the MOF and polymer. By having four MOF surfaces to investigate with similar interior properties, the polymer/filler (i.e. MOF) interface will be the only variable in this study. In other words, we are tuning the compatibility of the MOF with the polymer *via* surface PSM. UiO-66-NH_2 (I) was modified with aromatic (I_{PA}), non-polar (I_{C10}), or polar (I_{SA}) functionality on its surface. The gas diffusion and selectivity of the MMMs were studied to observe how each functional group effects the polymer/filler interface.

This study utilized Matrimid® as the continuous matrix. Matrimid® is a well-characterized glassy polymer. The glassy nature of Matrimid® makes adding filler particles more difficult because of the incompatibility and rigidity of the membrane. With this difficulty in mind, if this route to limit the interface defects is effective with Matrimid®, it could be used in MMMs containing higher-quality polymers. The limitations of Matrimid® as a real-world polymer for CO_2 separations will be discussed further in chapter 4.

3.2 Results and Discussion

3.2.1 UiO-66-NH_2 and Surface Functionalization

I was modified with a phenyl acetyl group (PA), a decanoyl acetyl group (C_{10}), or a succinic acid group (SA) (Figure 3.4) using straightforward acyl chloride-amine condensation or acid-amine condensation reactions.

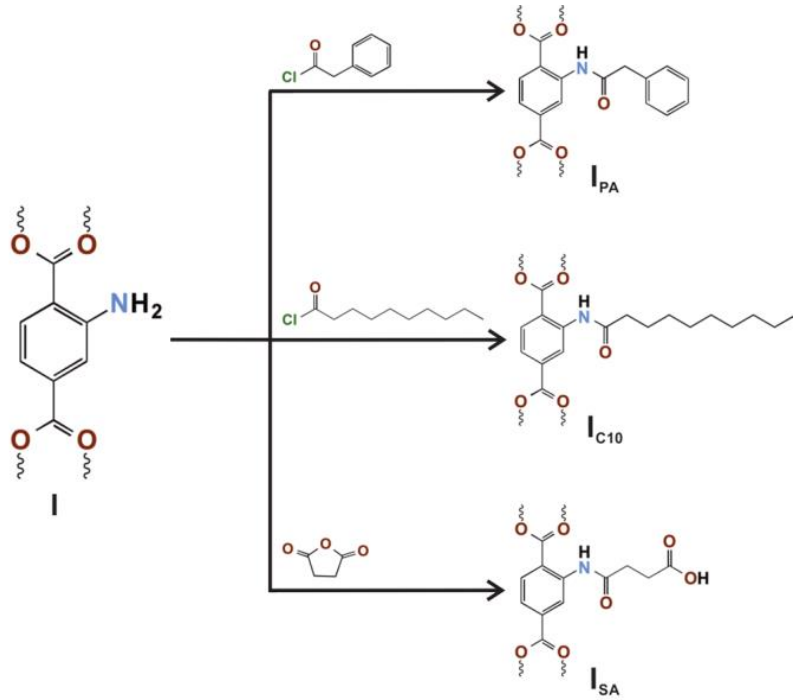

Figure 3.4 Post-synthetic modification of UiO-66-NH_2 (**I**) for functionalization of BDC-NH_2 ligand.

Powder X-Ray diffraction (PXRD) patterns of **I** before and after functionalization are

shown in Figure 3.5a. The diffraction lines are in good agreement with the simulated XRD pattern, confirming formation of the pure phase crystalline **I**. PXRD patterns of $\mathbf{I_{PA}}$, $\mathbf{I_{SA}}$, and $\mathbf{I_{C10}}$ were also consistent with the pattern of **I**, confirming that the crystallinity was maintained even after surface functionalization. SEM images of each of the MOF analogues were used to determine the average particle size. The average particle size of all these MOF analogues was ~200 nm and aggregation was observed. An SEM image of $\mathbf{I_{PA}}$ particles is shown in Figure 3.5b as an example; no changes in the particle morphology were observed after the modification. The observed BET surface area for $\mathbf{I_{PA}}$ is similar to that for **I**, which is consistent with this interpretation. The BET surface area for $\mathbf{I_{C10}}$ is lower than $\mathbf{I_{PA}}$, and therefore significantly lower than **I**. It is clear from our results that the SA groups react significantly with internal amino sites, because 16-32% of the ligands are functionalized with SA (*vide infra*). SA is smaller than phenylacyl chloride and decanoyl chloride, and its reaction with the internal amino groups would not be nearly as diffusion limited. The BET surface area for $\mathbf{I_{SA}}$ is significantly lower than **I**, which, again, is consistent with the observed degree of functionalization (*vide infra*). The N_2 isotherms collected at 77K for **I**, $\mathbf{I_{PA}}$, $\mathbf{I_{SA}}$, and $\mathbf{I_{C10}}$ are shown in Figure 3.5c. Type I isotherms were observed confirming the microporous nature of the materials. The apparent surface area of **I** was 1135 m^2/g, which is similar to previous reports. The BET surface areas of $\mathbf{I_{PA}}$ and $\mathbf{I_{C10}}$ were each slightly lower than **I** (1079 m^2/g for $\mathbf{I_{PA}}$ and 962 m^2/g for $\mathbf{I_{C10}}$) while that for $\mathbf{I_{SA}}$, 827 m^2/g, was significantly lower than **I**, for reasons described above. The BET surface areas for the functionalized analogues indicate that these samples have accessible internal surface, and they are consistent with the observed degree of functionalization for each of these samples.

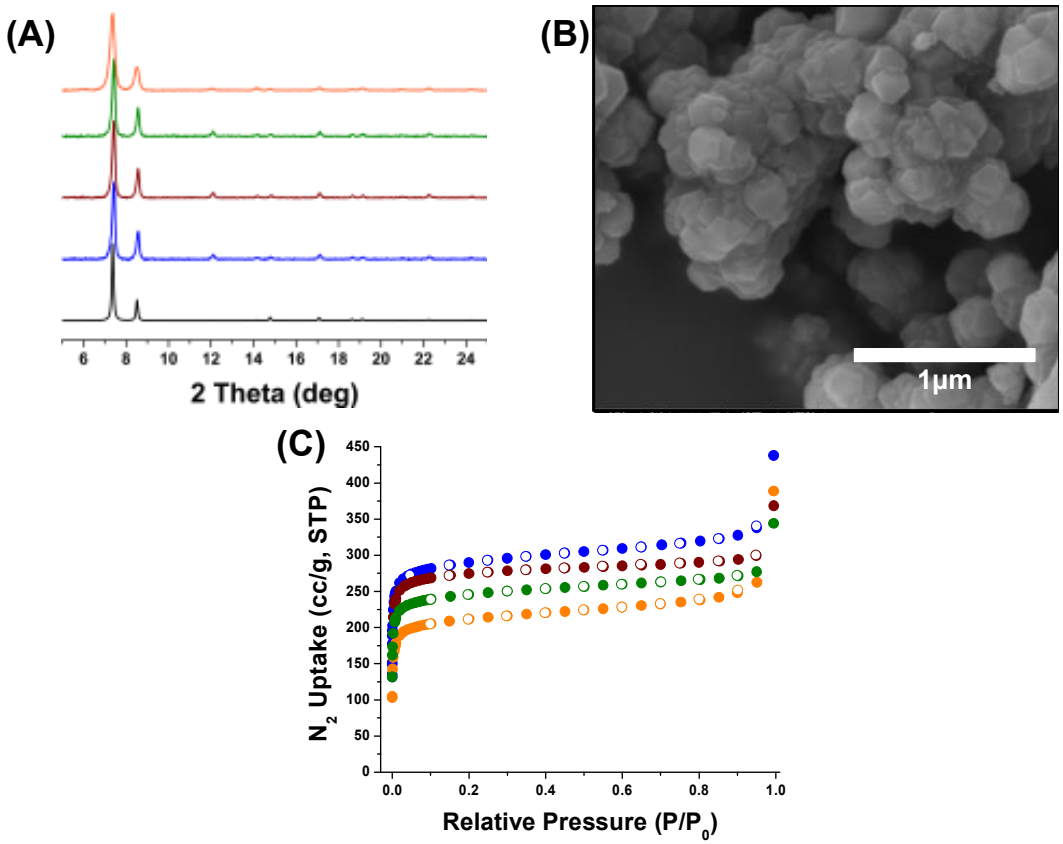

Figure 3.5 PXRD patterns (A), sample SEM image for $\mathbf{I_{PA}}$ (B), and N_2 isotherms at 77 K for **I** (blue), $\mathbf{I_{PA}}$ (maroon), $\mathbf{I_{C10}}$ (green), and $\mathbf{I_{SA}}$ (orange).

The composition of $\mathbf{I_{PA}}$, $\mathbf{I_{SA}}$, and $\mathbf{I_{C10}}$ was determined by collecting LCMS, XPS and ^{1}H NMR spectra for digested MOF samples. Data analysis details are included in the experimental section. Briefly, LCMS studies confirmed the presence of both functionalized and unfunctionalized ligand for $\mathbf{I_{PA}}$, $\mathbf{I_{SA}}$, and $\mathbf{I_{C10}}$. ^{1}H NMR (See Appendix, Figures A6-A9 and Tables A1-A4) was used to determine the ratio between unfunctionalized and functionalized ligand for $\mathbf{I_{PA}}$, $\mathbf{I_{SA}}$, and $\mathbf{I_{C10}}$. The percentage of functionalized ligands was found to be between 2-6% for $\mathbf{I_{PA}}$, 2-5% for $\mathbf{I_{C10}}$, and 16-32% for $\mathbf{I_{SA}}$. We expect that, for $\mathbf{I_{PA}}$ and $\mathbf{I_{C10}}$, the phenyl substituents and C_{10} chains are located on the external surface of the MOF particles, because functionalization at internal amino sites would be significantly limited by diffusion of the large phenyl and C_{10} reactants. XPS analysis of the functionalized MOFs were conducted by NETL

before and after crushing. XPS data indicated that the organic ligand functionalization was likely predominantly on the external surface of the MOF particles.

CO_2 isotherms for each sample were collected at 273 K and 298 K (See Appendix Figures A10 and A11). The amount of CO_2 adsorbed at 273 K and 298 K for each material corresponds closely to the observed BET surface areas for these materials; that is, the larger the BET surface area, the larger amount of CO_2 adsorbed at 1 bar. Along with the CO_2 isotherms, N_2 isotherms were also collected at 273 K and 298 K (See Appendix Figures A12 and A13).

With both CO_2 and N_2 isotherms at the same (ambient) temperatures, a comparison can be made to determine the selectivity factor (*S*) of the MOFs (Figure 3.6). By observing the uptake of each component at their relative percent humidity in flue gas (15 % for CO_2, 0.15 bar; 75% for N_2, 0.75 bar), the ideal selectivity can be calculated used equation 3.1

$$S = \frac{n_{CO2}/n_{N2}}{x_{CO2}/x_{N2}} \tag{3.1}$$

where *n* is number of mols adsorbed and *x* is the partial pressure of each gas. For each MOF, the selectivity is above 15 at 298 K. With a relatively high selectivity factor, each of these MOFs should be efficient materials for a filler in the Matrimid® MMMs. The only factor that should affect the application properties of the MMMs should be the polymer-MOF interface, because all of the MOFs have similar performance.

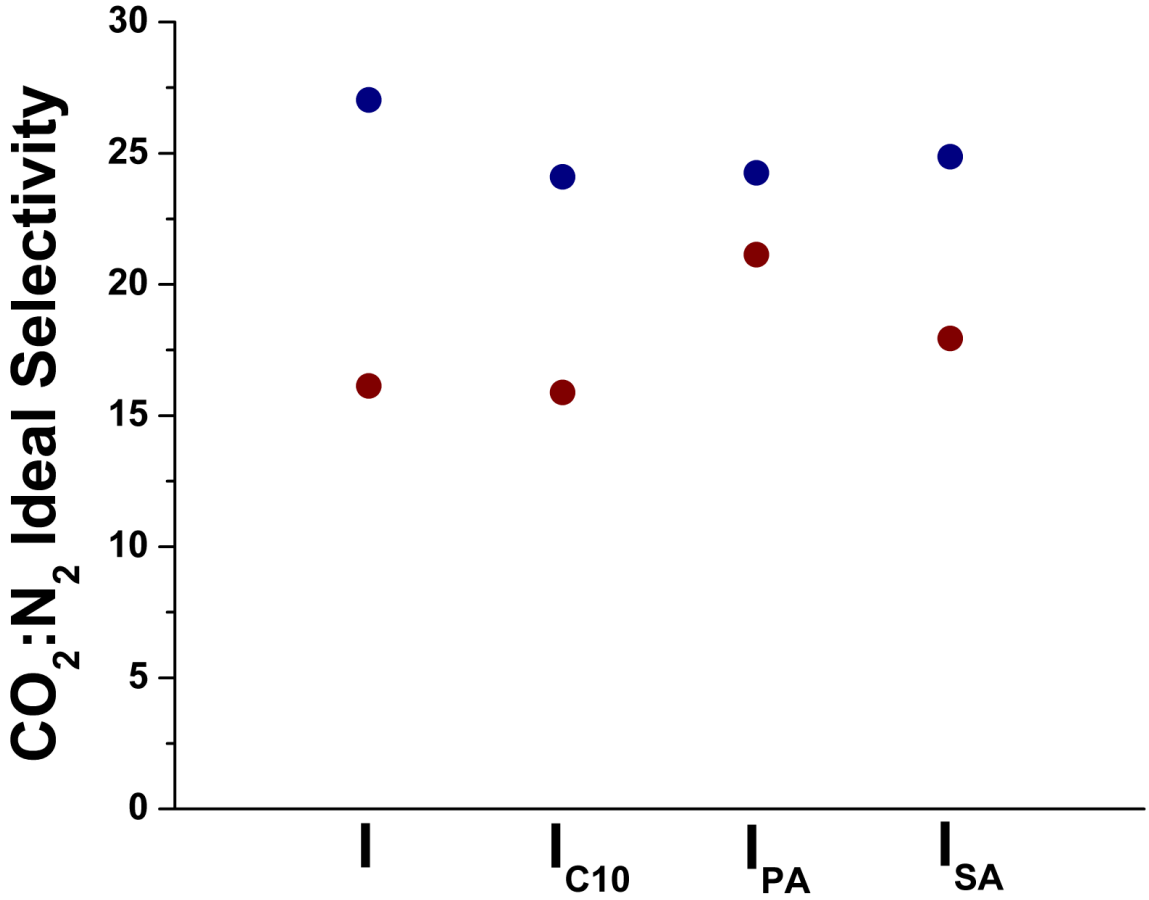

Figure 3.6 Ideal selectivity of **I** and post-synthetically modified **I** at 273K (blue) and 298K (red).

3.2.2 Matrimid® and MMM Characterization

Neat dense Matrimid® membranes and Matrimid®/MOF MMMs were prepared and analyzed using PXRD. The PXRD patterns were used to confirm the presence of UiO-66-NH_2 analogues in the MMMs as shown in Figure 3.7. The most evident diffraction lines observed for the MMMs match those for the neat MOFs, which confirms the preservation of the crystal structure after incorporation of the MOF particles in the Matrimid® polymer matrix.

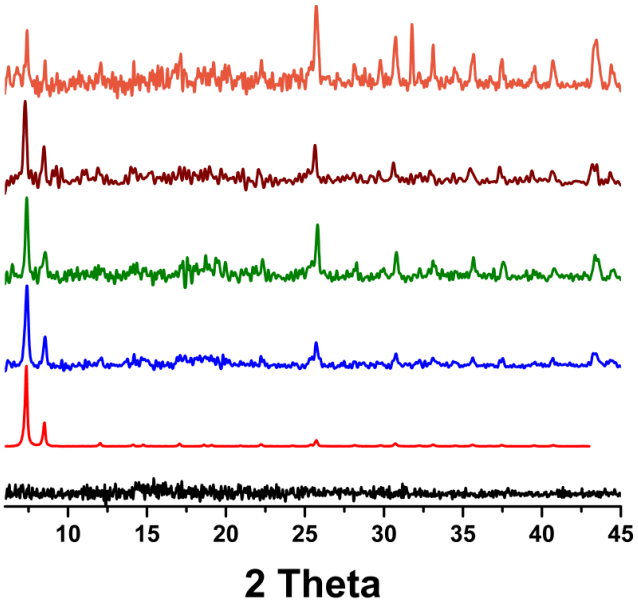

Figure 3.7 PXRD patterns for Matrimid® (black), **I** (red), MMM containing **I** (blue), $\mathbf{I_{PA}}$ (green), $\mathbf{I_{C10}}$ (maroon), and $\mathbf{I_{SA}}$ (orange) confirm the existence of MOF in the MMMs.

Thermograms obtained for **I**, $\mathbf{I_{PA}}$, $\mathbf{I_{SA}}$, and $\mathbf{I_{C10}}$ after soxhlet extraction are shown in Figure 3.8A. The initial weight loss observed for all the MOF samples is attributed to adsorbed water, because UiO-66-NH_2 is hygroscopic. The weight loss around 200-300 °C is attributed to residual DMF in the pores. The observed weight loss at higher temperatures corresponds to the decomposition of the ligand. The neat Matrimid® and MMM films were also studied using TGA to determine the effect of the MOF particles on the thermal stability of the membranes. The weight loss as a function of temperature is shown in Figure 3.8B-D. The thermal decomposition of neat Matrimid® begins around 440 °C. Overall, thermogravimetric analyses of the MMMs showed minimal weight loss up to 300 °C indicating that the casting solvent was not trapped in the pores of the MOF. The decomposition of MMMs with a moderate loading of 23 wt% MOF is shown in Figure 3.8B. The thermograms are very similar, indicating that the surface functionalization of **I** has minimal effect on the decomposition of the MMM. This is in agreement with the results for the neat MOFs. Figures 3.8C and D show the effect of loading on the decomposition temperature of the MMMs. For both cases, **I** and $\mathbf{I_{PA}}$, the decomposition

temperature of the MMM decreased with increased loading. Usually the decomposition temperature of a MMM increases with an increase in the MOF loading because the interaction between the Matrimid® and MOF particle restricts the thermal motion of polymer. This restricted motion increases the energy needed for the movement and segmentation of polymer chains, which enhances the thermal stability of the membranes. The results presented here show the opposite trend of a decreasing decomposition temperature with increased loading. This trend occurs because the decomposition temperature of the MOF is substantially lower (by more than 100 °C) than that of the Matrimid®. The decomposition of the MOF analogues in the MMMs begins at ~300 °C, much earlier than Matrimid®. Similar trends were reported for $Cu_3(BTC)_2$ MOF based MMMs.[95]

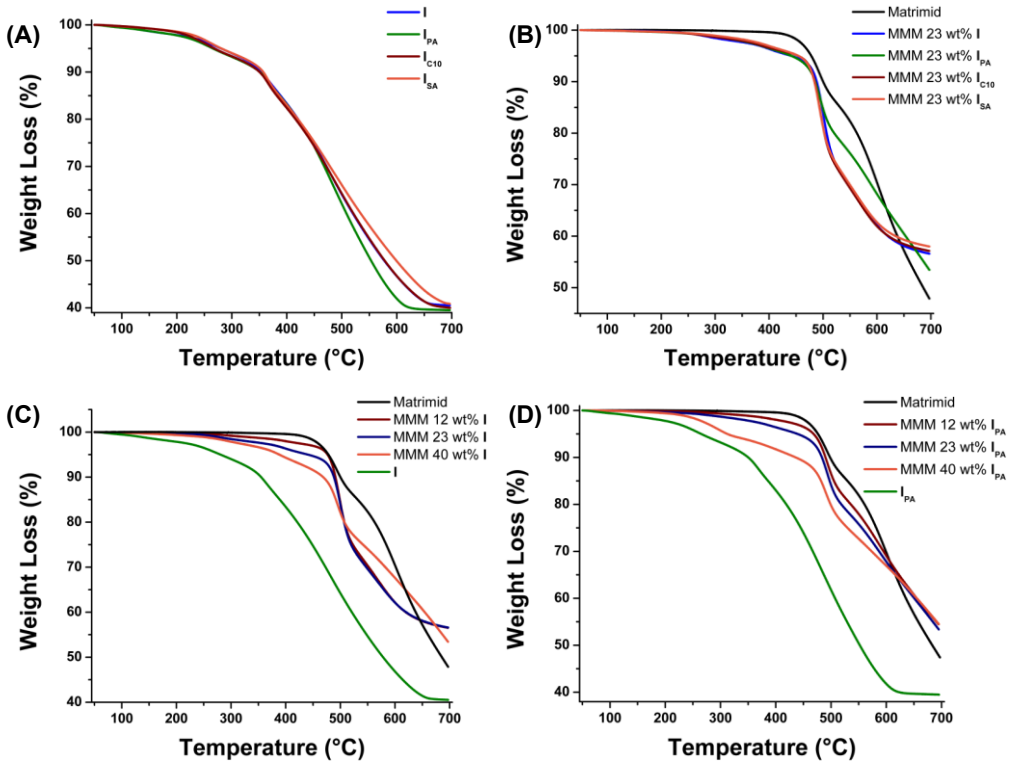

Figure 3.8 Thermogravametric analysis of MOF analogues (A), 23 wt% loaded MMMs (B), MMMs containing varying amounts of **I** (C), and MMMs containing varying amounts of $\mathbf{I_{PA}}$ (D).

SEM was used to study the membrane cross section morphology as well as to image the particle-polymer interface. Figure 3.9A shows an SEM image of a cross-section of a neat Matrimid® membrane. Its surface is very smooth without any noticeable defects, which is characteristic of a dense Matrimid® membrane. Representative cross sectional images of the MMMs with 12, 23 and 40 wt% of $\mathbf{I_{PA}}$ are shown in Figures 3.9B-D, respectively. From the images, no obvious defects around the $\mathbf{I_{PA}}$ particles were observed. At low to moderate loadings (12 and 23 wt%) the $\mathbf{I_{PA}}$ particles were typically well-dispersed. However, at high loadings (40 wt%), several large clusters of particles exist. These clusters range in size from 500 nm to several microns. Aggregated clusters often contain nonselective diffusion paths between the individual crystallites which reduces the overall performance of the membrane.

A second important feature of the SEM micrographs is the scalloped morphology observable for the MMMs that is not present for the neat Matrimid® membrane. This morphology is typically attributed to the formation of elongated polymer segments with increased plastic deformation of the polymer, and is taken as an indication that there is good interaction between the polymer and filler. The absence of any observable sieve-in-a-cage morphology or cavity formation at each loading is an indication of good film formation and strong interaction between the Matrimid® and $\mathbf{I_{PA}}$ particles. There was no easily observable difference between the cross-sectional images of **I**, $\mathbf{I_{PA}}$, $\mathbf{I_{SA}}$, and $\mathbf{I_{C10}}$ loaded MMMs. More sophisticated techniques like nano-computed tomography scanning (nano-CT) or positron annihilation lifetime spectroscopy (PALS) are needed to detect if there are any nano-defects or rigidification of the polymer around the particle. Therefore, in order to test the polymer-MOF interface, the separation factors for the MMMs must be studied. There was no physical difference in the SEM images, and the selectivity of the MOFs alone were similar, therefore, to

adsorption properties are going to determine if the surface modification influenced the polymer-MOF interface.

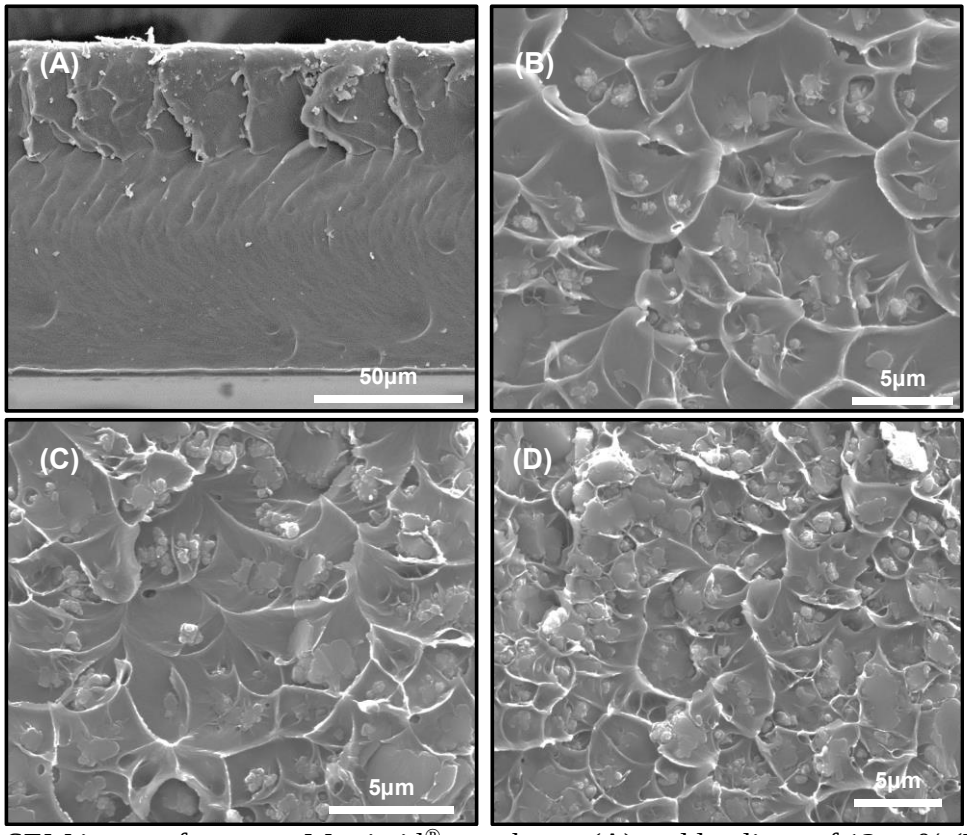

Figure 3.9 SEM images for a neat Matrimid® membrane (A) and loadings of 12 wt% (B), 23 wt% (C), and 40 wt% (D) of $\mathbf{I_{PA}}$ in Matrimid®.

3.2.3 CO_2/N_2 Gas Separation Performance of MMMs

Pure gas CO_2 and N_2 permeation measurements of neat Matrimid® and the MMMs were completed using an isochoric permeation system at room temperature and 20 psia pressure. The results are presented in Figures 3.10 and 3.12. All membranes were tested twice to check the reproducibility and determine the percent error, which was 2-5% for both the permeability and ideal selectivity. The dense Matrimid® membrane showed a CO_2 permeability of 8.5 Barrer with a CO_2/N_2 ideal selectivity of 29, in agreement with previously reported values.

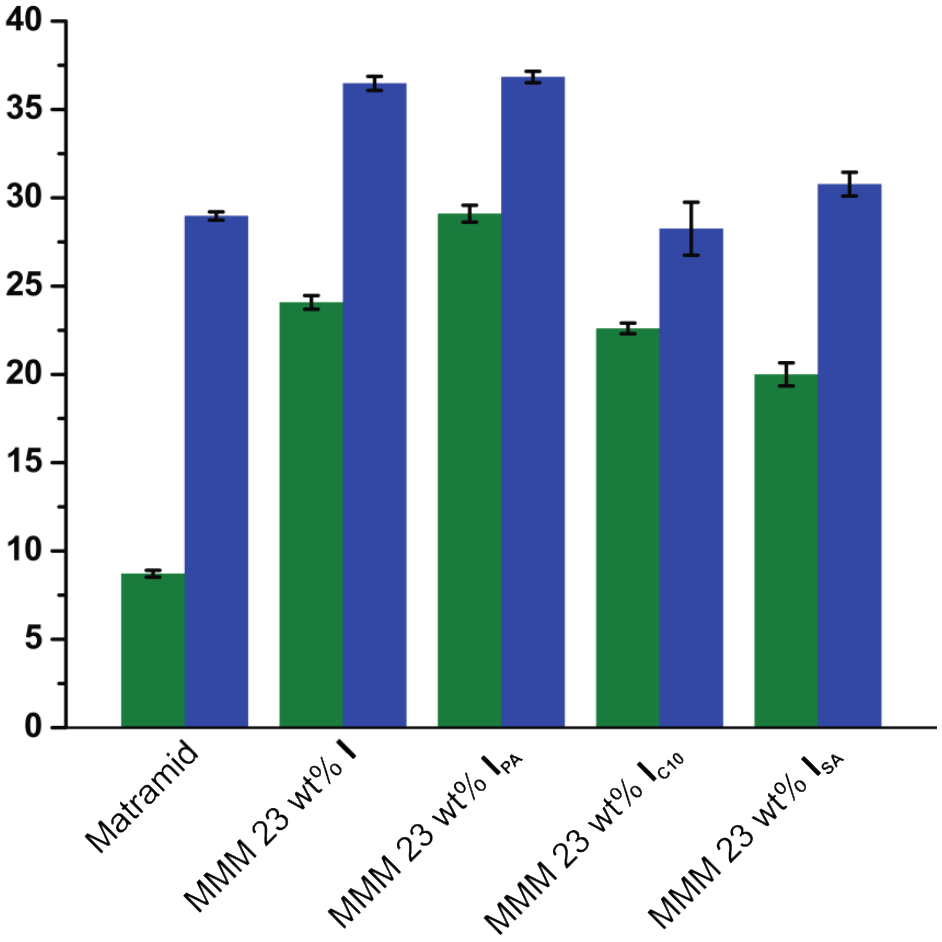

Figure 3.10 CO_2 permeability (green, in Barrer) and CO_2:N_2 ideal selectivity (blue) for Matrimid® as well as MMMs containing 23 wt% of the functionalized MOFs.

Figure 3.10 presents the permeability and ideal selectivity results for the MMMs with 23 wt% loading of all four MOF analogues. In all cases, the CO_2 permeability increased dramatically compared to the value for the neat Matrimid® polymer. In fact, the CO_2 permeability increased as much as four times upon incorporation of the MOF particles. In addition to a substantial increase in the permeability, the MMMs with **I** and $\mathbf{I_{PA}}$ filler particles also exhibited an increase in selectivity compared to the neat Matrimid® film. This improvement in ideal selectivity is attributed to the formation of a defect-free interface between the particle and polymer. Alternatively, the improved ideal selectivity may be attributed to significant

rigidification of the polymer around the particle. Such rigidification would lead to increased ideal selectivity but decreased gas permeability. In the case of the Matrimid®/**I** and Matrimid®/$\mathbf{I_{PA}}$ membranes presented here, the overall permeability increased substantially indicting this scenario is unlikely. It should be noted that UiO-66-NH_2 provides minimal molecular sieving selectivity because its pore size (6-7 Å) is larger than the kinetic diameter of both CO_2 (3.3 Å) and N_2 (3.64 Å). However, it is expected that UiO-66-NH_2 and the analogues used here may provide selectivity towards CO_2 due to a surface diffusion mechanism since CO_2 adsorbs more favorably the MOF compared to N_2. Overall, these results are promising, especially compared to previous MMM work with other MOFs.

The transport properties for the MMMs with the $\mathbf{I_{SA}}$ and $\mathbf{I_{C10}}$ surface-functionalized MOFs are also shown in Figure 3.10. The $\mathbf{I_{SA}}$ MMMs showed only slight improvement in ideal selectivity over pure Matrimid®, while $\mathbf{I_{C10}}$ showed a decrease in ideal selectivity. These membranes were also the most fragile and difficult to handle, with $\mathbf{I_{SA}}$ yielding the most brittle membrane.

The decreased transport properties and fragile nature resulting from the SA and C_{10} surface functional groups are interesting because they indicate that the MOF filler does not interact as strongly with the polymer matrix resulting in unobservable defects at the Matrimid®/MOF interface. These defects increase the brittleness of the membrane and act as non-selective alternate diffusion paths for the gases, resulting in the decreased transport performance. This decreased performance can be predicted by examining the structure of Matrimid®, which contains aromatic and imide groups. The surface functional groups (SA – polar; C_{10}– non-polar alkyl) are not expected to interact well with the functional groups in the Matrimid® polymer.

Conversely, for $–NH_2$ and –PA surface-functionalized MOFs of **I** and $\mathbf{I_{PA}}$, respectively, the aromatic groups present in the polymer are expected to interact favorably through π-π stacking with the aromatic ring of the –PA group and the imide groups in the polymer are expected to interact strongly with the $–NH_2$ groups and amide linkages through hydrogen bonding as shown in Figure 3.11. Furthermore, since all four MOF analogues have *nearly* identical internal structure and functionality (we note that $\mathbf{I_{SA}}$ has significant internal SA functionalization) and only differ by the organic moiety present at the surface, it can be concluded that simply changing the surface organic moiety can significantly affect whether the polymer/filler interface is truly defect-free.

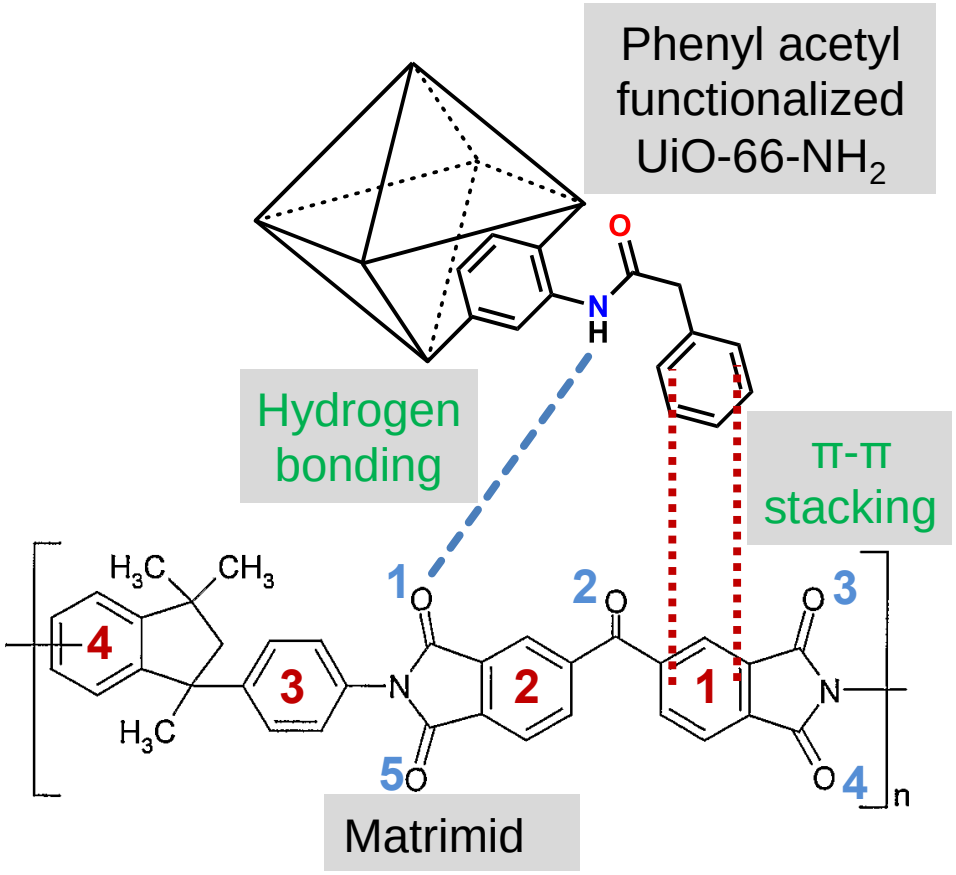

Figure 3.11 Scheme demonstrating the favorable interactions between Matrimid® polymer and $\mathbf{I_{PA}}$ based on surface functionality.

Additional MMMs were fabricated for the two best performing MMMs, those containing

I or $\mathbf{I_{PA}}$ MOF particles, with MOF loadings of 12 wt% and 40 wt%. The results, along with those for the 23 wt% loading, are shown in Figure 3.12. As expected, both the permeability and the ideal selectivity increase with loading up to 23 wt%. However, for the 40 wt% loadings, further increase in the permeability was observed, but the ideal selectivity values decreased compared to the 23 wt% loading. This is attributed to the agglomeration observed at the higher loading as shown in Figure 3.7D. The agglomerated clusters result in microvoids which act as non-selective diffusion pathways for the gas molecules resulting in a lower observed ideal selectivity.

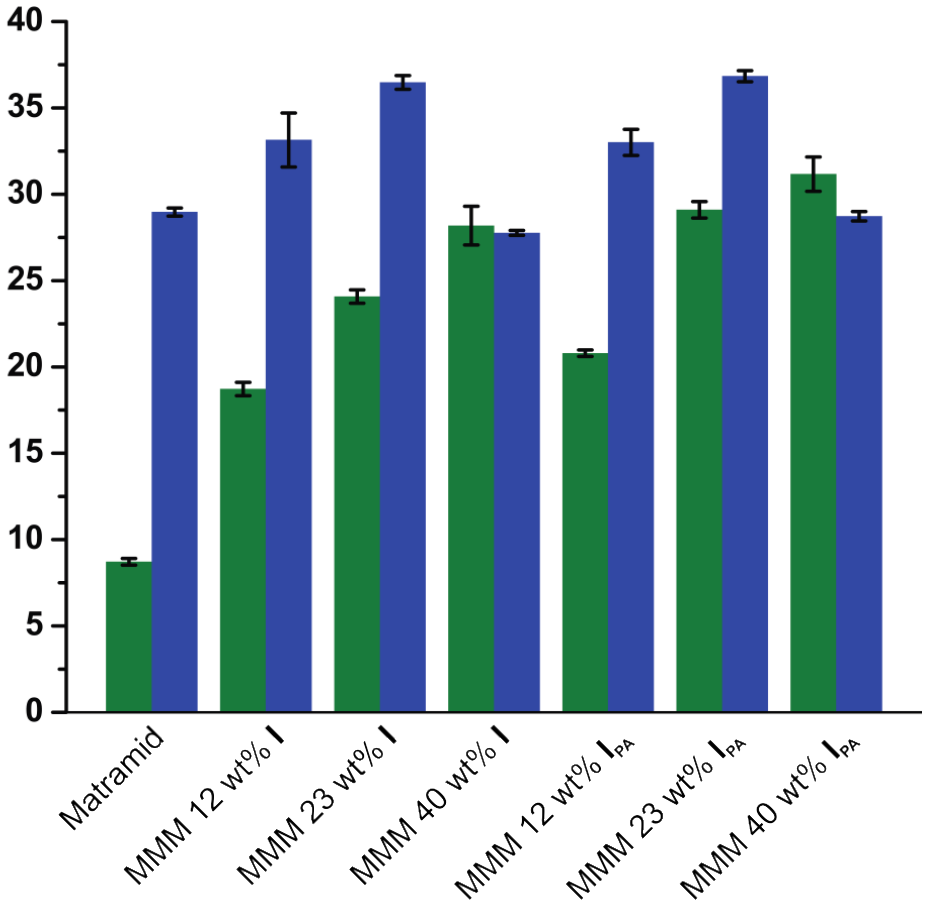

Figure 3.12 CO_2 permeability (green, in Barrer) and CO_2:N_2 ideal selectivity (blue) for 12, 23, and 40 wt% loadings of **I** and $\mathbf{I_{PA}}$.

3.3 Conclusion

Herein, we have shown a route to synthesizing mixed-matrix membranes (MMMs) that eliminate polymer/filler defects; namely surface modification to the filler particle. Through post-synthetic modification (PSM) of UiO-66-NH_2, the surface was functionalized with aromatic, non-polar, and polar groups. The aromatic group had the best adhesion to the Matrimid® polymer because of π-π stacking and hydrogen bonding.

Each of the surface functionalized MOFs had similar surface areas and selectivity factors, therefore, the only variable being examined was the polymer/filler interactions. UiO-66-NH_2 does have limitations in use for CO_2 separation in flue gas due to its hydroscopic nature. Even though the polymer (Matrimid®) used in this study has limited the effectiveness of "real-world" applications, this proof of concept report demonstrated that using surface PSM can be used for better polymer/filler interactions for MOFs

3.4 Experimental Section

3.4.1 Matrimid®

Matrimid® 5218 polymer was obtained from Huntsman Chemical. All other chemicals were purchased from Sigma Aldrich Chemical and were used as received without any further purification.

3.4.2 Preparation and Modification of MOFs

3.4.2.1 UiO-66-NH_2 Synthesis

UiO-66-NH_2 (I) synthesis was adapted from reported syntheses. Stock solutions of $ZrCl_4$ (0.1 M), 2-aminoterephthalic acid (0.1 M), and HCl (conc.) (1 M) in DMF were first prepared. To a 40 mL vial were added 10 mL $ZrCl_4$ (1 mmol), 20 mL 2-aminoterephthalic acid (2 mmol), and 3 mL HCl (3 mmol). The vial was capped and heated in a 120 °C oven for 24 hours. Yellow

microcrystalline product was centrifuged (5 min, ~1000 rpm) and washed first with DMF (3X) and then with $CHCl_3$ (3X). The product was then dried in a 130 °C oven (24 h), collected, and stored in a capped vial and used for subsequent functionalization steps without further purification.

3.4.2.2 Modification of I with Phenyl Acetyl Group (I_{PA})

I (2.0 g, 0.64 mmol) was suspended in $CHCl_3$ (20 mL) in a 40 mL vial. While stirring, phenylacetyl chloride (1.5 mL,11.4 mmol) and triethylamine (1.4 mL,10 mmol) were added and the resulting mixture was allowed to stir at room temperature (16 h). The yellow product was centrifuged (5 min, ~1000 rpm), washed with $CHCl_3$ (3X), and dried in a 130 °C oven (16 h). The product was stored in a capped vial.

3.4.2.3 Modification of I with Decanoyl Acetyl Group (I_{C10})

I (2.0 g, 0.64 mmol) was suspended in $CHCl_3$ (20 mL) in a 40 mL vial. While stirring, decanoyl chloride (2.4 mL, 11.4 mmol) and triethylamine (1.4 mL, 10 mmol) were added and the resulting mixture was allowed to stir at room temperature (16 h). The yellow product was centrifuged (5 min, ~1000 rpm), washed with $CHCl_3$ (3X), and dried in a 130 °C oven (16 h). The product was stored in a capped vial.

3.4.2.4 Modification of I with Succinic Acid Group (I_{SA})

I (2.0 g, 0.64 mmol) was placed in dry DMF (20 mL) with 3Å molecular sieves (~5-10 sieves dried for 2d at 200°C and then evacuated prior to use). While stirring, succinic anhydride (2.0 g, 19.9 mmol) was added and the mixture was heated in a 60 °C oil bath (16 h). The yellow product was centrifuged (5 min, ~1000 rpm), washed with DMF (3X), washed with $CHCl_3$ (3X), and then dried in a 130 °C oven (16 h). The product was stored in a capped vial.

3.4.3 Membrane Fabrication

For preparation of the neat Matrimid® dense membrane, Matrimid® was dried in a vacuum oven at 120 ℃ overnight. Next, a dope solution was formed by dissolving the Matrimid® in chloroform followed by mixing on a roller mixer. The dope was kept stationary overnight to remove any retained gas bubbles. Prior to casting, a glove bag was purged with N_2 to remove any humidity and was saturated with chloroform to slow the rate of solvent evaporation from the membrane. Matrimid® dense membranes were cast onto a glass plate in the glove bag using a casting knife. The resulting membrane was kept for 2 days in the glove bag as the chloroform evaporated slowly from the membrane. The Matrimid® membrane was dried at 100 ℃ overnight followed by annealing at 225 ℃ in a vacuum oven for 2 hours. Finally, the membrane was slowly cooled to room temperature. To ensure full activation of the UiO-66-NH_2, Soxhlet-extraction was employed to extract any residual DMF from the MOF framework. The sample was loaded in the Soxhlet extraction apparatus and extracted for 7 days, using dichloromethane as the extracting agent. For preparation of the MMMs, both the Matrimid® and MOF were dried in a vacuum oven at 120 ℃ overnight.

Preparation of the dope solution followed the standard ‘priming’ technique in which the MOF particles were first dispersed in chloroform solvent using an ultrasonication water bath for 2 hours to obtain a homogenous dispersion. Next, the MOF crystals were primed by adding 30% of the total polymer to the MOF solution followed by roller mixing and sonication for another 2 hours. The remaining polymer was added in two steps (30% and 40%) followed by stirring and sonication after each addition. The mixed matrix dense films were formed by casting the mixed matrix dope as discussed above for the neat membranes. The MOF loading was controlled by changing the mass ratio of MOF to polymer in the mixed matrix dope solution. MMMs with low

(12 wt%), medium (23 wt%), and high (40 wt%) loadings of MOF were fabricated using **I** (MMM-I), $\mathbf{I_{PA}}$ (MMM-I_{PA}). MMMs were also prepared using 23 wt% $\mathbf{I_{SA}}$ (MMM-I_{SA}) and 23 wt% $\mathbf{I_{C10}}$ (MMM-I_{C10}) to study the effect of different surface functionalizations on the Matrimid®/MOF filler adhesion and the gas separation performance. The loadings represented here – 12 wt%, 23 wt%, and 40 wt% – correspond to volume percentages of approximately 11%, 22% and 38%, respectively.

3.4.4 Characterization of MOFs

Powder X-Ray diffraction (PXRD) was used to verify the phase purity and homogeneity of the MOF samples. Each pattern was collected using a Bruker AXS D8 Discover powder diffractometer at 40 kV, 40 mA for Cu Kα, (λ = 1.5406 Å) with a scan speed of 0.20 sec/step and a step size of 0.02018°. The simulated powder pattern was calculated using Mercury 2.4 software.

Liquid chromatography-mass spectrometry (LCMS) was used to confirm that **I** was successfully functionalized to yield $\mathbf{I_{PA}}$, $\mathbf{I_{C10}}$, or $\mathbf{I_{SA}}$. For LCMS, ~5 mg of MOF sample was digested in a solution of MeOH/HF/H_2O (500 μL MeOH and 5 μL of 48% HF in H_2O). The mixture was shaken to dissolve the MOF. Analyses were performed on a Shimadzu LCMS-2020. LC methods were employed using an acetonitrile/water eluent. The flow rate was held steady at 0.2 mL/min and acetonitrile was increased steadily from 10 % to 90 % over 0-9 min and then reduced to 10% acetonitrile for the final minute. The ionization interface was simultaneous ESI & APCI.

^{1}H NMR spectroscopy was used to estimate the degree of functionalization of the post-synthetically modified MOFs. For these studies, ~5mg of MOF sample was digested in a solution of d_4-MeOD/HF/H_2O (500 μL d_4-MeOD and 5 μL of 48% HF in H_2O). The mixture was shaken

to dissolve the MOF. Spectra of dissolved MOFs were collected at room temperature using Bruker Avance 300 MHz spectrometers. The integration for each proton of the H_2-NH_2-BDC ligand was set at 1. Chemical shifts are in parts per million using the residual solvent peak as the reference value. The values used for proton spectra, respectively, are 3.3 ppm for d_4-MeOH.

X-ray photoelectron spectroscopy (XPS) measurement was carried out with a PHI 5600ci instrument using monochromatic Al Kα x-rays. The pass energy of the analyzer was 58.7 eV. The relative amounts of different chemical states of carbon were determined by curve fitting the C 1s spectra using Casa XPS software. A peak at 284.6 eV was used as the binding energy reference and was assigned to C-C and C=C functionalities. A peak at 285.8 eV was assigned to C-O and C-N functionalities, and a peak at 288.6 eV was assigned to carboxyl carbon.

Gas adsorption isotherms were collected volumetrically as a function of relative pressure using an Autosorb 1 from Quantachrome. Activated MOF samples were weighed using an AB54-S/FACT (Mettler Toledo) electrogravimetric balance (sensitivity 0.1 mg). 9 mm large bulb cells (from Quantachrome) of a known weight were loaded with ~60 mg of sample for gas adsorption experiments. The samples were degassed at 150°C for 12-24 hours on the degassing station until the outgas rate was no more than 3.0 mTorr/min. The degassed sample and sample cell were weighed precisely and then transferred back to the analyzer. The temperature of each sample for N_2 adsorption experiments was controlled using a refrigerated bath of liquid nitrogen (77 K). CO_2 and N_2 isotherms (273 K and 298 K) were measured in a temperature-controlled water bath. The N_2 and CO_2 adsorbates were of UHP grade.

Thermogravimetric analysis (TGA) of each MOF sample was performed using a TGA Q500 thermal analysis system. All TGA experiments of MOF samples were performed under a N_2 atmosphere from 25-600 °C at a rate of 5 °C /min.

3.4.5 Characterization of MMMs

TGA was also used to determine the thermal stability of the MMMs and to analyze any remaining solvent in the membranes. The MMM samples were first heated up to 100 °C and kept at 100 °C for 15 min under N_2 atmosphere in order to remove the adsorbed water. The samples were then cooled down to 50°C and the temperature was subsequently increased to 700 °C at a rate of 10 °C/min.

Scanning electron microscopy (SEM) was performed on an FEI Quanta 600 scanning electron microscope to determine the particle size of the MOF crystallites, as well as to evaluate the cross-sectional structure of the fabricated membranes. The membrane samples were prepared by fracturing the membranes in liquid nitrogen and subsequent sputter coating of palladium using a SPI Module Sputter Coater.

The pure gas CO_2 and N_2 permeation tests were performed at room temperature using an isochoric (constant volume, variable pressure) permeation system. Upstream pressures were measured with a pressure transducer (Maximum pressure 150 psia, Viatran Inc., Model-345) and accompanying readout (Dalec Electronics digital panel). Downstream pressures were measured using a Baratron 627D capacitance manometer with a maximum pressure output of 10 Torr (MKS, Wilmington, MA). The downstream volume was calibrated by using a standard simple mole balance method with a known volume of stainless steel balls. The thicknesses of the membranes were measured using a micrometer (Marathon Electronic digital micrometer) several times and the average value was used for the calculation of permeability. The membrane diameter is 1.85 cm and the area is 2.7 cm^2.

Testing was carried out as follows: the membrane was loaded into a Millipore high pressure 25 mm filter holder. The entire permeation system was de-gassed using a vacuum pump

(Edwards nXDS 10i scroll pump) for 18 hours and then the leak rate was measured by isolating the permeation system from the vacuum pump. The leak rate was always much less than the typical steady state pressure rise during gas permeation measurement. The feed gas was then introduced to the upstream side of the membrane, and the pressure rise in the downstream volume was recorded as a function of time. Two film samples were tested at each MOF loading to get average permeation results.

The permeation of a gas through the membrane can be described using the solution-diffusion model. The permeability of a gas, i, is given by: $P_i = D_i \bullet S_i$, where D_i and S_i represent the diffusion and solubility coefficients of component i, respectively. In terms of this model, the productivity of a membrane is defined by the permeability of the gas through the membrane and the ideal selectivity of the membrane is the ratio of the permeabilities of the individual gases. Permeability was calculated by differentiating the pressure rise as a function of time and using equation 3.2.

$$P = \frac{V_d l}{p_2 ART}\left[\left(\frac{dp_1}{dt}\right)_{ss} - \left(\frac{dp_1}{dt}\right)_{leak}\right] \qquad (3.2)$$

Where, V_d= downstream volume (cm^3), l = film thickness (cm), p_2 = upstream absolute pressure (cmHg), A = film area (cm^2), T = Temperature (K), R = gas constant (cm^3cmHg/mol K), $(dp_l/dt)_{SS}$ = rate of downstream pressure rise during testing (cmHg/sec), $(dp_l/dt)_{leak}$ = rate of downstream pressure rise under vacuum (cmHg/sec).

4.0 Polyphosphazene Polymer Development for Mixed Matrix Membranes Using SIFSIX-Cu-2i as Performance Enhancement Filler Particles

This work, written in collaboration with Surrendar Venna, Zhicheng Tian, David Hopkinson, Harry Allcock, David Luebke, Erik Albenze, and Nathaniel Rosi*, was published in in *Journal of Membrane Science*, **2017**, *535*, 103[97] (Copyright 2017, Elsevier).

All polymers and MMMs were synthesized by Dr. Surendar Venna at the National Energy Laboratory Technology (NETL). SEM, TGA, permeability, and selectivity studies were also conducted at NETL.

4.1 Introduction

In our previous study, the major shortcomings of using a Matrimid®/UiO-66-NH_2 MMM in "real-world" conditions were (i) Matrimid® is a glassy polymer that is difficult to modify and handle, and (ii) UiO-66-NH_2, while exhibiting good CO_2 selectivity, is hygroscopic and will have competing adsorption with H_2O in flue gas. With this in mind, the Matrimid®/UiO-66-NH_2 study is proof of concept work that enhancing the polymer/filler interactions can improve overall MMM application properties. Moving into our second generation of MMMs, our goal was to utilize polymers that are more flexible and tailorable and filler-particle MOFs that perform better in "real-world" flue gas conditions.

In this study, a family of polyphosphazene polymers were synthesized for post-combustion CO_2 capture. Polyphosphazenes are hybrid polymers consisting of an inorganic backbone with alternating phosphorus and nitrogen atoms with two side groups (usually organic) attached to each phosphorus atom (Figure 4.1). In recent years, several hundred different polyphosphazenes have been synthesized by macromolecular substitutions. Polyphosphazenes are therefore a tailorable material. For example, polyphosphazenes can be made with a wide range of chemical and physical properties by substituting a large variety of side groups. Furthermore, the phosphorus-nitrogen bonds in the polymers are extremely flexible due to the low torsional energy. With the tenability, high flexibility, and high thermal and chemical stability, Polyphosphazene polymers allow for more variation and better separation compared to the Matrimid® in the previous study.

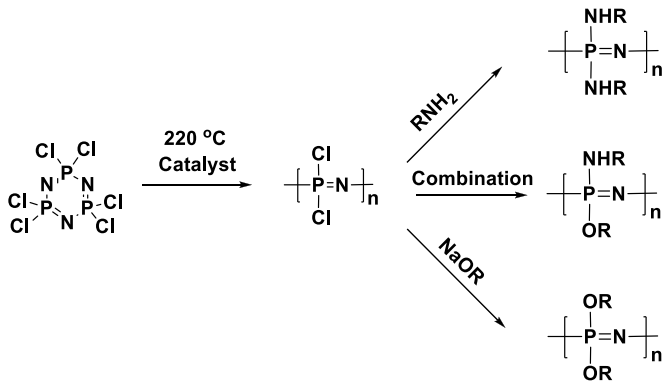

Figure 4.1 Synthesis of polyphosphazene polymer.

Due to their synthetic tunability, backbone chain flexibility, property optimization, and chemical and thermal stability, polyphosphazenes are especially advantageous as polymeric membranes for CO_2 separations. To date there have been relatively few investigations on the development of polyphosphazene polymers for gas separation applications.[98-105] Polyphosphazene membranes were studied for the separation of different gas mixtures and showed a wide range of gas permeability with differing pendant groups such as alcohols, fluorinated alcohols, phenols etc.[101-105] Most significantly, higher CO_2 permeability was observed with mixed pendant functional groups.[99-103] Enhancing membrane permeability can be achieved by addressing either the solubility or the diffusivity of a particular gas through that membrane according to the solution-diffusion mechanism.[106] For example, one study suggested that increased stiffness in the polymer backbone and appropriate inter-chain spacing has the potential of providing increased permeability by increasing diffusivity for a particular gas.[107]

Once again, eliminating interface defects was of paramount importance. We chose a simpler route to approach this issue. Even though surface PSM was effective, by selecting a MOF with similar functionality to the polyphosphazene polymers under investigation, we anticipated a smooth polymer/filler interface. SIFSIX-Cu-2i was chosen as the filler material for this family of membranes. SIFSIX-Cu-2i is a catenated MOF containing Cu^{2+} metal centers

connected by hexafluorosilicate (SiF_6^{2-}) anions and pyridine linkages. SIFSIX-Cu-2i is an ideal filler material because (i) it has high CO_2 selectivity over N_2 and (ii) due to the fluorine functionalization, it is water stable and exhibits low water adsorption,[108] which results in promising post-combustion CO_2 capture over H_2O and N_2. Furthermore, due to the SiF_6^{2-} anions, SIFSIX-Cu-2i will interact well with the polyphosphazene polymer, which could lead to a MMM with fewer defects (Figure 4.2). Due to the incorporation of polymers more apt to "real world" conditions and SIFSIX-Cu-2i exhibiting better CO_2 separation, this family of MMMs reached close to the Robeson upper bound, making them an excellent choice for industrial separation techniques.

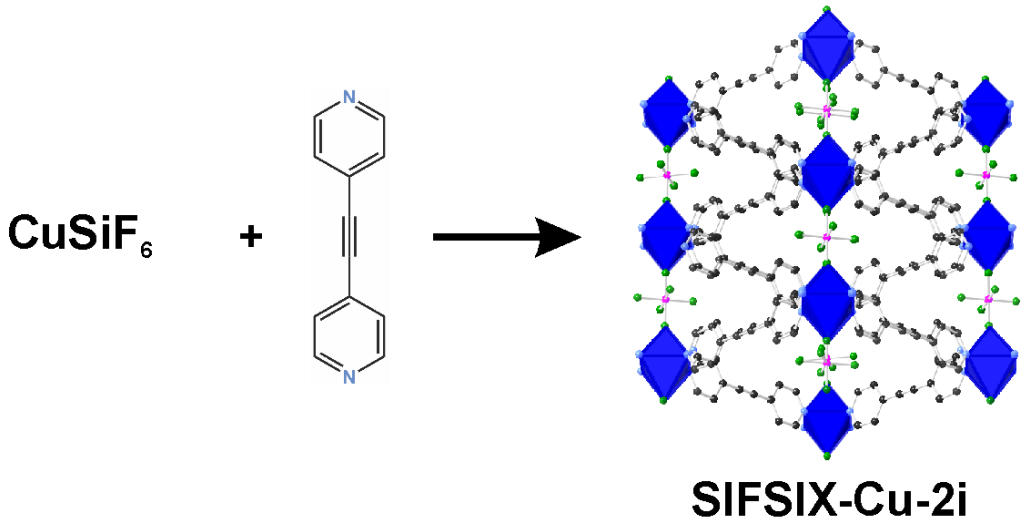

Figure 4.2 Synthesis of SIFSIX-Cu-2i. (Cu^{2+}, blue polyhedra; C, grey spheres; Si, pink spheres; F, green spheres; N, light blue spheres. H atoms omitted for clarity).

4.2 Results and Discussion

4.2.1 SIFSIX-Cu-2i MOF Characterization

The powder X-ray diffraction (PXRD) pattern of the SIFSIX-Cu-2i MOF is shown in Figure 4.3A and the peak positions are in agreement with previously reported data.[109] Figure 4.3B shows the SEM images of the SIFSIX-Cu-2i MOF particles with an average particle size of ~0.1-0.2 μm. The N_2 adsorption isotherms at 77 K of SIFSIX-Cu-2i MOF displayed type-I adsorption isotherms typical of a microporous phase. The Brunauer-Emmett-Teller (BET) surface area was 556 m^2/g with 9.8 Å pore size and pore volume of 0.27 cc/g based on the N_2 adsorption isotherm. Gas adsorption measurements showed that SIFSIX-Cu-2i MOF adsorbs ~4 weight percent CO_2 at 0.15 bar and 13 weight percent at 1 bar. The selectivity for SIFSIX-Cu-2i for CO_2 over N_2 was ~26.5 at 1 bar and 298K. We note that these data are consistent with the reported experimental and computational results.[108, 110] We also calculated the ideal CO_2:N_2 selectivity by comparing uptake at 0.15 bar of CO_2 and 0.85 bar of N_2 using equation 3.1. SIFSIX-Cu-2i MOF showed very high CO_2/N_2 selectivity (~79.7) at these conditions compared to many other MOFs.[25, 90] SIFSIX-Cu-2i unit cell consists of Cu^{2+} metal nodes connected by SiF_6^{2-} anions and linker 1,4-bis(4-pyridyl)butadiyne. The interpenetrated framework, in which two identical unit cells are interwoven, offers improved stability as compared with the non-interpenetrated phase, as well as improved CO_2 affinity due to constriction of its pore size.[109]

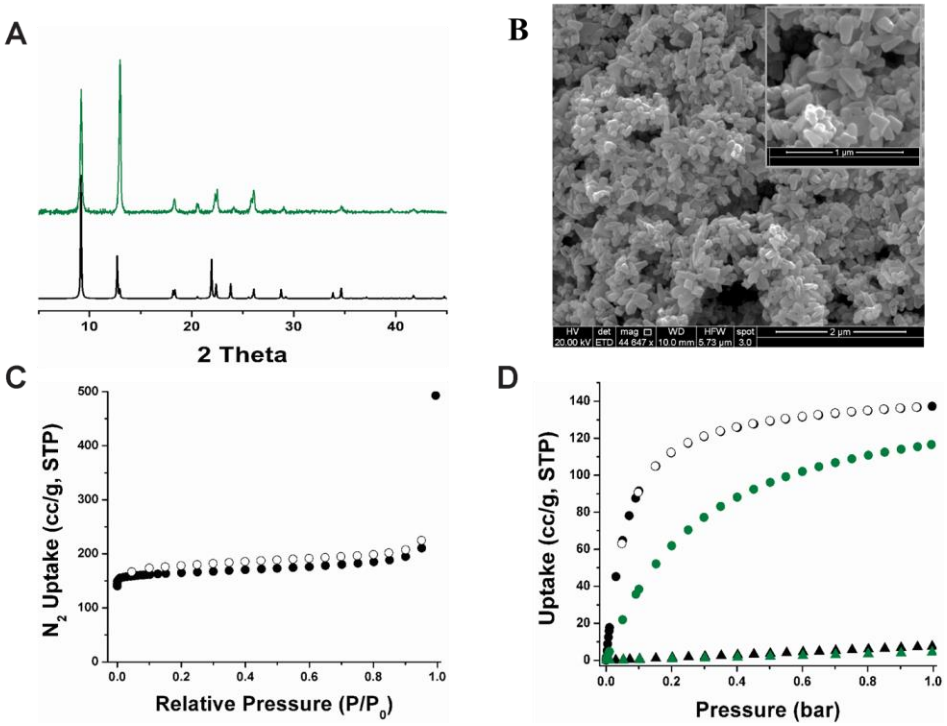

Figure 4.3 (A) PXRD (black, simulated; green, as-synthesized), (B) SEM, (C) N_2 adsorption isotherms (77 K) and (D) CO_2 (circles) and N_2 (triangles) adsorption isotherms at 273 K (black) and 298 K (green) of SIFSIX-Cu-2i.

4.2.2 Polyphosphazene Mixed Matrix Membrane Film Characterization

The fluoroalkoxy single-substituent polyphosphazene (TFE) was selected as a control material for the fabrication of MMMs (Figure 4.4). TFE polyphosphazene was used because it showed good gas separation performance, good film forming properties, and its rubbery nature may improve the interface between the polymer and filler particles.

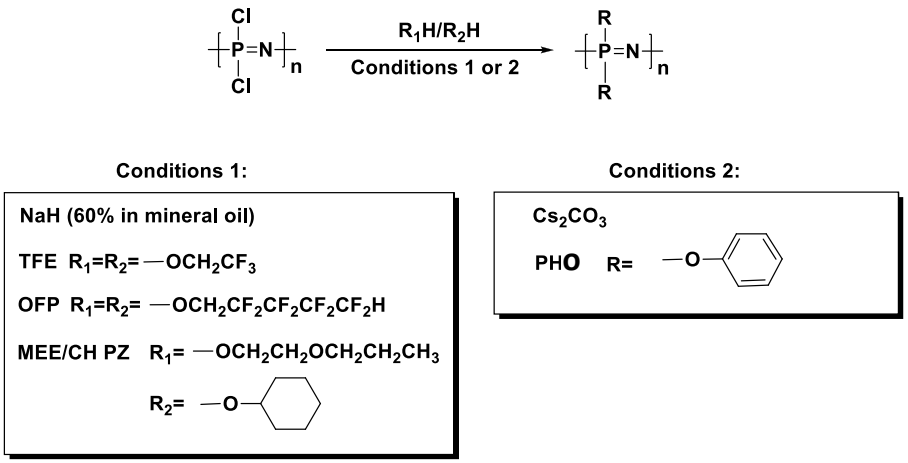

Figure 4.4 Macromolecular substitutions of polyphosphazenes.

SIFSIX–Cu-2i was selected as the filler particle material because of its strong, favorable interaction with CO_2, and chemical stability. Furthermore, it was anticipated that fluorinated groups in the SIFSIX-Cu-2i and TFE should interact well and form mixed matrix membrane without interfacial voids. This is the first report of using SIFSIX–Cu-2i in the fabrication and testing of MMMs using TFE-PZ as the polymer. Flat sheet dense MMMs containing poly(bis(trifluoroethoxy)phosphazene and different weight loadings (10 wt%, 15 wt% and 20 wt%) of MOF were fabricated.

SIFSIX-Cu-2i MOFs were heated isothermally at 100 °C for 30 minutes under flowing N_2 gas to remove any remaining solvent molecules before the TGA analysis. The maximum weight loss of SIFSIX-Cu-2i was at around 300 °C as shown in Figure 4.3, which was attributed to the decomposition of the organic 1,4-bis(4-pyridyl) butadiyne ligand. The neat TFE and TFE/SIFSIX-Cu-2i MMM films were also studied using TGA to determine the effect of the MOF particles on the thermal stability of the membranes (Figure 4.5). The thermal decomposition of neat TFE begins above 300 °C. Overall, thermogravimetric analyses of the MMMs showed minimal weight loss up to 200 °C indicating that the casting solvent was not trapped in the pores of the MOF. The decomposition temperature of the MMM decreased with

increased MOF loading. In some cases, the decomposition temperature of a MMM increases with an increase in the MOF loading because the interaction between the polymer and filler particle restricts the thermal motion of the polymer. This restricted motion increases the energy needed for the movement and segmentation of polymer chains, which enhances the thermal stability of the membranes.[111] The results presented here show the opposite trend because the decomposition temperature of the MOF is substantially lower (by more than 100 °C) than that of the TFE. The decomposition of the MOFs in the MMMs begins at ~200 °C, much earlier than TFE. Similar trends were reported for UiO-66-NH_2 in our previous report and $Cu_3(BTC)_2$ MOF based MMMs.[95]

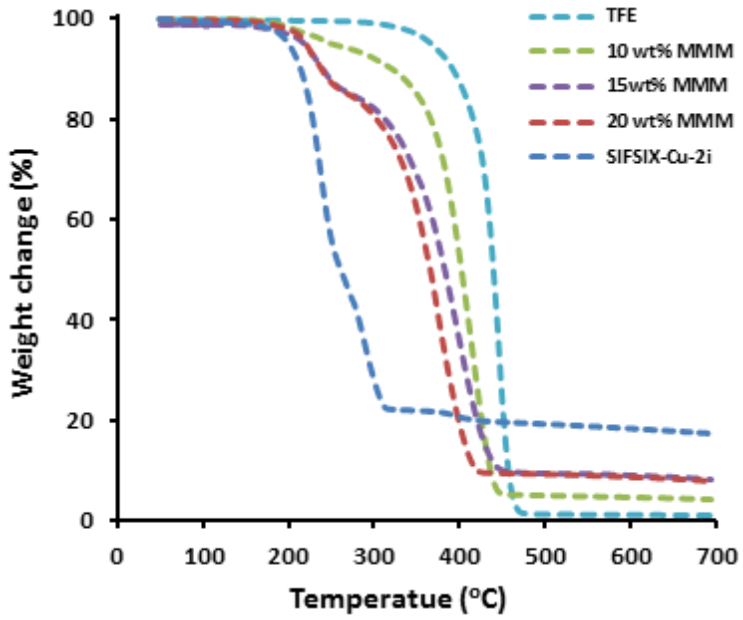

Figure 4.5 TGA analysis of polyphosphazene polymer and SIFSIX-Cu-2i based mixed matrix membranes

SEM was used to study the membrane cross-section morphology as well as the particle-polymer interface. Our previous studies and other studies in the literature confirmed that the interaction between the MOF and polymer is critical to obtain excellent separation performance.[90] Figure 4.6A shows a cross-section image of a neat TFE membrane. The texture is

smooth without any noticeable defects, which is characteristic of a dense polyphosphazene membrane. Representative cross sectional images of the MMMs with 10, 15 and 20 wt% of MOF are shown in Figures 4.6B-D. From the images, no obvious defects around the MOF particles were observed. In the case of 10wt% MMM, some defects were observed across the cross section. These defects might be artifacts that formed during freeze fracturing of the membranes due to breaking of small aggregates of particles. The CO_2/N_2 selectivity was used to test if these findings are artifacts or defects. Overall, the selectivity improved (Table 4.1), confirming that these defects are artifacts and through defects across the membrane. In all the cases SIFSIX-Cu-2i particles were typically well-dispersed without any obvious aggregated clusters of MOF particles.

There was not any observed scalloped morphology in the SEM micrographs with these TFE polyphosphazene, which are usually observed with glassy polymers. With Matrimid® MMMs, for example, scallop morphology is usually observed and is an indication of a strong attachment of the particle and filler.[33, 42] The polymer chains which are attached to the particles have very high fracture toughness compared to the polymer chains away from the filler particles and will not stretch much while freeze fracturing the membranes. The absence of any observable sieve-in-a-cage morphology or cavity formation at each loading is an indication of good film formation and strong interaction between the TFE and MOF particles in all three MMM cases. More sophisticated techniques like nano-computed tomography scanning (nano-CT) or positron annihilation lifetime spectroscopy (PALS) are needed to detect if there are any nano-defects or rigidification of the polymer around the particle.[96, 112] The gas separation performance of these membranes further confirmed the formation of defect-free MMMs using TFE-PZ and SIFSIX-Cu-2i.

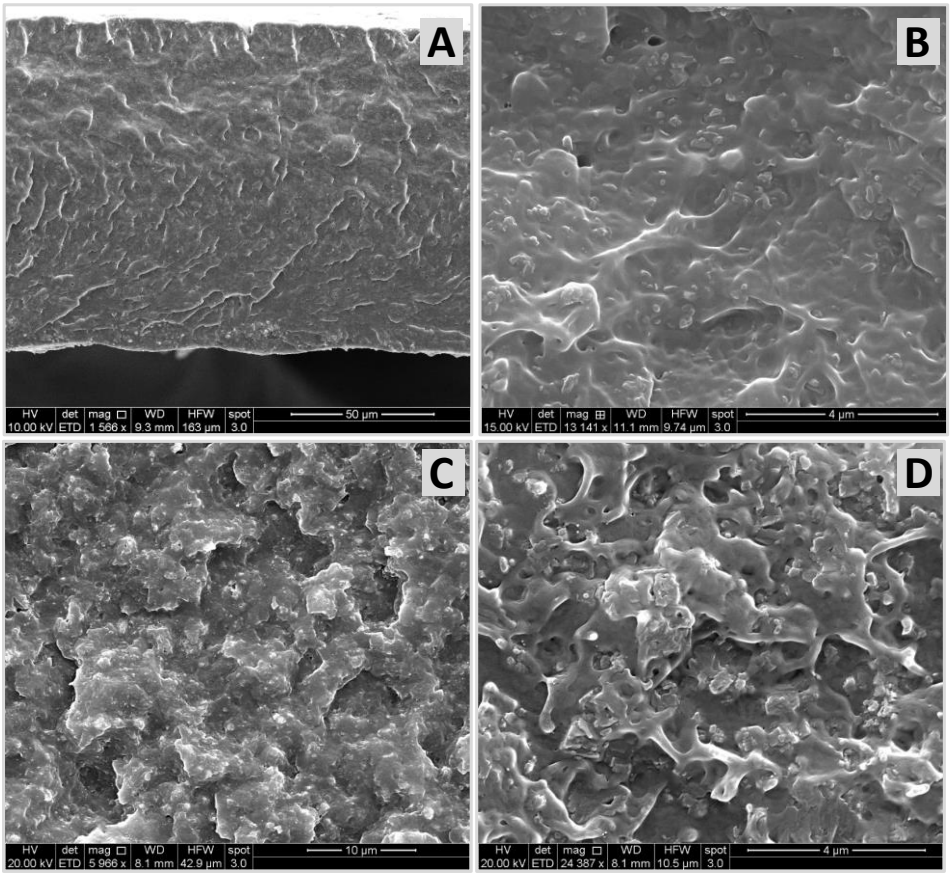

Figure 4.6 Cross sectional SEM images showing the defect-free dense mixed matrix membranes containing (A) 0 wt% MOF-TFE, (B) 10 wt% MOF-TFE, (C) 15 wt% MOF-TFE, and (D) 20 wt% MOF-TFE.

Table 4.1 Gas separation properties of the TFE- SIFSIX-Cu-2i mixed matrix membranes.

%wt loading of MOF	CO_2 Permeability (Barrer)	N_2 Permeability (Barrer)	CO_2/N_2 ideal selectivity
TFE	325	24.6	13.2
10 wt%	354	22.0	16.1
15 wt%	387	19.6	19.7
20 wt%	441	23.5	18.8

MMMs with 10, 15, and 20 wt% of SIFSIXCu-2i in TFE polyphosphazene were fabricated. CO_2 permeability and pure gas selectivity of the three MMMs and the neat polymer are shown in Table 4.1. These membranes showed improved gas separation properties compared to the neat polymer membranes at all the three loading conditions. Both the CO_2 permeability and CO_2/N_2 selectivity were improved with increased particle loading. These results indicate that

the filler particles in the MMM were well dispersed and defect free as confirmed by SEM images (Figure 4.6). This was likely due to the interaction between the MOF containing free fluorine groups and the pendent fluorine groups on the polymer backbone. The increase in the CO_2 permeability with the addition of SIFSIX-Cu-2i particle can related to two factors: 1) the path length of CO_2 diffusion might be decreased by the addition of SIFSIX-Cu-2i particles since the CO_2 (kinetic diameter 0.33 nm) passes through the pores of SIFSIX-Cu-2i (pore size 0.6 nm) without any resistance and 2) the increase in the free volume of the polymer due to chain packing disruption. The increase in CO_2/N_2 selectivity was attributed to the higher affinity of SIFSIX-Cu-2i filler towards CO_2 compared to N_2 as confirmed by adsorption studies. The adsorption of CO_2 molecules in the pores of SIFSIX-Cu-2i might be further restricting the passage of N_2 through its pores, resulting in the increased diffusion path length since it needs to pass around the particles, which increases tortuosity. CO_2 transport through the membranes dominates in both the case of diffusivity and solubility.

In some of the reported MMM studies, adding filler particles causes the permeability to increase at the expense of gas selectivity or vice versa.[44] Here, the MMMs exhibited improved CO_2 permeability as compared to the neat polymer while significantly improving the selectivity with MOF loadings between 10-20 wt%. This highlights the importance of selecting filler particles that chemically and physically interact with the polymer while possessing high CO_2 adsorption capacity. The gas separation performance of these membranes were compared with other polymeric membranes on the Robeson upper bound (Figure 4.7). These membranes out performed many other polymers and close to the upper bound line. These membranes have high potential for the separation of CO_2 from fossil fuel derived flue gas. Further optimization of

material properties is needed to get performance above the upper bound, and further reduction of the film thickness is necessary to achieve high gas permeance values.

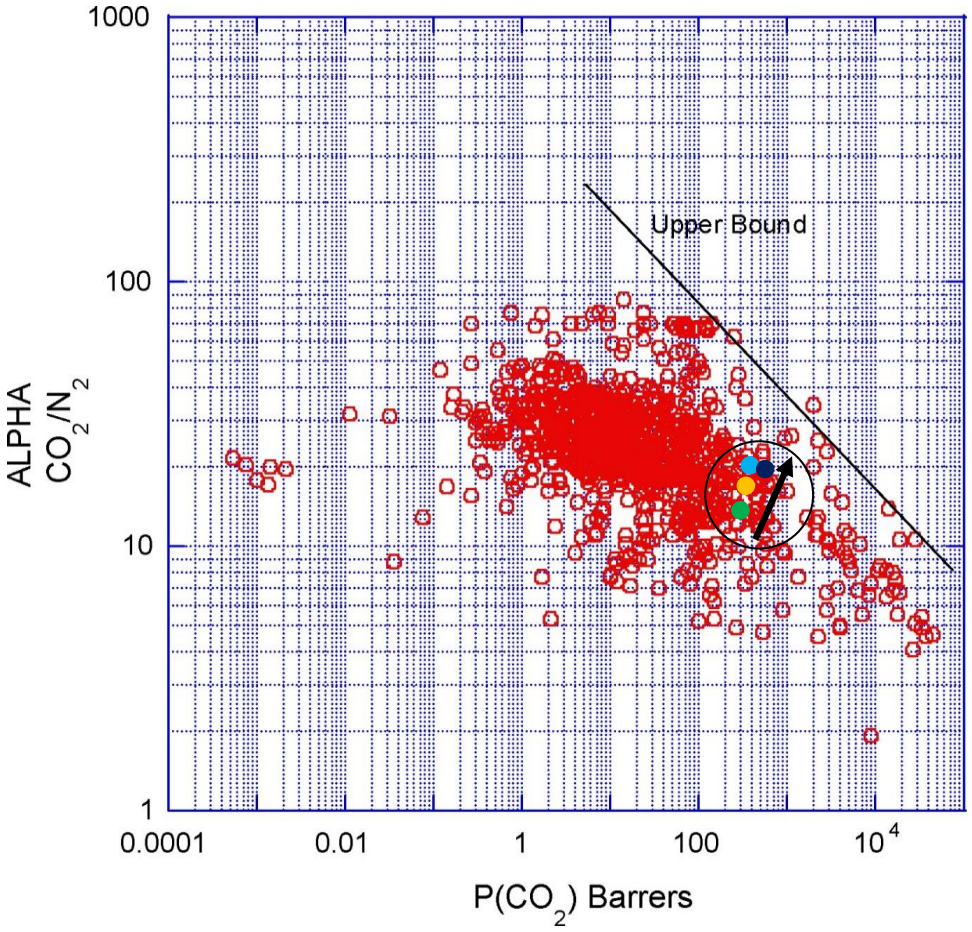

Figure 4.7 Comparison of the performance of the TFE polyphosphaze (●), 10 wt% MMM (●), 15wt% MMM (●), and 20 wt% MMM (●) with other polymer membranes.

4.3 Conclusion

In this study, we have expanded upon our previous work. The selection of a MOF (SIFSIX-Cu-2i) that selectively adsorbs CO_2 over N_2 and H_2O is an improvement over the hydroscopic UiO-66-NH_2. Furthermore, the polyphosphazene polymers are more flexible, tunable, and have better stability in various thermal and chemical conditions compared to Matrimid® in the previous study. We have shown that MMMs of these materials have more "real world" possibility in post-combustion CO_2 capture. Furthermore, the selection of SIFSIX-

Cu-2i with the polyphosphazene polymer was intentional in order to eliminate polymer/particle defects of the MMM. The MMMs synthesized approach the Robeson Upper bound and we are encouraged that these materials can continue to improve and expand their possibilities as CO_2 scrubbers.

4.4 Experimental Section

4.4.1 Synthesis of Polyphosphazenes

4.4.1.1 Synthesis of Poly[bis(trifluoroethoxy)phosphazene] (TFE)

Poly(dichlorophosphazene) (15.00 g, 129.46 mmol) was dissolved in anhydrous THF (1 L). Meanwhile, trifluoroethanol ($HOCH_2CF_3$) (20.50 mL, 284.8 mmol) and sodium hydride (NaH) (11.39 g, 294.8 mmol, 60% in mineral oil) were stirred in anhydrous THF (500 mL) in a separate Schlenk flask at room temperature for 4 h. This mixture was then added to the polymer solution and was allowed to react at room temperature for 1 day. The reaction medium was concentrated to 1/3 in volume and precipitated from THF into water (× 3) and from THF to hexanes (× 3). The collected product was dried under vacuum as a white fibrous material (yield=80%). ^{1}H NMR (acetone-d_6) δ (ppm): 4.58 (s, $–OCH_2CF_3$, 2H). ^{19}F NMR (acetone-d_6) δ (ppm): -75.79 (s, $–OCH_2CF_3$). ^{31}P NMR (acetone-d_6) δ (ppm): -7.81 (s).

4.4.1.2 Synthesis of SIFSIX-Cu-2i MOF

The synthesis of SIFSIX-Cu-2i was scaled up from a reported procedure. Stock solutions of $CuSiF_6$ (0.258 M) in water and 4,4'-dipyridylacetylene (dpa, 0.270 M) in methanol were prepared. To a 40 mL vial were added 15 mL of $CuSiF_6$ (3.87 mmol), 15 mL of dpa (4.05 mmol). The vial was capped and heated in an 85 °C oven for 12 hours. Purple microcrystalline product was centrifuged (5 min, ~1000 rpm) and washed first with methanol (x 2) and then with

water (x 2). The product was then dried in a 100°C oven for 24 h. The collected sample was stored in a capped vial and used without further purification.

4.4.2 Membrane Fabrication

For preparation of the neat polyphosphazene dense membrane, the polyphosphazene was dissolved in THF followed by mixing on a roller mixer. Then, the solution was kept stationary overnight to remove any retained gas bubbles. Prior to casting, a glove bag was purged with N_2 to remove any humidity and was saturated with THF to slow down the rate of solvent evaporation from the membrane. Polyphosphazene dense membranes were cast onto a glass plate in a glove bag using a casting knife. The resulting membrane was kept for a day in the glove bag as the THF evaporated slowly from the polymer. The membrane was dried at 100°C for 18 hours and slowly cooled to room temperature.

For preparation of the MMMs, the solution was prepared using the 'priming' technique in which the SIFSIX particles were first dispersed in THF solvent using an ultrasonic probe (Branson Digital Sonifier 450 model) to obtain a homogenous dispersion. Next, the MOF crystals were primed by adding 30% of the total polyphosphazene to the SIFSIX/THF solution followed by roller mixing. The remaining polyphosphazene polymer was added in two steps (30% and 40%) followed by stirring after each addition. The mixed matrix dense films were formed by casting the membranes similar to the procedure discussed above for the neat polyphosphazene membranes. The MOF loading was controlled by changing the mass ratio of MOF to polyphosphazene in the mixed matrix dope solution according to Equation 4.1.

$$\text{Filler Loading (wt\%)} = \frac{W_{filler}}{W_{filler} + W_{polymer}} \times 100\% \qquad (4.1)$$

4.4.3 Materials and Membrane Characterization

4.4.3.1 Structural Characterization

^{1}H and ^{31}P spectra were recorded on a Bruker WM-360 NMR spectrometer operated at 360 or 145 MHz, respectively. ^{1}H NMR spectra were referenced to solvent signals, while ^{31}P NMR chemical shifts are relative to 85% phosphoric acid as an external reference, with positive shift values downfield from the reference. ^{19}F NMR spectra were collected using a Bruker CDPX-300 spectrometer operated at 282 MHz with trifluoroacetic acid as an internal standard.

4.4.3.2 Thermal Analysis

Thermal characteristics of samples were measured with a TA Instruments Q10 differential scanning calorimeter and a Perkin-Elmer thermogravimetric analyzer. About 10 mg of dried sample was used for each test. A heating rate of 10 °C/min with a temperature range from -100 to 200 °C was used for the DSC, while a heating rate of 20 °C/min from 25 to 800 °C was applied for TGA measurements. Both instruments used dry nitrogen as the purge gas. Thermogravimetric analysis (TGA) of each MOF sample was performed using a TGA Q500 thermal analysis system. All TGA experiments of MOF samples were performed under a N_2 atmosphere from 25-600°C at a rate of 2 °C /min. TGA was also used to determine the thermal stability of the MMMs and to analyze any remaining solvent in the membranes.

4.4.3.3 Microscopy

Scanning electron microscopy (SEM) was performed on an FEI Quanta 600 scanning electron microscope to determine the particle size of the MOF crystallites, as well as to evaluate the cross-sectional structure of the fabricated membranes. The membrane samples were prepared by fracturing the membranes in liquid nitrogen and subsequent sputter coating of palladium using a SPI Module Sputter Coater.

4.4.3.4 MOF Structure

Powder X-Ray diffraction (PXRD) was used to verify the phase purity and homogeneity of the MOF samples. Each pattern was collected using a Bruker AXS D8 Discover powder diffractometer at 40 kV, 40 mA for Cu Kα, (λ = 1.5406 Å) with a scan speed of 0.10 sec/step and a step size of 0.02018°. The simulated powder pattern was calculated using Mercury 3.5.1 software.

4.4.3.5 Gas Adsorption

Gas adsorption isotherms were collected volumetrically as a function of relative pressure using an Autosorb 1 from Quantachrome. Activated MOF samples were weighed using an AB54-S/FACT (Mettler Toledo) electrogravimetric balance (sensitivity 0.1 mg). 9 mm large bulb cells (from Quantachrome) of a known weight were loaded with ~120 mg of sample for gas adsorption experiments. The samples were degassed at room temperature for 24 hours on the degassing station until the outgas rate was no more than 3.0 mTorr/min. The degassed sample and sample cell were weighed precisely and then transferred back to the analyzer. The temperature of each sample for N_2 adsorption experiments was controlled using a refrigerated bath of liquid nitrogen (77 K). CO_2 and N_2 isotherms (273 K and 298 K) were measured in a temperature-controlled water bath. The N_2 and CO_2 adsorbates were of UHP grade.

4.4.3.6 Gas Separation Performance

Pure gas CO_2 and N_2 permeation tests were performed at room temperature using an isochoric (constant volume, variable pressure) permeation system, which consists of two chambers separated by the membrane material. The upstream chamber is pressurized with a pure gas while the downstream chamber is evacuated. The rate of pressure rise in the evacuated chamber is used to determine the gas permeability of the membrane. Upstream pressures were

measured with a pressure transducer (Maximum pressure 150 psia, Viatran Inc., Model-345). Downstream pressures were measured using a Baratron 627D capacitance manometer with a maximum pressure output of 10 Torr (MKS, Wilmington, MA).

Testing was carried out as follows: the membrane was loaded into a Millipore high pressure 25 mm filter holder. The entire permeation system was de-gassed using a vacuum pump (Edwards nXDS 10i scroll pump) for 18 hours and then the leak rate was measured by isolating the permeation system from the vacuum pump. The leak rate was always much less than the typical steady state pressure rise during gas permeation measurement. The feed gas was then introduced to the upstream side of the membrane, and the pressure rise in the downstream volume was recorded as a function of time. All the membranes were tested at 22.5 psig upstream pressure and room temperature. The thicknesses of the membranes were measured using a micrometer several times and the average values were used for the calculation of permeability. All permeation data were determined at room temperature using a minimum of two samples to ensure the reproducibility of the experimental results.

The permeation of a gas through the membrane can be described using the solution-diffusion model. The permeability of a gas, i, is given by: $P_i = D_i \bullet S_i$, where D_i and S_i represent the diffusion and solubility coefficients of component i, respectively. In terms of this model, the productivity of a membrane is defined by the permeability of the gas through the membrane and the ideal selectivity of the membrane is the ratio of the permeabilities of the individual gases. Permeability was calculated by differentiating the pressure rise as a function of time and using equation 4.2

$$P = \frac{V_d l}{p_2 ART}\left[\left(\frac{dp_1}{dt}\right)_{SS} - \left(\frac{dp_1}{dt}\right)_{leak}\right] \tag{4.2}$$

Where, V_d = downstream volume (cm^3), l = film thickness (cm), p_2 = upstream absolute pressure (cmHg), A = film area (cm^2), T = Temperature (K), R = gas constant (cm^3 cmHg/mol K), $(dp_1/dt)_{ss}$ = rate of downstream pressure rise during membrane testing (cmHg/sec), $(dp_1/dt)_{leak}$ = rate of downstream pressure rise under vacuum (cmHg/sec).

Appendix

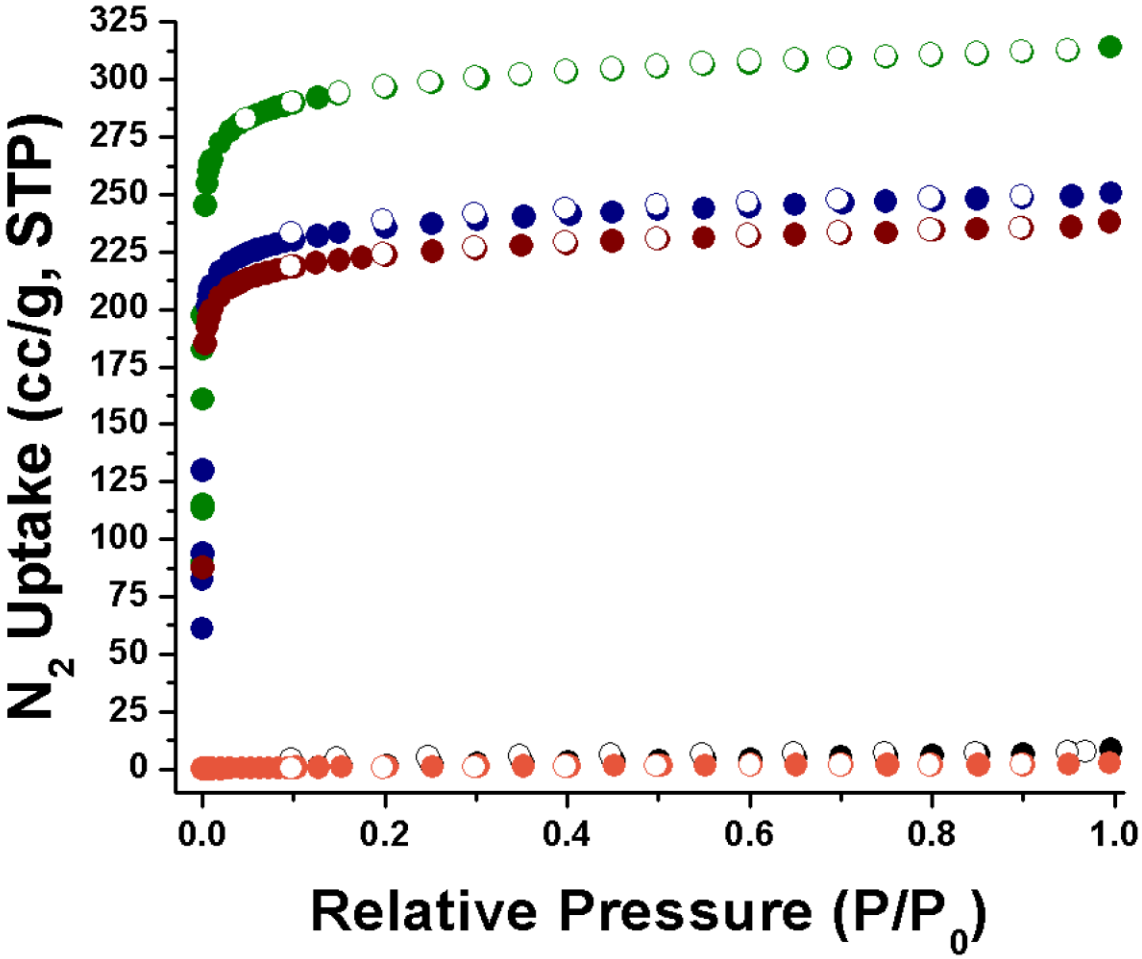

Figure A1 N_2 isotherm for **I** before exposure (green), after 90% humidity (black), 20% humidity (orange), 17.5% humidity (red), and 15% humidity (blue).

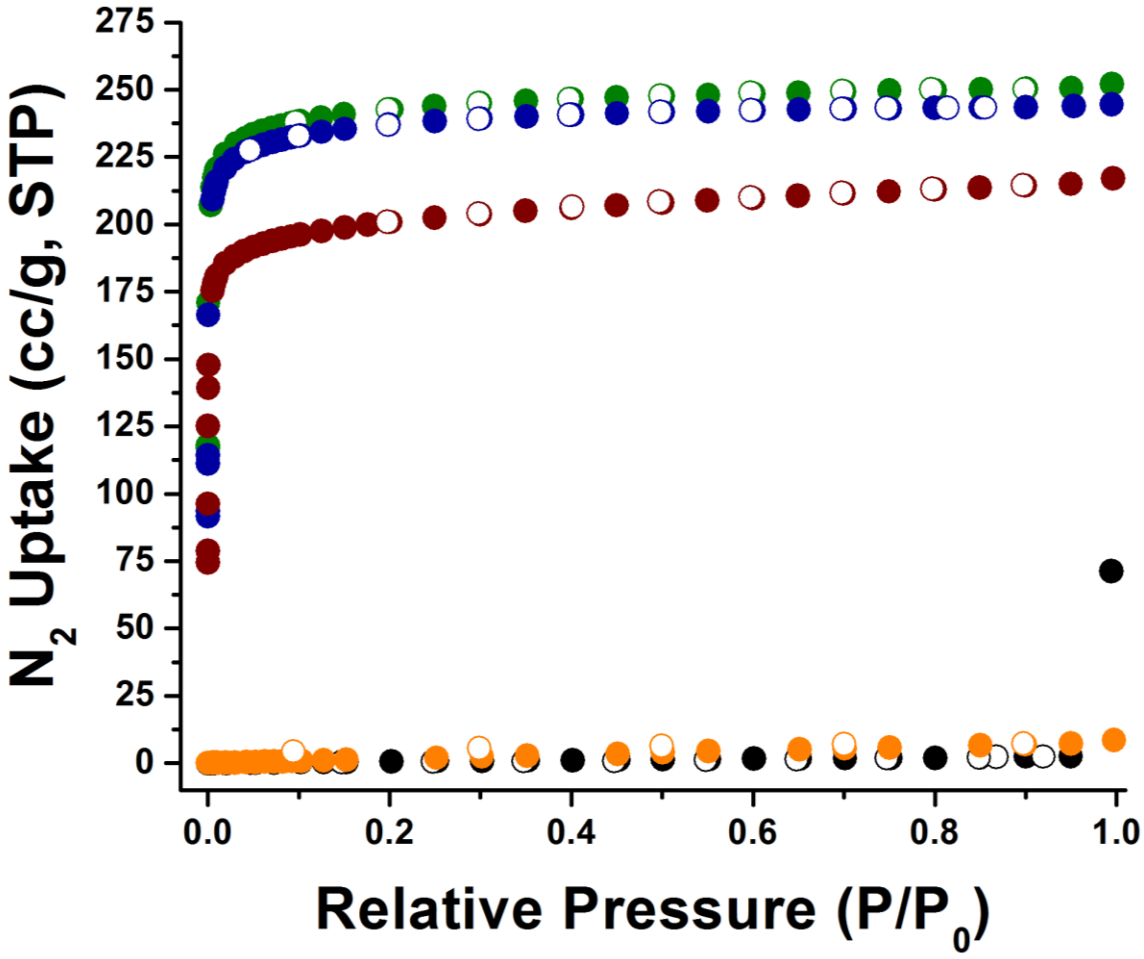

Figure A2 N_2 isotherm for **II** before exposure (green), after 90% humidity (black), 20% humidity (orange), 17.5% humidity (red), and 15% humidity (blue). Some points omitted for clarity due to overlapping plots.

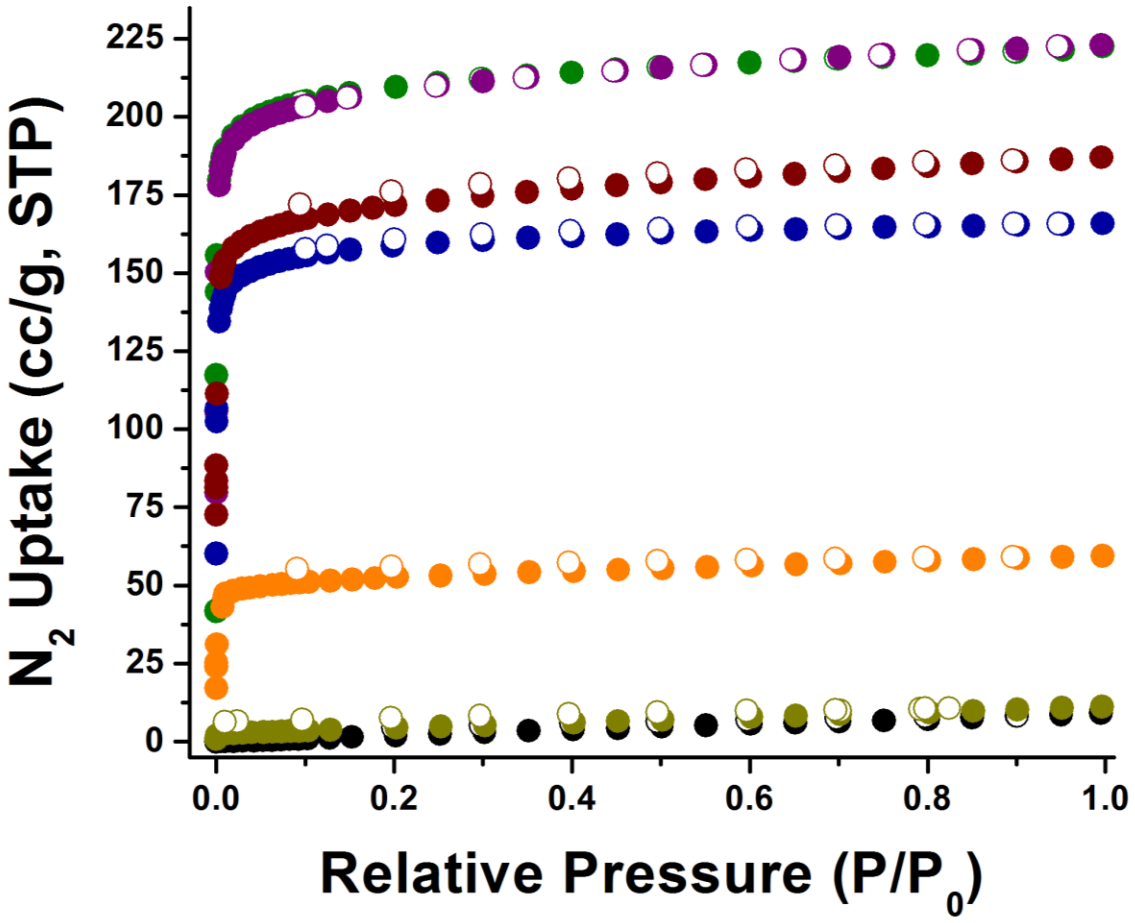

Figure A3 N_2 isotherm for **III** before exposure (green), after 90% humidity (black), 22% humidity (yellow), 20% humidity (orange), 17.5% humidity (red),15% humidity (blue), 12.5% humidity (purple). Some points omitted for clarity due to overlapping plots.

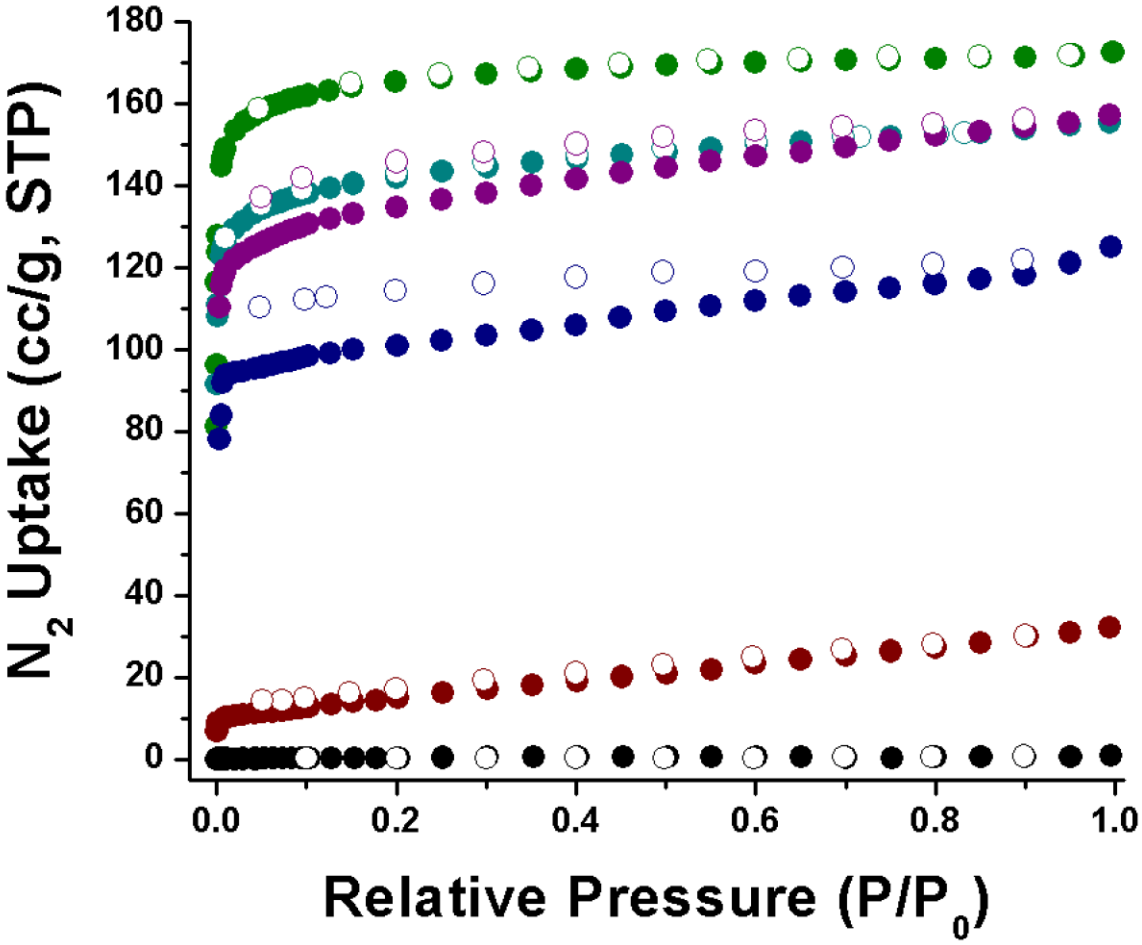

Figure A4 N_2 isotherm for **IV** before exposure (green), after 90% humidity (black), 17.5% humidity (red), 15% humidity (blue), 12.5% humidity (purple), and 10% humidity (teal).

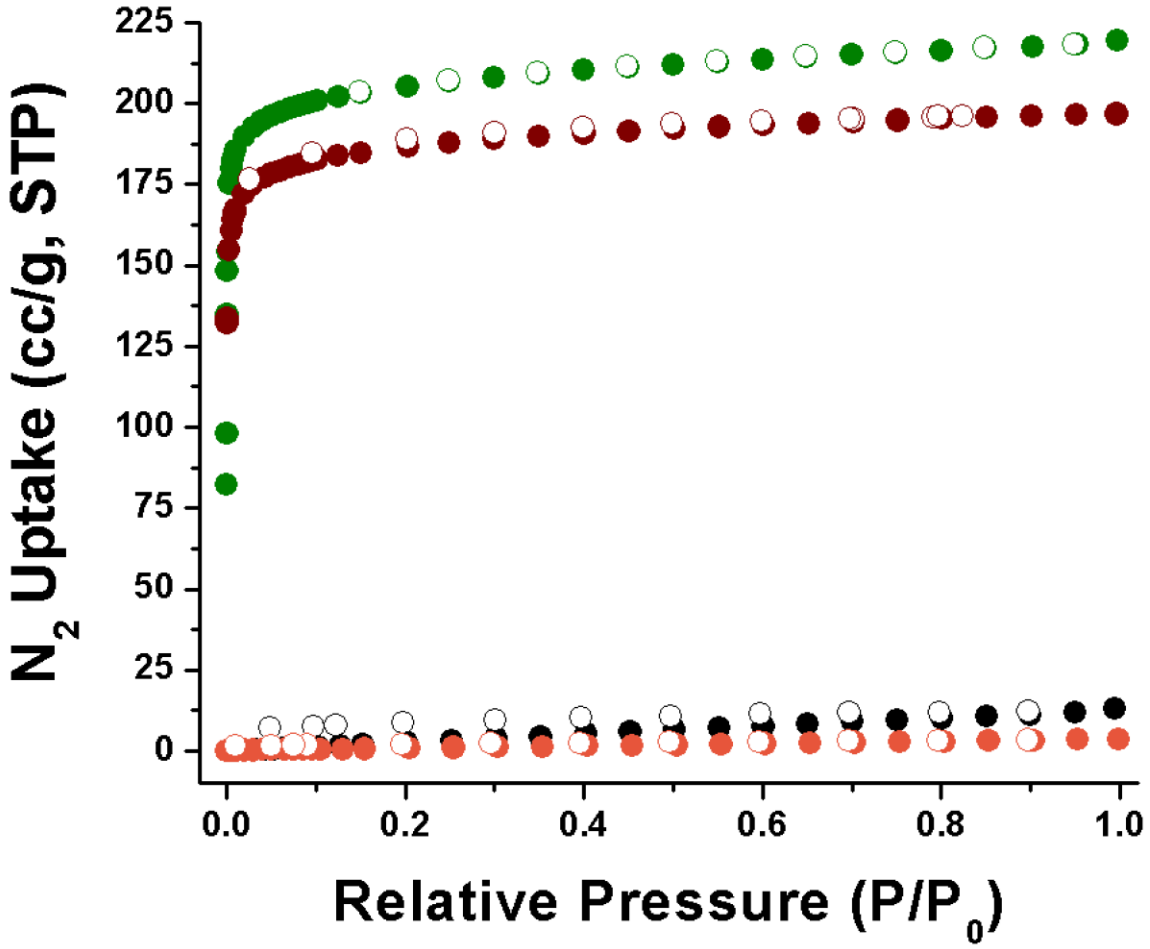

Figure A5 N_2 isotherm for **V** before exposure (green), after 90% humidity (black), 5% humidity (red), and 7.5% humidity (orange).

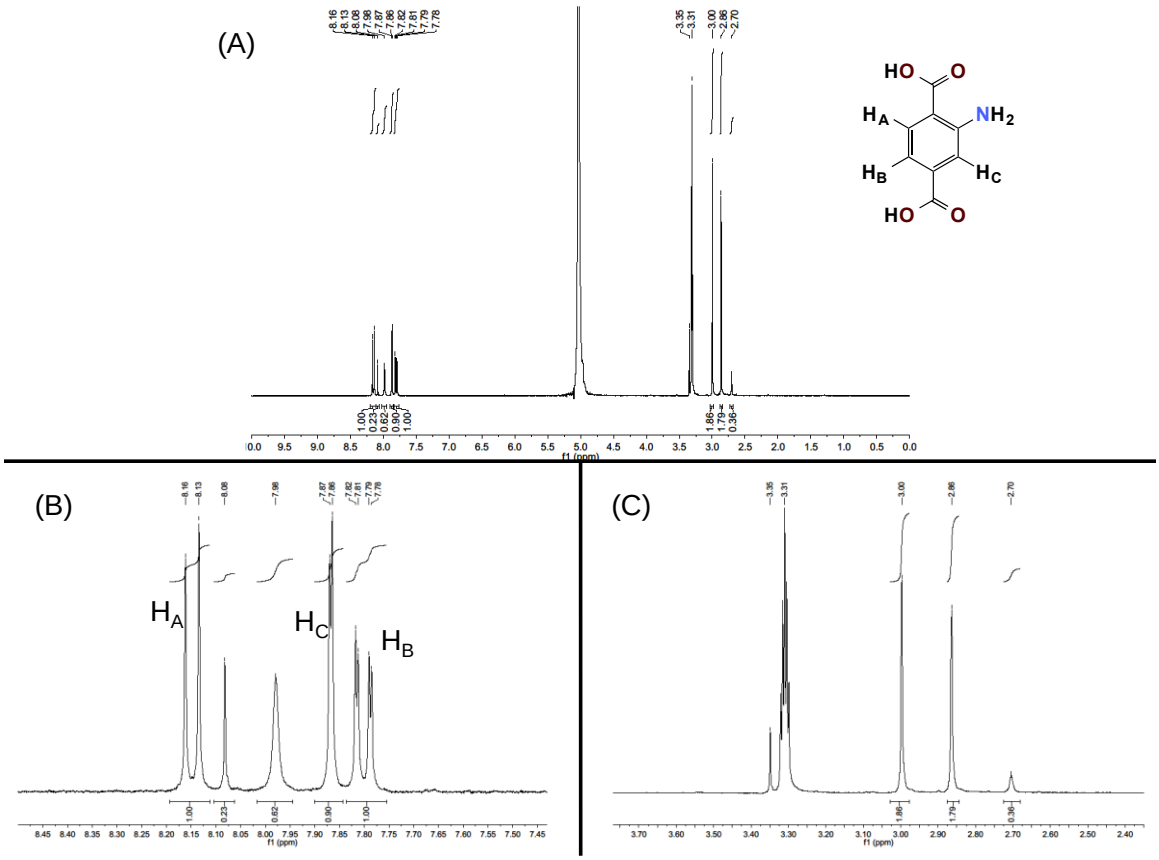

Figure A6 ^{1}H NMR spectrum of digested **I** (A) and a magnified region (B & C). See **Table A1** for signal shifts, integrations, and assignments.

Table A1 ^{1}H NMR signal shifts, integration and assignments for **I**.

Proton	Chemical Shift, ppm (splitting)	Predicted Integration	Actual Integration
H_A	8.14 (doublet)	1 H	1.00 H
H_B	7.80 (doublet)	1 H	1.00 H
H_C	7.86 (singlet)	1 H	0.90 H
DMF	7.98 (singlet)	--	0.62 H
DMF	2.86 and 3.00 (singlets)	--	1.83 H
$CHCl_3$	8.08 (singlet)	--	0.23 H
H_2O & HF	5.00 (singlet)	--	--
MeOH	3.31 (singlet)	--	--

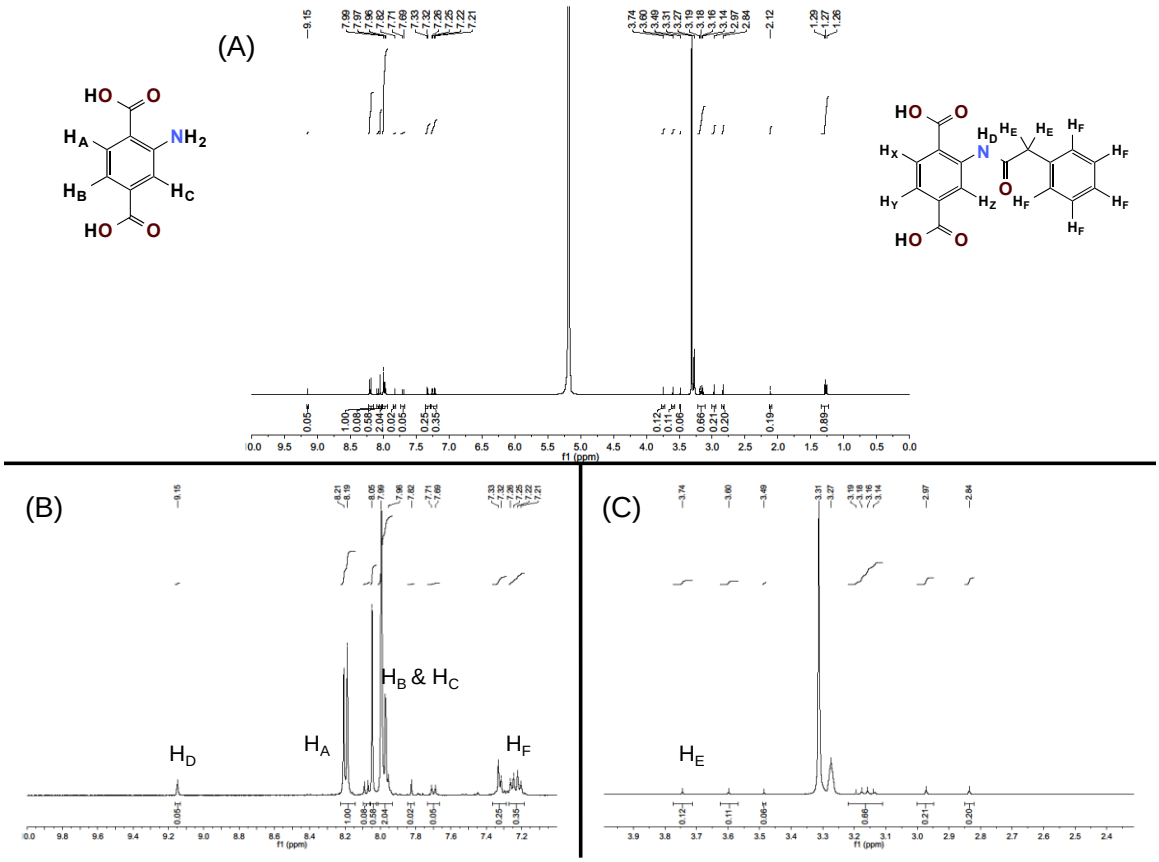

Figure A7 ^{1}H NMR spectrum of digested $\mathbf{I_{PA}}$. Degree of functionalization determined by calculating the integration ratio between H_2-NH_2-BDC (H_A) to amide proton (H_D). $\mathbf{I_{PA}}$ was functionalized 5% in this sample and functionalization ranged from 3-6%. Some free phenylacetyl chloride is observed (H_E and H_F). See **Table A2** for signal shifts, integrations, and assignments.

Table A2 ^{1}H NMR signal shifts, integration and assignments for $\mathbf{I_{PA}}$.

Proton	Chemical Shift, ppm (splitting)	Predicted Integration	Actual Integration	Percent Functionalization
H_A	8.20 (doublet)	1 H	1.00 H	--
H_B & H_C	7.97 (multiplet)	2 H	2.04 H	--
H_D	9.15 (singlet)	--	0.05 H	5%
H_E	3.74 (singlet)	--	0.12 H	--
H_E (Free)	3.60 (singlet)	--	0.11 H	--
H_F	7.32 (multiplet)	--	0.25 H	--
H_F (Free)	7.23 (multiplet)	--	0.35 H	--
H_X	8.07 (doublet)	--	0.08 H	--
H_Y	7.70 (doublet)	--	0.05 H	--
H_Z	7.82 (singlet)	--	0.02 H	--
DMF	2.84 & 2.97 (singlets)	--	0.20 H	--
DMF/$CHCl_3$	8.05 (singlet)	--	0.58 H	--
H_2O & HF	5.00 (singlet)	--	--	--
MeOH	3.31 (singlet)	--	--	--

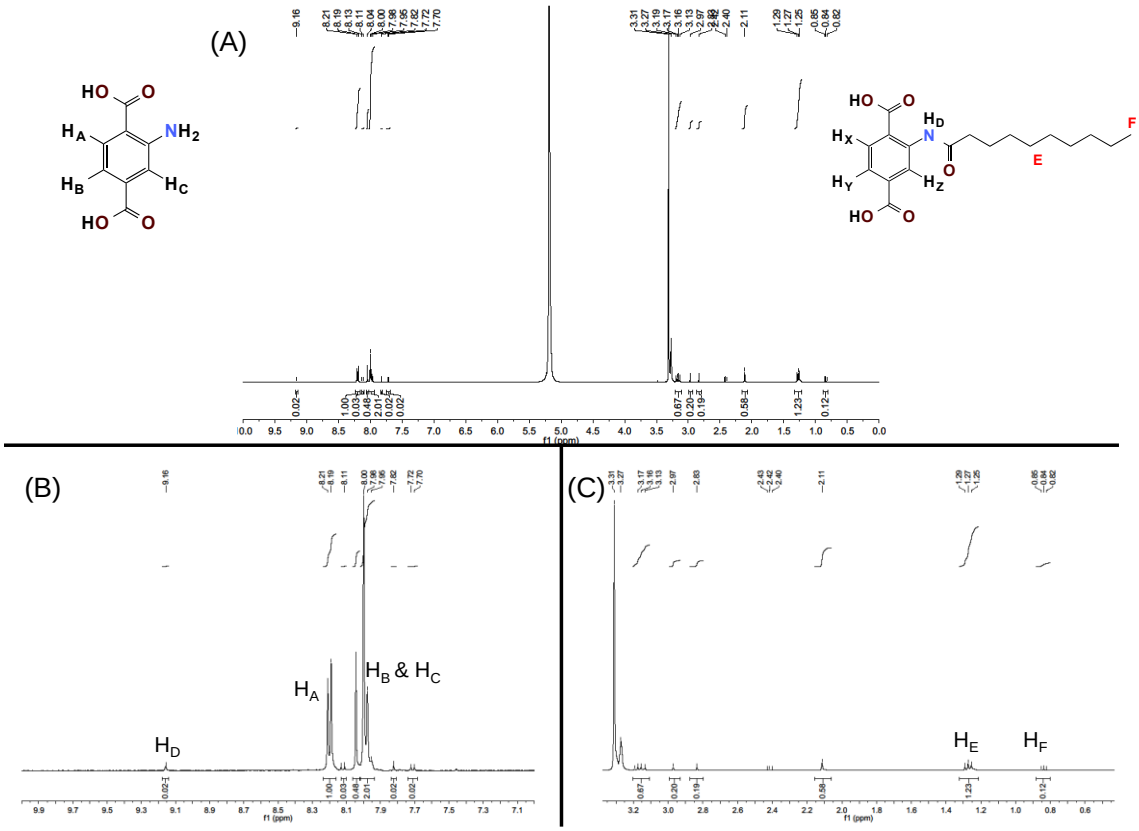

Figure A8 ^{1}H NMR spectrum of digested $\mathbf{I_{C10}}$. Degree of functionalization determined by calculating the integration ratio between H_2-NH_2-BDC (H_A) to amide proton (H_D). $\mathbf{I_{C10}}$ was functionalized 2% in this sample and ranged from 2-5%. We observe higher than expected integrations for H_E and H_F, which we attribute to the presence of free decanoyl chloride. See **Table A3** for signal shifts, integrations, and assignments.

Table A3 ^{1}H NMR signal shifts, integration and assignments for $\mathbf{I_{C10}}$.

Proton	Chemical Shift, ppm (splitting)	Predicted Integration	Actual Integration	Percent Functionalization
H_A	8.20 (doublet)	1 H	1.00 H	--
H_B & H_C	7.98 (multiplet)	2 H	2.01 H	--
H_D	9.16 (singlet)	--	0.02 H	2%
H_E	1.27 (multiplet)	--	1.23 H	--
H_F	0.84 (triplet)	--	0.12 H	--
H_X	8.11 (doublet)	--	0.03 H	--
H_Y	7.71 (doublet)	--	0.02 H	--
H_Z	7.82 (singlet)	--	0.02 H	--
DMF	2.83 & 2.97 (singlets)	--	0.19 H	--
DMF/$CHCl_3$	8.05 (singlet)	--	0.48 H	--
H_2O & HF	5.00 (singlet)	--	--	--
MeOH	3.31 (singlet)	--	--	--

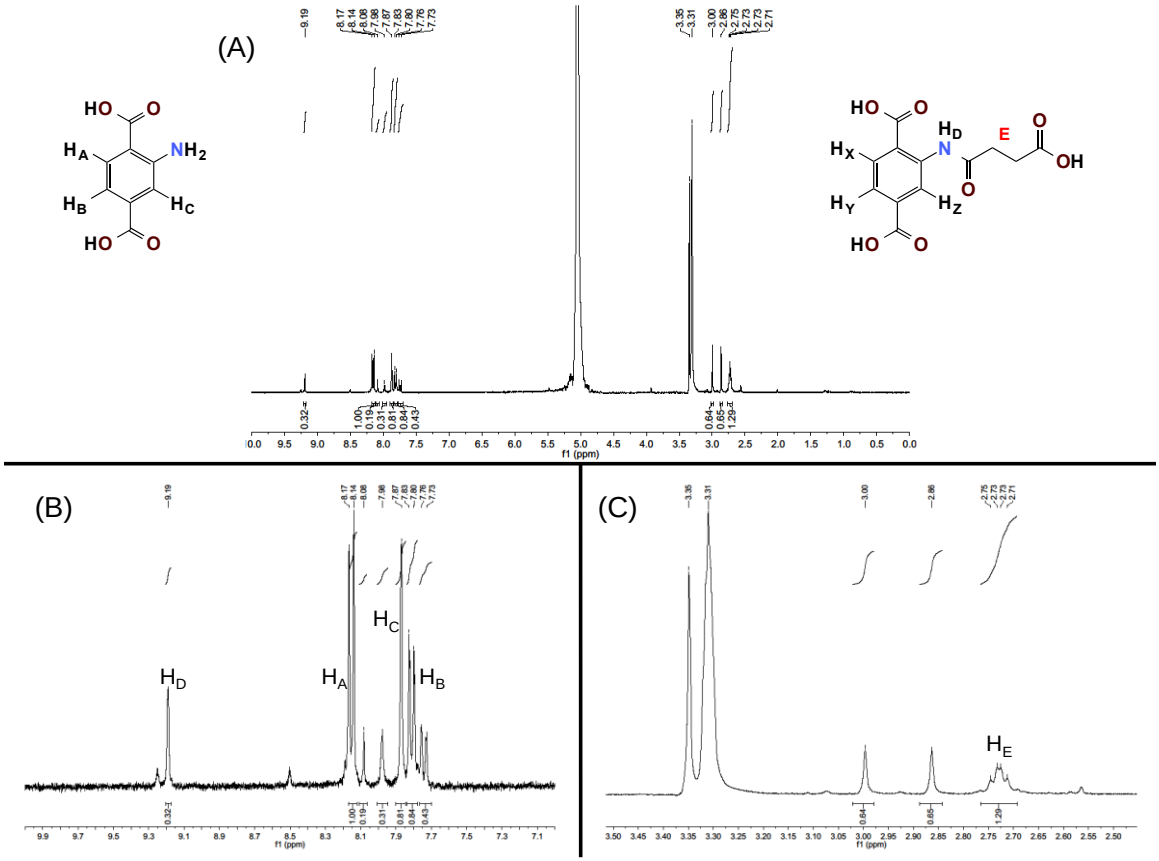

Figure A9 ^{1}H NMR spectrum of digested **I$_{SA}$**. Degree of functionalization determined by calculating the integration ratio between H_2-NH_2-BDC (H_A) to amide proton (H_D). **I$_{SA}$** was functionalized 32% in this sample and ranged from 16-32%. See **Table A4** for signal shifts, integrations, and assignments.

Table A4 ^{1}H NMR signal shifts, integration and assignments for $\mathbf{I_{SA}}$.

Proton	Chemical Shift, ppm (splitting)	Predicted Integration	Actual Integration	Percent Functionalization
H_A	8.16 (doublet)	1 H	1.00 H	--
H_B	7.78 (doublet)	1 H	0.84 H	--
H_C	7.87 (singlet)	1 H	0.81 H	--
H_D	9.19 (singlet)	--	0.32 H	32%
H_E	2.73 (multiplet)	--	1.29 H	--
H_Y	7.74 (doublet)	--	0.43 H	--
DMF	7.98 (singlet)	--	0.31 H	--
DMF	2.86 & 3.00 (singlets)	--	0.64 H	--
H_2O & HF	5.00 (singlet)	--	--	--
MeOH	3.31 (singlet)	--	--	--

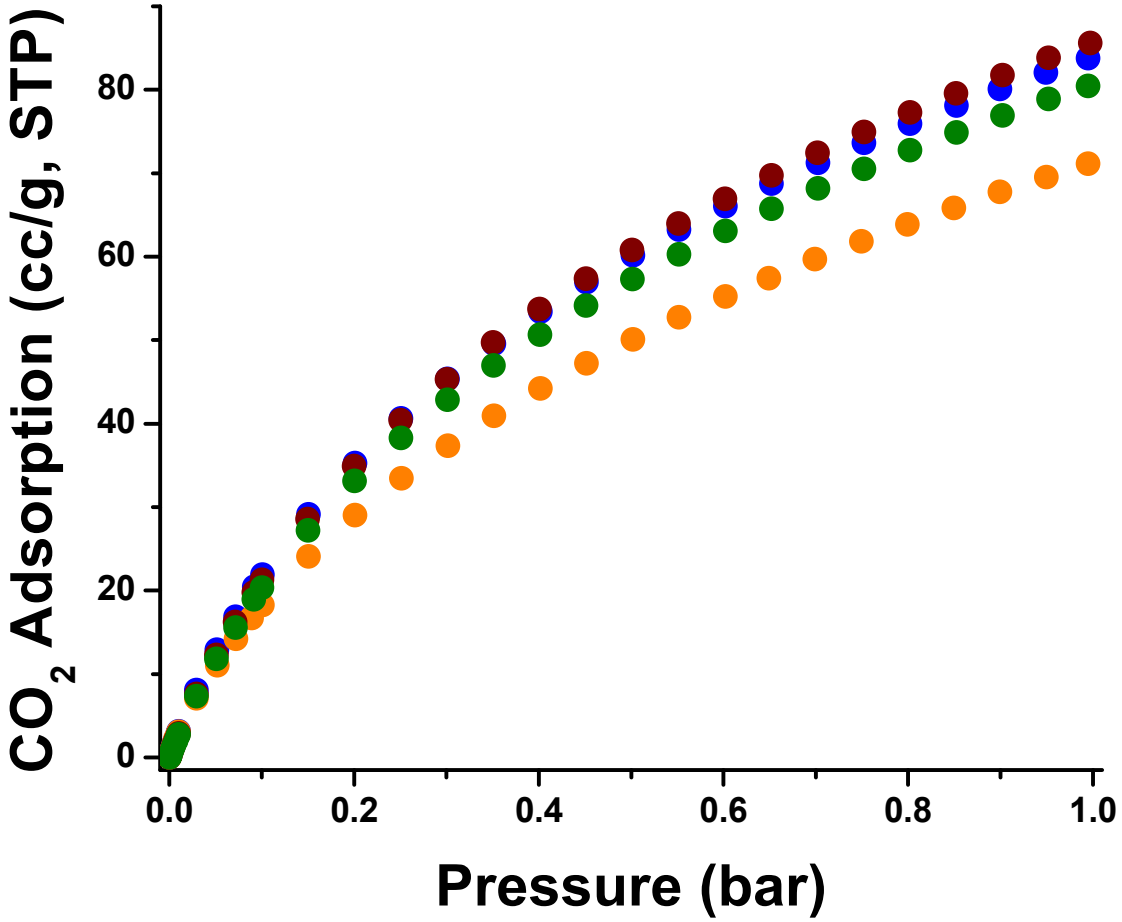

Figure A10 CO_2 isotherms (273 K) of **I** (blue), $\mathbf{I_{PA}}$ (green), $\mathbf{I_{C10}}$ (maroon), and $\mathbf{I_{SA}}$ (orange).

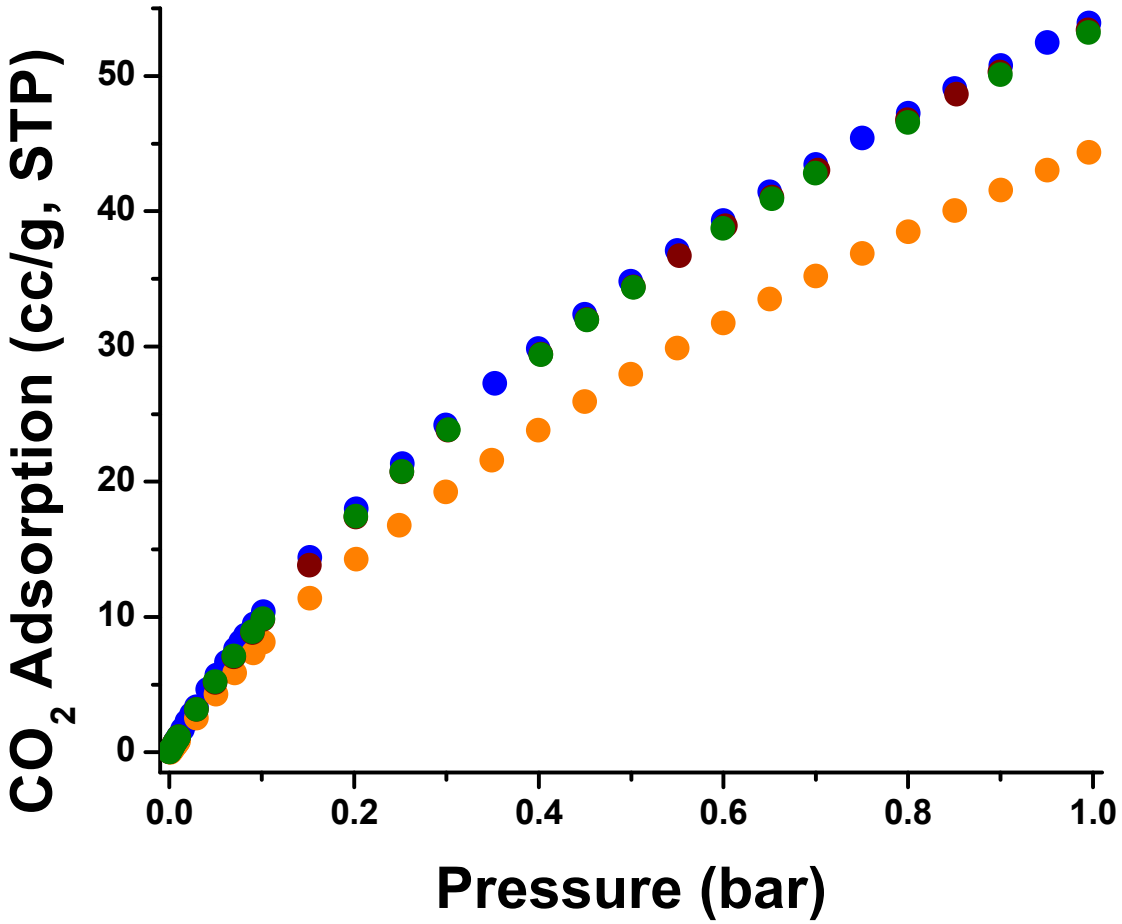

Figure A11 CO_2 isotherms (298 K) of **I** (blue), $\mathbf{I_{PA}}$ (green), $\mathbf{I_{C10}}$ (maroon), and $\mathbf{I_{SA}}$ (orange).

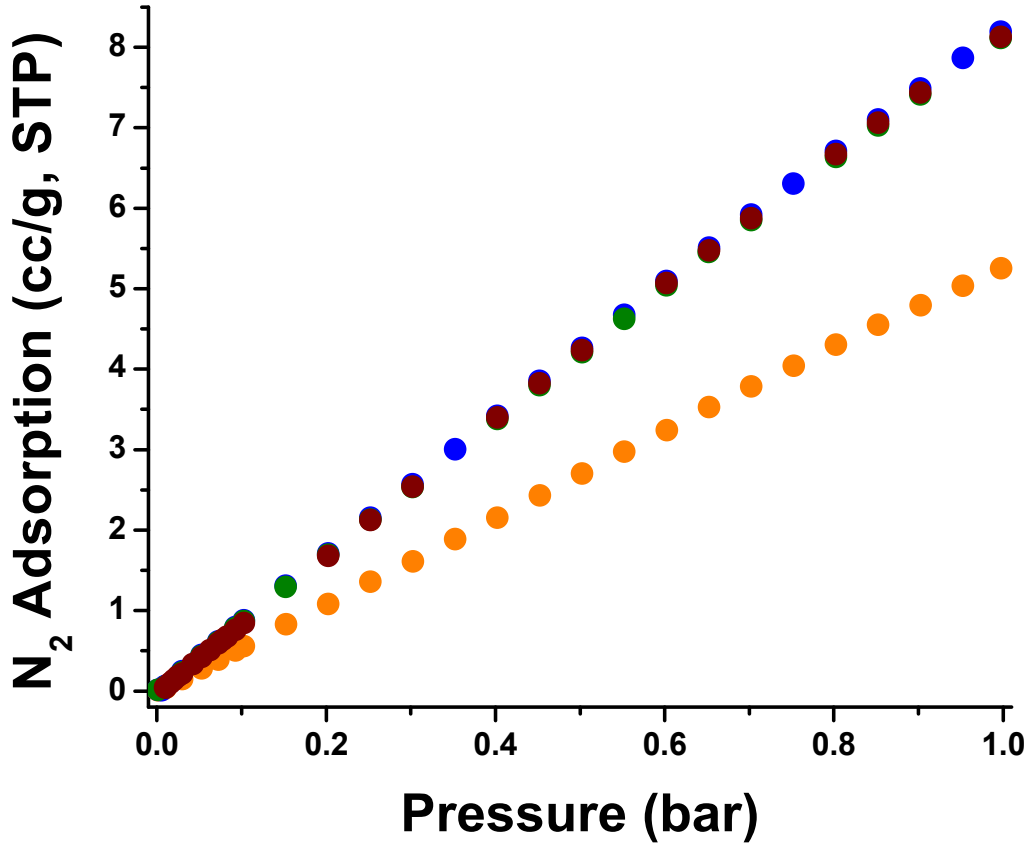

Figure A12 N_2 Isotherms (273 K) of **I** (blue), $\mathbf{I_{PA}}$ (green), $\mathbf{I_{C10}}$ (maroon), and $\mathbf{I_{SA}}$ (orange).

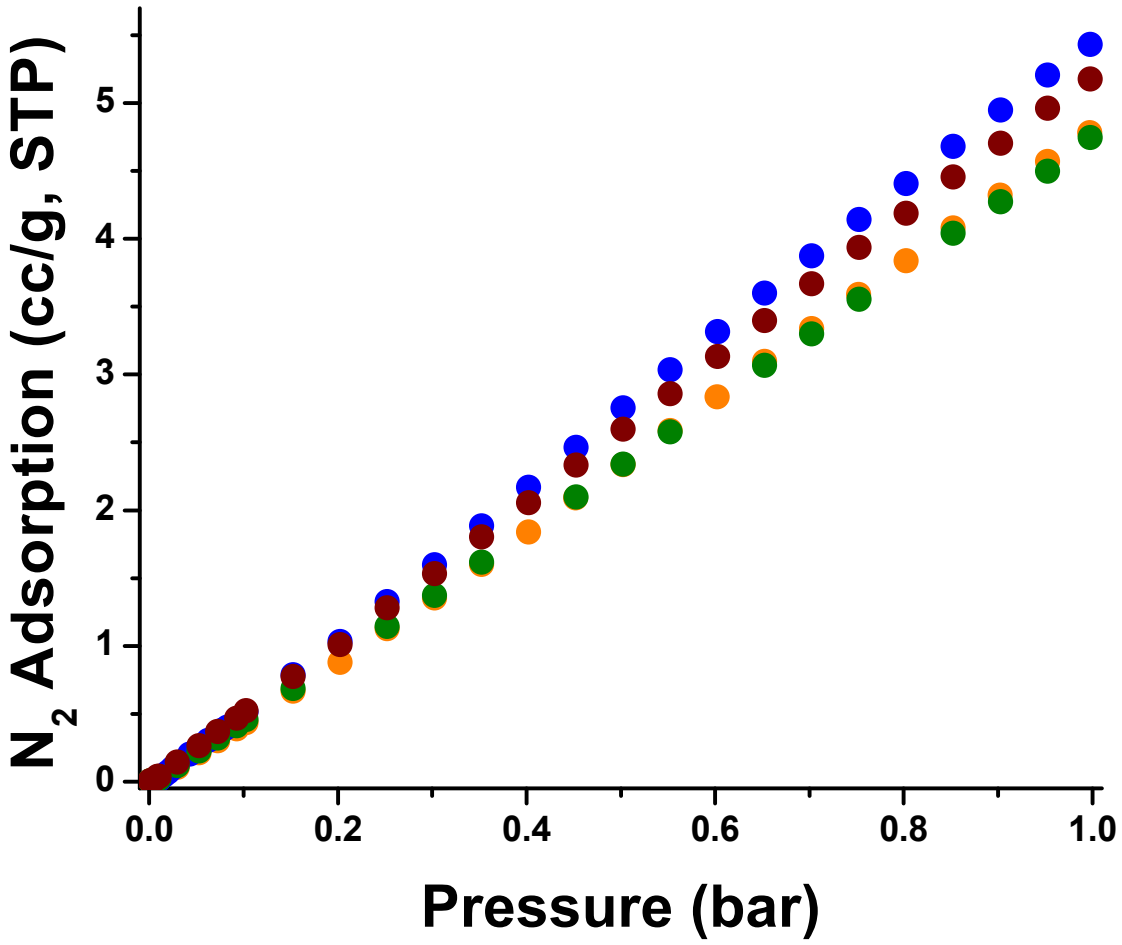

Figure A13 N_2 Isotherms (298 K) of **I** (blue), $\mathbf{I_{PA}}$ (green), $\mathbf{I_{C10}}$ (maroon), and $\mathbf{I_{SA}}$ (orange).

Bibliography

1. M. Eddaoudi, D. B. Moler, H. Li, B. Chen, T. M. Reineke, M. O'Keeffe and O. M. Yaghi, *Accounts of Chemical Research*, 2001, **34**, 319-330.

2. O. M. Yaghi, M. O'Keeffe, N. W. Ockwig, H. K. Chae, M. Eddaoudi and J. Kim, *Nature*, 2003, **423**, 705-714.

3. H. Furukawa, K. E. Cordova, M. O'Keeffe and O. M. Yaghi, *Science*, 2013, **341**.

4. H. Li, M. Eddaoudi, M. O'Keeffe and O. M. Yaghi, *Nature*, 1999, **402**, 276-279.

5. M. Eddaoudi, *Nature Materials*, 2007, **6**, 718-719.

6. F. Gandara and T. D. Bennett, *International Uunion of Crystallography Journal*, 2014, **1**, 563-570.

7. M. Fischer, J. R. B. Gomes, M. Fröba and M. Jorge, *Langmuir*, 2012, **28**, 8537-8549.

8. Q. Yang, S. Vaesen, F. Ragon, A. D. Wiersum, D. Wu, A. Lago, T. Devic, C. Martineau, F. Taulelle, P. L. Llewellyn, H. Jobic, C. Zhong, C. Serre, G. De Weireld and G. Maurin, *Angewandte Chemie International Edition*, 2013, **52**, 10316-10320.

9. R. B. Getman, Y.-S. Bae, C. E. Wilmer and R. Q. Snurr, *Chemical Reviews*, 2012, **112**, 703-723.

10. H. Babaei, A. J. H. McGaughey and C. E. Wilmer, *Chemical Science*, 2017, **8**, 583-589.

11. H. Babaei and C. E. Wilmer, *Physical Review Letters*, 2016, **116**, 025902.

12. K. D. Vogiatzis, E. Haldoupis, D. J. Xiao, J. R. Long, J. I. Siepmann and L. Gagliardi, *The Journal of Physical Chemistry C*, 2016, **120**, 18707-18712.

13. T. Li, D.-L. Chen, J. E. Sullivan, M. T. Kozlowski, J. K. Johnson and N. L. Rosi, *Chemical Science*, 2013, **4**, 1746.

14. K. B. Sezginel, T. Feng and C. E. Wilmer, *CrystEngComm*, 2017, **19**, 4497-4504.

15. J. Yu, L.-H. Xie, J.-R. Li, Y. Ma, J. M. Seminario and P. B. Balbuena, *Chemical Reviews*, 2017, **117**, 9674-9754.

16. Q. Yang, A. D. Wiersum, H. Jobic, V. Guillerm, C. Serre, P. L. Llewellyn and G. Maurin, *The Journal of Physical Chemistry C*, 2011, **115**, 13768-13774.

17. J. H. Cavka, S. Jakobsen, U. Olsbye, N. Guillou, C. Lamberti, S. Bordiga and K. P. Lillerud, *Journal of the American Chemical Society*, 2008, **130**, 13850-13851.

18. M. Eddaoudi, J. Kim, N. Rosi, D. Vodak, J. Wachter, M. O'Keeffe and O. M. Yaghi, *Science*, 2002, **295**, 469-472.

19. N. L. Rosi, J. Eckert, M. Eddaoudi, D. T. Vodak, J. Kim, M. O'Keeffe and O. M. Yaghi, *Science*, 2003, **300**, 1127-1129.

20. H. K. Chae, D. Y. Siberio-Perez, J. Kim, Y. Go, M. Eddaoudi, A. J. Matzger, M. O'Keeffe and O. M. Yaghi, *Nature*, 2004, **427**, 523-527.

21. K. K. Tanabe and S. M. Cohen, *Chemical Society Reviews*, 2011, **40**, 498-519.

22. H. Deng, C. J. Doonan, H. Furukawa, R. B. Ferreira, J. Towne, C. B. Knobler, B. Wang and O. M. Yaghi, *Science*, 2010, **327**, 846-850.

23. S. J. Garibay and S. M. Cohen, *Chemical Communications*, 2010, **46**, 7700-7702.

24. K. Konstas, T. Osl, Y. Yang, M. Batten, N. Burke, A. J. Hill and M. R. Hill, *Journal of Materials Chemistry*, 2012, **22**, 16698-16708.

25. J. R. Li, J. Sculley and H. C. Zhou, *Chemical Reviews*, 2012, **112**, 869-932.

26. K. Sumida, D. L. Rogow, J. A. Mason, T. M. McDonald, E. D. Bloch, Z. R. Herm, T. H. Bae and J. R. Long, *Chemical Reviews*, 2012, **112**, 724-781.

27. J. J. Gassensmith, H. Furukawa, R. A. Smaldone, R. S. Forgan, Y. Y. Botros, O. M. Yaghi and J. F. Stoddart, *Journal of the American Chemical Society*, 2011, **133**, 15312-15315.

28. L. Ma, C. Abney and W. Lin, *Chemical Society Reviews*, 2009, **38**, 1248-1256.

29. L. E. Kreno, K. Leong, O. K. Farha, M. Allendorf, R. P. Van Duyne and J. T. Hupp, *Chemical Reviews*, 2012, **112**, 1105-1125.

30. Z. Hu, B. J. Deibert and J. Li, *Chemical Society Reviews*, 2014, **43**, 5815-5840.

31. S. E. Miller, M. H. Teplensky, P. Z. Moghadam and D. Fairen-Jimenez, *Interface Focus*, 2016, **6**.

32. P. Horcajada, T. Chalati, C. Serre, B. Gillet, C. Sebrie, T. Baati, J. F. Eubank, D. Heurtaux, P. Clayette, C. Kreuz, J.-S. Chang, Y. K. Hwang, V. Marsaud, P.-N. Bories, L. Cynober, S. Gil, G. Ferey, P. Couvreur and R. Gref, *Nature Materials*, 2010, **9**, 172-178.

33. O. G. Nik, X. Y. Chen and S. Kaliaguine, *Journal of Membrane Science*, 2012, **413-414**, 48-61.

34. R. Q. Snurr, J. T. Hupp and S. T. Nguyen, *AIChE Journal*, 2004, **50**, 1090-1095.

35. T. Li, J. E. Sullivan and N. L. Rosi, *Journal of the American Chemical Society*, 2013, **135**, 9984-9987.

36. R. Quadrelli and S. Peterson, *Energy Policy*, 2007, **35**, 5938-5952.

37. R. S. Haszeldine, *Science*, 2009, **325**, 1647-1652.

38. A. Demessence, D. M. D'Alessandro, M. L. Foo and J. R. Long, *Journal of the American Chemical Society*, 2009, **131**, 8784-8786.

39. A. M. Fracaroli, H. Furukawa, M. Suzuki, M. Dodd, S. Okajima, F. Gandara, J. A. Reimer and O. M. Yaghi, *Journal of the American Chemical Society*, 2014, **136**, 8863-8866.

40. H. B. Tanh Jeazet, C. Staudt and C. Janiak, *Dalton Transactions*, 2012, **41**, 14003-14027.

41. E. V. Perez, K. J. Balkus, J. P. Ferraris and I. H. Musselman, *Journal of Membrane Science*, 2009, **328**, 165-173.

42. M. J. C. Ordoñez, K. J. Balkus, J. P. Ferraris and I. H. Musselman, *Journal of Membrane Science*, 2010, **361**, 28-37.

43. Y. Dai, J. R. Johnson, O. Karvan, D. S. Sholl and W. J. Koros, *Journal of Membrane Science*, 2012, **401-402**, 76-82.

44. B. Mu and K. S. Walton, *The Journal of Physical Chemistry C*, 2011, **115**, 22748-22754.

45. A. J. Howarth, Y. Liu, P. Li, Z. Li, T. C. Wang, J. T. Hupp and O. K. Farha, *Nature Reviews Materials*, 2016, **1**, 15018.

46. T. Loiseau, C. Serre, C. Huguenard, G. Fink, F. Taulelle, M. Henry, T. Bataille and G. Ferey, *Chemistry*, 2004, **10**, 1373-1382.

47. T.-L. Ho, *Chemical Reviews*, 1975, **75**, 1-20.

48. P. M. Schoenecker, C. G. Carson, H. Jasuja, C. J. J. Flemming and K. S. Walton, *Industrial & Engineering Chemistry Research*, 2012, **51**, 6513-6519.

49. J. B. DeCoste, G. W. Peterson, H. Jasuja, T. G. Glover, Y.-g. Huang and K. S. Walton, *Journal of Materials Chemistry A*, 2013, **1**, 5642.

50. S. Han, Y. Huang, T. Watanabe, S. Nair, K. S. Walton, D. S. Sholl and J. Carson Meredith, *Microporous and Mesoporous Materials*, 2013, **173**, 86-91.

51. H. Furukawa, F. Gándara, Y.-B. Zhang, J. Jiang, W. L. Queen, M. R. Hudson and O. M. Yaghi, *Journal of the American Chemical Society*, 2014, **136**, 4369-4381.

52. Y. Cai, Y. Zhang, Y. Huang, S. R. Marder and K. S. Walton, *Crystal Growth & Design*, 2012, **12**, 3709-3713.

53. H. Jasuja, N. C. Burtch, Y. G. Huang, Y. Cai and K. S. Walton, *Langmuir*, 2013, **29**, 633-642.

54. H. Jasuja and K. S. Walton, *The Journal of Physical Chemistry C*, 2013, **117**, 7062-7068.

55. Y. Cui, Y. Yue, G. Qian and B. Chen, *Chemical Reviews*, 2012, **112**, 1126-1162.

56. Y. T. Liang, G. P. Yang, B. Liu, Y. T. Yan, Z. P. Xi and Y. Y. Wang, *Dalton Transactions*, 2015, **44**, 13325-13330.

57. H. Wu, Y. S. Chua, V. Krungleviciute, M. Tyagi, P. Chen, T. Yildirim and W. Zhou, *Journal of the American Chemical Society*, 2013, **135**, 10525-10532.

58. M. S. Denny Jr, J. C. Moreton, L. Benz and S. M. Cohen, *Nature Reviews Materials*, 2016, **1**, 16078.

59. P. Bernardo, E. Drioli and G. Golemme, *Industrial & Engineering Chemistry Research*, 2009, **48**, 4638-4663.

60. L. M. Robeson, *Journal of Membrane Science*, 1991, **62**, 165-185.

61. L. M. Robeson, *Journal of Membrane Science*, 2008, **320**, 390-400.

62. J. C. Moreton, M. S. Denny and S. M. Cohen, *Chemical Communications*, 2016, **52**, 14376-14379.

63. D. Wu, G. Maurin, Q. Yang, C. Serre, H. Jobic and C. Zhong, *Journal of Materials Chemistry A*, 2014, **2**, 1657.

64. R. Semino, J. C. Moreton, N. A. Ramsahye, S. M. Cohen and G. Maurin, *Chemical Science*, 2018, **9**, 315-324.

65. Z. Sumer and S. Keskin, *Computational Screening of MOF-Based Mixed Matrix Membranes for CO_2/N_2 Separations*, 2016.

66. Z. Zhang, H. T. Nguyen, S. A. Miller and S. M. Cohen, *Angewandte Chemie International Edition*, 2015, **54**, 6152-6157.

67. G. E. M. Schukraft, S. Ayala, B. L. Dick and S. M. Cohen, *Chemical Communications*, 2017, **53**, 10684-10687.

68. Z. Zhang, H. T. Nguyen, S. A. Miller, A. M. Ploskonka, J. B. DeCoste and S. M. Cohen, *Journal of the American Chemical Society*, 2016, **138**, 920-925.

69. A. B. Spore and N. L. Rosi, *CrystEngComm*, 2017, **19**, 5417-5421.

70. H.-C. Zhou, J. R. Long and O. M. Yaghi, *Chemical Reviews*, 2012, **112**, 673-674.

71. N. C. Burtch, H. Jasuja and K. S. Walton, *Chemical Reviews*, 2014, **114**, 10575-10612.

72. D. Ma, Y. Li and Z. Li, *Chemical Communications*, 2011, **47**, 7377-7379.

73. H. Jasuja, Y. G. Huang and K. S. Walton, *Langmuir*, 2012, **28**, 16874-16880.

74. H. Jasuja and K. S. Walton, *Dalton Transactions*, 2013, **42**, 15421-15426.

75. H. Jasuja, J. Zang, D. S. Sholl and K. S. Walton, *The Journal of Physical Chemistry C*, 2012, **116**, 23526-23532.

76. K. A. Cychosz and A. J. Matzger, *Langmuir*, 2010, **26**, 17198-17202.

77. J. A. Greathouse and M. D. Allendorf, *Journal of the American Chemical Society*, 2006, **128**, 10678-10679.

78. P. Guo, D. Dutta, A. G. Wong-Foy, D. W. Gidley and A. J. Matzger, *Journal of the American Chemical Society*, 2015, **137**, 2651-2657.

79. S. J. Yang and C. R. Park, *Advanced Materials*, 2012, **24**, 4010-4013.

80. J. G. Nguyen and S. M. Cohen, *Journal of the American Chemical Society*, 2010, **132**, 4560-4561.

81. H. Li, W. Shi, K. Zhao, H. Li, Y. Bing and P. Cheng, *Inorganic Chemistry*, 2012, **51**, 9200-9207.

82. Q. Sun, H. He, W. Y. Gao, B. Aguila, L. Wojtas, Z. Dai, J. Li, Y. S. Chen, F. S. Xiao and S. Ma, *Nature Communications*, 2016, **7**, 13300.

83. J. J. Low, A. I. Benin, P. Jakubczak, J. F. Abrahamian, S. A. Faheem and R. R. Willis, *Journal of the American Chemical Society*, 2009, **131**, 15834-15842.

84. K. S. Park, Z. Ni, A. P. Cote, J. Y. Choi, R. Huang, F. J. Uribe-Romo, H. K. Chae, M. O'Keeffe and O. M. Yaghi, *Proceedings of the National Acadamy of Science, U S A*, 2006, **103**, 10186-10191.

85. J. An, S. J. Geib and N. L. Rosi, *Journal of the American Chemical Society*, 2009, **131**, 8376-8377.

86. K. A. White, D. A. Chengelis, K. A. Gogick, J. Stehman, N. L. Rosi and S. Petoud, *Journal of the American Chemical Society*, 2009, **131**, 18069-18071.

87. Q. Liu, H. Cong and H. Deng, *Journal of the American Chemical Society*, 2016, **138**, 13822-13825.

88. T. Li and N. L. Rosi, *Chemical Communications*, 2013, **49**, 11385-11387.

89. T. M. Alam, D. R. Dreyer, C. W. Bielwaski and R. S. Ruoff, *The Journal of Physical Chemistry A*, 2011, **115**, 4307-4316.

90. S. R. Venna, M. Lartey, T. Li, A. Spore, S. Kumar, H. B. Nulwala, D. R. Luebke, N. L. Rosi and E. Albenze, *Journal of Materials Chemistry A*, 2015, **3**, 5014-5022.

91. S. R. Venna and M. A. Carreon, *Langmuir*, 2011, **27**, 2888-2894.

92. O. Bakhtiari, S. Mosleh, T. Khosravi and T. Mohammadi, *Desalination and Water Treatment*, 2012, **41**, 45-52.

93. C. Zhang, Y. Dai, J. R. Johnson, O. Karvan and W. J. Koros, *Journal of Membrane Science*, 2012, **389**, 34-42.

94. T. T. Moore and W. J. Koros, *Journal of Molecular Structure*, 2005, **739**, 87-98.

95. S. Basu, A. Cano-Odena and I. F. J. Vankelecom, *Journal of Membrane Science*, 2010, **362**, 478-487.

96. T. Rodenas, M. van Dalen, E. García-Pérez, P. Serra-Crespo, B. Zornoza, F. Kapteijn and J. Gascon, *Advanced Functional Materials*, 2014, **24**, 268-268.

97. S. R. Venna, A. Spore, Z. Tian, A. M. Marti, E. J. Albenze, H. B. Nulwala, N. L. Rosi, D. R. Luebke, D. P. Hopkinson and H. R. Allcock, *Journal of Membrane Science*, 2017, **535**, 103-112.

98. M. Deng, S. G. Kumbar, Y. Wan, U. S. Toti, H. R. Allcock and C. T. Laurencin, *Soft Matter*, 2010, **6**, 3119-3132.

99. P. Jha, L. W. Mason and J. D. Way, *Industrial & Engineering Chemistry Research*, 2006, **45**, 6570-6577.

100. K. Nagai, B. D. Freeman, A. Cannon and H. R. Allcock, *Journal of Membrane Science*, 2000, **172**, 167-176.

101. C. J. Orme, M. K. Harrup, T. A. Luther, R. P. Lash, K. S. Houston, D. H. Weinkauf and F. F. Stewart, *Journal of Membrane Science*, 2001, **186**, 249-256.

102. C. J. Orme, J. R. Klaehn, M. K. Harrup, T. A. Luther, E. S. Peterson and F. F. Stewart, *Journal of Membrane Science*, 2006, **280**, 175-184.

103. J. G. Muldoon, P. N. Pintauro, R. J. Wysick, J. Lin, C. J. Orme and F. F. Stewart, *Journal of Membrane Science*, 2009, **334**, 74-82.

104. Z. Yang, Z. Wang, J. Li and J. Chen, *RSC Advances*, 2012, **2**, 11432-11437.

105. C. J. Orme and F. F. Stewart, *Journal of Membrane Science*, 2005, **253**, 243-249.

106. W. J. Koros and G. K. Fleming, *Journal of Membrane Science*, 1993, **83**, 1-80.

107. B. D. Freeman, *Macromolecules*, 1999, **32**, 375-380.

108. S. D. Burd, S. Ma, J. A. Perman, B. J. Sikora, R. Q. Snurr, P. K. Thallapally, J. Tian, L. Wojtas and M. J. Zaworotko, *Journal of the American Chemical Society*, 2012, **134**, 3663-3666.

109. P. Nugent, Y. Belmabkhout, S. D. Burd, A. J. Cairns, R. Luebke, K. Forrest, T. Pham, S. Ma, B. Space, L. Wojtas, M. Eddaoudi and M. J. Zaworotko, *Nature*, 2013, **495**, 80.

110. I. Skarmoutsos, Y. Belmabkhout, K. Adil, M. Eddaoudi and G. Maurin, *The Journal of Physical Chemistry C*, 2017, **121**, 27462-27472.

111. M. Alexandre and P. Dubois, *Materials Science and Engineering: R: Reports*, 2000, **28**, 1-63.

112. M. Z. Rong, M. Q. Zhang, Y. X. Zheng, H. M. Zeng, R. Walter and K. Friedrich, *Polymer*, 2001, **42**, 167-183.